MINISTRY OF EDUCATION AND RESEARCH

THE ANNALS OF "DUNAREA DE JOS" UNIVERSITY OF GALATI

Fascicle IX
METALLURGY AND MATERIALS SCIENCE

YEAR XLIV (XLIX)
March 2026, no. 1

ISSN 2668-4748; e-ISSN 2668-4756

GALATI UNIVERSITY PRESS

2026

EDITORIAL BOARD

THE ANNALS OF "DUNAREA DE JOS" UNIVERSITY OF GALATI
FASCICLE IX. METALLURGY AND MATERIALS SCIENCE
Nº. 1 - 2026, ISSN 2668-4748; e-ISSN 2668-4756
Volume DOI: https://doi.org/10.35219/mms.2026.1

Table of Contents

THE ANNALS OF "DUNAREA DE JOS" UNIVERSITY OF GALATI
FASCICLE IX. METALLURGY AND MATERIALS SCIENCE
Nº. 1 - 2026, ISSN 2668-4748; e-ISSN 2668-4756
Volume DOI: https://doi.org/10.35219/mms.2026.1

THE ANNALS OF "DUNAREA DE JOS" UNIVERSITY OF GALATI
FASCICLE IX. METALLURGY AND MATERIALS SCIENCE
Nº. 1 - 2026, ISSN 2668-4748; e-ISSN 2668-4756
Article DOI: https://doi.org/10.35219/mms.2026.1.01

TEMPERATURE EFFECTS ON THE DIMENSIONS OF CoCr ALLOYS: DILATOMETRIC STUDY

Mirabela Georgiana MINCIUNĂ[1,2], Petrică VIZUREANU[1,2]

[1] "Gheorghe Asachi" Technical University of Iasi, Faculty of Materials Science and Engineering, Blvd. Mangeron, No. 51, 700050, Iasi, Romania

[2] Centre of Excellence Geopolymer and Green Technology (CEGeoGTech), Universiti Malaysia Perlis (UniMAP), 01000 Perlis, Malaysia

e-mail: mirabela.minciuna@yahoo.ro

ABSTRACT

Cobalt-chromium (Co-Cr) alloys are widely employed in biomedical and dental applications due to their favourable mechanical properties, corrosion resistance, and thermal stability. This study investigates the effect of silicon (Si) addition on the chemical composition and dimensional behavior of Co-Cr alloys, with an emphasis on their suitability for removable partial denture frameworks. A series of Co-Cr alloys with variable Si content (0.5–7.05 wt.%) were analysed using optical emission spectrometry and dilatometry to establish correlations between composition and thermal expansion.

The experimental approach provides new insights into how silicon content modifies the thermal behavior and dimensional stability of Co-Cr alloys during heating up to 1200 °C. The novelty of this research lies in the systematic evaluation of Si addition as a compositional variable in Co-Cr dental alloys, which has not been extensively explored in relation to dilatometric behavior. The study demonstrates that controlled silicon enrichment not only reduces the linear thermal expansion coefficient but also enhances structural stability during thermal cycling, minimizing the risk of deformation or mismatch with low-fusing dental ceramics. These findings bridge the gap between alloy chemistry and thermal compatibility, offering a scientific basis for optimizing alloy formulations used in precision dental restorations.

The outcomes provide valuable guidelines for the development of advanced Co-Cr-Si alloys with improved dimensional accuracy and thermal performance, contributing to the reliability and longevity of metal-ceramic prosthetic components.

KEYWORDS: Co-Cr-Mo alloys, thermal expansion, silicon, dilatometry

1. Introduction

Cobalt-based alloys, especially those in the Co-Cr system, are widely used in biomedical and technical applications due to their optimal mechanical properties, corrosion resistance, and high temperature stability. In the field of dental technology, these materials represent a viable solution for the production of removable partial denture (RPD) frameworks, where resistance to mechanical stress and dimensional compatibility with ceramic veneers are essential factors [1-3]. The dimensional behavior of alloys under temperature variations plays a critical role, since differences between the thermal expansion coefficients of the alloy and the restorative material can lead to internal stresses, cracks, or micro-leakage at the interface. Therefore, dilatometric analysis becomes an indispensable method for understanding the phase transformations and dimensional changes that occur during the thermal cycles specific to casting and sintering [4].

The dilatometric method allows for the determination of both the linear coefficient of thermal expansion and any discontinuities associated with solid-state structural transformations. In the case of Co-Cr alloys, dimensional stability and the absence of phase transformations within the temperature range ensure their clinical performance. At the same time, the chemical composition directly influences the

THE ANNALS OF "DUNAREA DE JOS" UNIVERSITY OF GALATI
FASCICLE IX. METALLURGY AND MATERIALS SCIENCE
Nº. 1 - 2026, ISSN 2668-4748; e-ISSN 2668-4756
Article DOI: https://doi.org/10.35219/mms.2026.1.01

thermal behavior, with silicon being a particularly important alloying element for optimizing physical properties [5-7].

The purpose of this study is to analyse the dimensional changes via dilatometry of select alloys from the Co-Cr system with variable silicon additions, correlating dilatometric behavior with chemical composition and highlighting the practical implications for their use in the manufacture of partial denture frameworks [8-10].

2. Determinations of Chemical Composition by Optical Emission Spectrometry

The determination of the chemical composition via optical emission spectrometry was performed on samples collected after the solidification of the alloy, which was obtained by vacuum induction melting. Sample preparation for optical emission spectrometry was carried out by grinding with coarse-grit abrasive paper [11].

The chemical analysis of the cobalt-based alloys by optical emission spectrometry was conducted in the Laboratory of Optical Emission and X-Ray Fluorescence Spectrochemical Testing, using a SpectromaXx spark spectrometer [12-15].

The electrical discharge releases a significant amount of energy, resulting in the formation of plasma and the emission of characteristic light. The light spectrum is resolved by an optical diffraction grating, and the results are analysed using specialized software [16]. Since the discharge occurs only on the surface of the sample and does not penetrate the bulk, surface contamination must be carefully controlled. The mass concentrations of the elements in the cobalt-based alloys are listed in Table 1.

Table 1. *Chemical composition of alloys in the Co-Cr system*

Alloying element	**Co-Cr**	**Co-Cr-Si5**	**Co-Cr-Si6**	**Co-Cr-Si7**
	(Mass %)			
Co	70	60	57.70	56.88
Cr	19.28	27	26.53	26.40
Si	**0.50**	**5.06**	**6.10**	**7.05**
Mo	6	5	5.29	5.20
Ni	2.90	1.52	2.84	2.87
Mn	0.31	0.43	0.39	0.38
Fe	0.33	0.31	0.58	0.43
Other	0.68	0.68	0.57	0.79

Chemical composition studies have revealed that the primary elements present in these cobalt-based alloys are Co, Cr, and Mo, alongside the specific elements added to the commercial formulation. With the incremental increase of silicon, the proportions of the other elements showed proportionally lower values, with a notable change occurring in the base element, cobalt. While it was initially present at 70 wt.% in the commercial Co-Cr alloy, in the Co-Cr-Si7 alloy, its concentration decreased to 56.88 wt.%.

3. Thermal Effects on the Dimensional Stability of Co-Cr Alloys

Dilatometry was performed using a Linseis L75H/1400 differential dilatometer. The cobalt alloys subjected to dilatometric analysis featured flat parallel ends and a square cross-section with a width of 5 mm and a sample length of 30 mm, adhering to dilatometer standards [17].

Dilatometric analysis is used to establish the solid-state phase transformation points of materials and to determine the coefficient of linear thermal expansion. The theoretical basis of the coefficient of linear thermal expansion is rooted in the principle that atoms in equilibrium occupy the lowest energy level within the crystal lattice [18-22].

The melting range of alloys in the Co-Cr system must be at least 150-200 °C higher than the firing temperature of the associated ceramic materials. The ceramic veneers used fall into the category of low-sintering-temperature materials (850-1100 °C). To ensure efficient processing, it is recommended that the melting temperature of the alloys remain below 1400 °C, a range in which the studied alloys fit well [23].

The Co-Cr samples were placed on the sample holder, where they were heated linearly. Dimensional changes were transmitted through a quartz pushrod to a displacement sensor, while sample temperature was monitored using a thermocouple [6]. Specimen heating was conducted in an electric tubular furnace,

THE ANNALS OF "DUNAREA DE JOS" UNIVERSITY OF GALATI
FASCICLE IX. METALLURGY AND MATERIALS SCIENCE
No. 1 - 2026, ISSN 2668-4748; e-ISSN 2668-4756
Article DOI: https://doi.org/10.35219/mms.2026.1.01

up to the maximum temperature of 1200 °C, with a heating rate of 10 °C/min. The furnace cooling rate was regulated by the water-cooling system with a flow rate of 5 m^3/h [24-26].

Fig. 1. *Linseis L75H/1400 Dilatometer* [4]

Fig. 2. *Sample subjected to experimental investigations* [3]

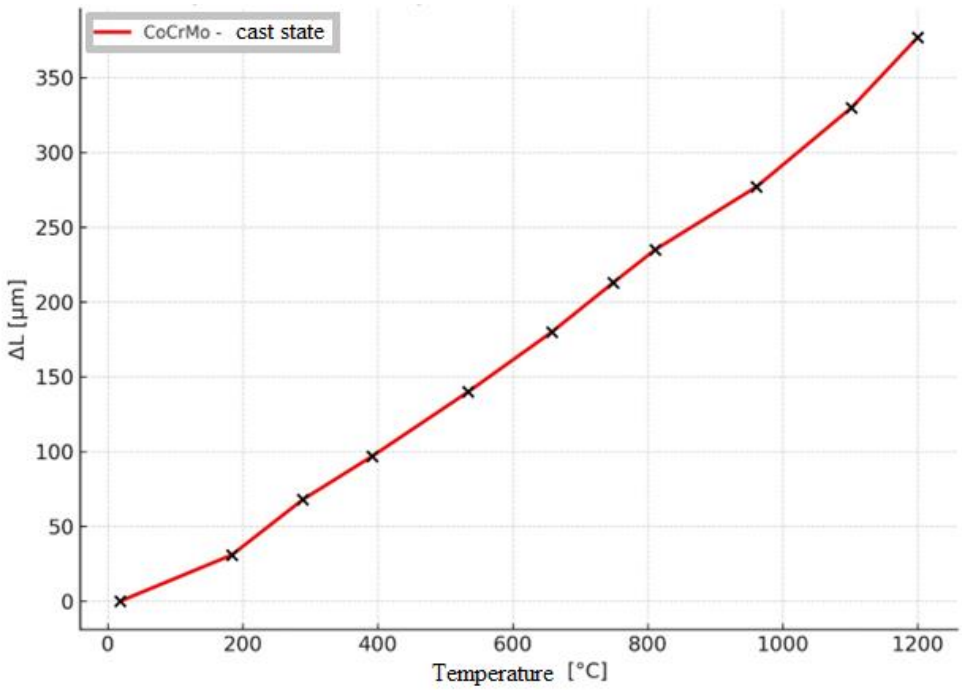

Fig. 3. *Variation of thermal expansion with temperature, for the Co-Cr alloy*

THE ANNALS OF "DUNAREA DE JOS" UNIVERSITY OF GALATI
FASCICLE IX. METALLURGY AND MATERIALS SCIENCE
No. 1 - 2026, ISSN 2668-4748; e-ISSN 2668-4756
Article DOI: https://doi.org/10.35219/mms.2026.1.01

During mechanical processing of cobalt alloys, dimensional variations may occur at high temperatures, leading to partially irreversible thermal expansion in the affected areas. Under these conditions, we analysed the behavior of Co-Cr system alloys under heating, considering both their clinical applications and the high temperatures reached during manufacturing (machining, melting, and investment casting).

Understanding the high-temperature behavior of these materials provides critical data on how physical, mechanical, and technological properties are established. The use of small samples usually ensures better precision in temperature control and increases the repeatability of results, while large samples facilitate superior precision in determining linear elongation [8].

The images below illustrate elongation as a function of temperature for the Co-Cr and Co-Cr-Si alloy systems. Figure 3 illustrates the thermal expansion of a Co-Cr alloy specimen, commonly used for removable partial dentures. The maximum thermal expansion that the specimen reaches at a temperature of 1200 °C is 377 µm.

Table 2 presents the variation of elongation as a function of heating temperature for the Co-Cr alloy.

Table 2. *Elongation values for Co-Cr alloy*

Temperature [ºC]		18	184	289	392	534	658	749	811	961	1102	1200
Thermal expansion [µm]	**Co-Cr**	0	31	68	97	140	180	213	235	277	330	377

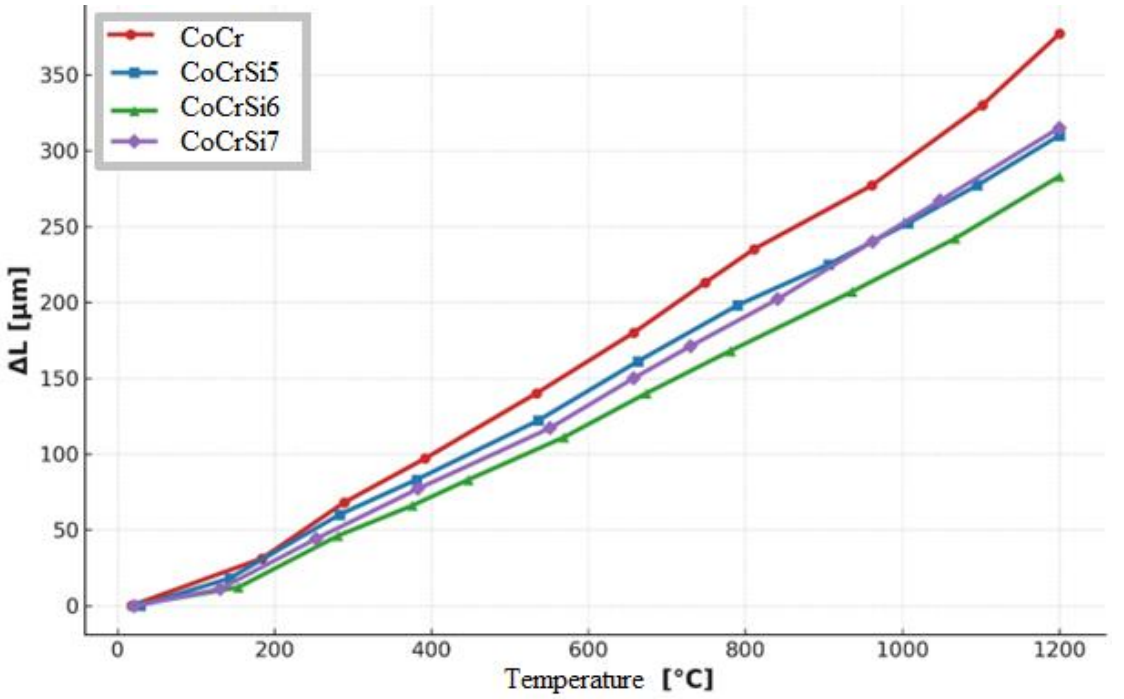

Fig. 4. *Variation of thermal expansion with temperature, for the Co-Cr-Si 5,6,7 alloy, cast state*

Temperature [ºC]		29	143	283	381	536	663	790	906	1007	1095	1200
Thermal expansion [µm]	**CoCrSi5**	0	18	60	83	122	161	198	225	252	277	310
	CoCrSi6	0	12	46	66	83	111	140	168	207	242	283
	CoCrSi7	0	11	44	77	117	150	171	202	240	267	315

Dilatometric analysis revealed a steady increase in elongation as temperature increased, which is characteristic of metallic materials. For the commercial Co-Cr alloy, the maximum expansion at 1200 °C was 377 µm, suggesting moderate thermal expansion suitable for low-fusing ceramic veneers. The modified alloys (C-oCr-Si5, Co-Cr-Si6, Co-Cr-Si7) showed maximum expansion values between

283–315 µm. These values are slightly lower than those of the commercial alloy, indicating superior dimensional stability at high temperatures. The melting range of these Co-Cr alloys (below 1400 °C) is sufficiently higher than the firing temperature of the ceramic (850–1100 °C), thus minimizing excessive deformation or expansion during ceramic sintering.

The phase transformation curves for both the Co-Cr and Co-Cr-Si alloys (Figures 3 and 4) display slight deviations from the otherwise linear trend. These irregularities may be associated with minor phase transformations or structural rearrangements occurring during heating, which could influence the thermal expansion behavior and should be further investigated.

This demonstrates the viability of using Co-Cr and Co-Cr-Si alloys for metal-ceramic and removable partial denture (RPD) frameworks without significant risks of thermal incompatibility. The small sample dimensions (5×5×30 mm) facilitated precise monitoring of temperature and elongation, ensuring repeatability across the experiments. The differences found between the Co-Cr-Si versions can be attributed to variations in chemical composition, which directly affects the coefficient of thermal expansion [27-29].

The expansion curves show an almost linear relationship between elongation and temperature, without abrupt discontinuities, suggesting a stable solid structure free of metastable phases within the examined range. The minor differences between Co-Cr-Si5 and Co-Cr-Si7 suggest an opportunity to optimize the composition to reduce thermal expansion, thus increasing the dimensional accuracy of the final prostheses.

4. Conclusions

Chemical analysis confirmed that the primary elements of these cobalt alloys are Co and Cr, with Si included in the experimental versions to adjust their physicochemical characteristics. The increase in silicon concentration caused a proportional reduction in the levels of the other alloying elements, most notably cobalt, the main component. Thus, cobalt, which was initially 70 wt.% in the commercial Co-Cr alloy, decreased to 56.88 wt.% in the modified Co-Cr-Si7 alloy. Dilatometric analysis validated the compatibility of both the base Co-Cr alloy and its Co-Cr-Si variants with dental ceramics, confirming an adequate melting range relative to the firing temperature of the ceramic.

The thermal expansion coefficient of the analysed alloys ensures precise control of dimensional changes during the ceramic sintering and firing processes.

The Co-Cr-Si5, Co-Cr-Si6, and Co-Cr-Si7 variants offer superior dimensional stability at high temperatures compared to the commercial Co-Cr alloy, which is highly beneficial for precision dental applications. The use of standardized small-scale specimens guaranteed superior repeatability and precision in the evaluation of elongation and expansion coefficient.

However, this study presents certain limitations. The dilatometric analysis was performed on cast specimens without subsequent heat treatment or microstructural characterization, which could further clarify the nature of the phase transformations observed as minor deviations in the expansion curves. In addition, the investigation was limited to a maximum temperature of 1200 °C; extending the thermal range and including controlled cooling cycles could provide more comprehensive insight into reversible structural changes.

Future work will focus on correlating the dilatometric behavior with detailed microstructural observations (via optical and electron microscopy) and differential scanning calorimetry to confirm phase transformation phenomena. Further studies will also evaluate the mechanical properties and metal-ceramic bond strength of the optimized Co-Cr–Si alloys to support their practical application in advanced dental prosthetics.

References

[1]. Moon J. H., Won D. M., *Analysis of sintering kinetics at different heating rates by dilatometry*, Metal Powder Report, 55(2), 39, 2000.
[2]. Dăneț A., *Spectroscopic Methods for Alloy Analysis*, Bucharest: Editura Tehnică, 2010.
[3]. ***, *ASTM E228-17 - Standard Test Method for Linear Thermal Expansion of Solid Materials with a Dilatometer. ASTM International*, 2017.
[4]. ***, *L75H/1400 Dilatometer Operation Manual*, Linseis GmbH, Selb, Germany, 2018.
[5]. Davis J. R., *Handbook of Thermal Expansion of Metals and Alloys*, ASM International, 2002.
[6]. Ristic M. M., *et al.*, *Sintering and Related Phenomena*, Pergamon Press, 2006.
[7]. German R. M., *Sintering: From Empirical Observations to Scientific Principles*, Elsevier, 2014.
[8]. Barbosa F. O., Araújo M. C., *Fractographic analysis of K3 nickel-titanium rotary instruments submitted to different modes of mechanical loading*, Journal of Endodontics, 34(8), p. 994-998, 2008.
[9]. Geis-Gerstorfer J., *Dental alloys: Physical properties and clinical applications*, Dental Materials Journal, 39(3), p. 345-356, 2020.
[10]. Anselme K., *et al.*, *Metal-ceramic compatibility in dental prosthetics*, Journal of Biomedical Materials Research Part B, 106(5), p. 2027-2035, 2018.
[11]. Baba N., *et al.*, *Mechanical strength of laser-welded cobalt–chromium alloy*, Journal of Biomedical Materials Research Part B, 69B, p. 121-124, 2004.
[12]. Baciu E. R., Forna N. C., *Influența tehnicilor de finisare asupra rugozității suprafețelor componentelor metalice ale*

restaurărilor protetice, Revista Medico-Chirurgicală a Societăţii de Medici şi Naturalişti din Iaşi, 114(4), p.1198-1203, 2010.
[13]. Behazin M., *et al.*, *Combined effects of pH and γ-irradiation on the corrosion of Co–Cr alloy Stellite-6*, Electrochimica Acta, 134, p. 399-410, 2014.
[14]. Li W., Lee L. J., *Low temperature cure of unsaturated polyester resins with thermoplastic additives: I. Dilatometry and morphology study*, Polymer, 41(2), p. 685-696, 2000.
[15]. Callister W. D., Rethwisch D. G., *Materials Science and Engineering: An Introduction*, (10th ed.), Wiley, 2020.
[16]. Hans M., *et al.*, *Thermal and mechanical behavior of Co–Cr dental alloys*, Journal of Prosthodontic Research, 63(2), p. 167-175, 2019.
[17]. Henriques B., *et al.*, *Mechanical behavior of Co–Cr dental alloys*, Journal of the Mechanical Behavior of Biomedical Materials, 4(8), p. 1718-1726, 2011.
[18]. Nowacki J., Pieczonka T., *Dilatometric analysis of sintering of iron–boron–cobalt P/M metal matrix composites*, Journal of Materials Processing Technology, 157-158, p. 749-754, 2004.
[19]. Witek K., Polkowski W., *Thermal expansion and microstructural stability of Al-Si alloys reinforced with ceramic particles*, Materials Characterization, 145, p. 250-258, 2018.
[20]. Ceschini L., *et al.*, *Effect of thermal exposure on the wear and mechanical properties of aluminum matrix composites*, Wear, 352-353, p. 144-152, 2016.
[21]. Kieback B., *et al.*, *Processing techniques for metal matrix composites*, Materials Science and Engineering: A, 362(1-2), p. 81-106, 2003.
[22]. Liu C., *et al.*, *Thermo-mechanical fatigue behavior of Co–Cr–Mo alloys for biomedical applications*, Materials Science and Engineering: C, 120, 111746, 2021.
[23]. Danninger H., Gierl C., *Sintering of ferrous powder compacts: Mechanisms and practical aspects*, Powder Metallurgy, 46(3), p. 213-221, 2003.
[24]. Xu X., *et al.*, *Effect of heat treatment on microstructure and wear resistance of Co–Cr dental alloys*, Surface & Coatings Technology, 394, 125872, 2020.
[25]. Swaminathan V., Narayanasamy R., *Tribological behavior of aluminum-based composites under dry sliding conditions*, Journal of Materials Research and Technology, 4(2), p. 151-158, 2015.
[26]. Callister W. D., Rethwisch D. G., *Materials Science and Engineering: An Introduction*, (10th ed.), Wiley, 2020.
[27]. Hans M., *et al.*, *Thermal and mechanical behavior of Co–Cr dental alloys*, Journal of Prosthodontic Research, 63(2), p. 167-175, 2019.
[28]. Henriques B., *et al.*, *Mechanical behavior of Co–Cr dental alloys*, Journal of the Mechanical Behavior of Biomedical Materials, 4(8), p. 1718-1726, 2011.
[29]. Nowacki J., Pieczonka T., *Dilatometric analysis of sintering of iron–boron–cobalt P/M metal matrix composites*, Journal of Materials Processing Technology, 157-158, p. 749-754, 2004.

THE ANNALS OF "DUNAREA DE JOS" UNIVERSITY OF GALATI
FASCICLE IX. METALLURGY AND MATERIALS SCIENCE
No. 1 - 2026, ISSN 2668-4748; e-ISSN 2668-4756
Article DOI: https://doi.org/10.35219/mms.2026.1.02

FAILURE CASE STUDY SERIES PART ONE: ANALYSIS OF OXYGEN COMPRESSOR SHAFT BREAKAGE

Liviu GURĂU, Carmela GURĂU, Gheorghe GURĂU
Interdisciplinary Research Centre in the Field of Eco-Nano Technology and Advanced Materials CC-ITI, Faculty of Engineering, "Dunarea de Jos" University of Galati, 47 Domneasca Street, 800008 Galati, Romania
e-mail: gheorghe.gurau@ugal.ro

ABSTRACT

This paper presents the results of a failure analysis of an oxygen compressor shaft using seven basic steps. The findings of this work form the basis for corrective and preventive actions to enhance equipment reliability and prevent future recurrence. The paper also offers a simple and direct approach to determine the root cause of structural component failure.

Visual inspection, specimen selection and preservation, high-stress area identification, chemical analysis with comparison to standards, hardness testing, optical microscopy, scanning electron microscopy (SEM), and EDS analysis were performed. A comprehensive metallurgical analysis of the oxygen compressor shaft failure provided substantial insights into the underlying mechanism, indicating shaft misalignment and bending-induced fatigue as the primary causes, with poor steel quality contributing to faster crack initiation and propagation.

KEYWORDS: failure analysis, fatigue, compressor shaft, OM, SEM, EDS

1. Introduction

The compressor crankshaft is a critical rotating component that converts the reciprocating motion of the pistons into rotary motion, enabling the continuous compression of oxygen gas [1]. Typically manufactured from high-strength forged steel, the crankshaft is designed to withstand cyclic stress [2, 3], torsional loads, and high operating pressures under continuous service. Failure of this component can cause significant secondary damage to associated parts such as bearings, connecting rods, and the housing.

Failure occurs when mechanical components lose their designed functionality under various stresses, such as mechanical loads, thermal stresses, corrosion, or combined effects [4, 5]. Primary tools for shaft failure analysis include visual inspection, optical microscopy, scanning electron microscopy (SEM), metallurgical analysis, and mechanical testing [6-8].

Fatigue is a progressive and localized structural damage mechanism [9-11] that occurs when a material is subjected to cyclic or fluctuating stresses, typically at magnitudes significantly below its ultimate tensile strength (UTS) or yield strength [9, 12, 13]. Under repeated loading–unloading cycles, microscopic defects within the material—such as dislocations, inclusions, or surface irregularities—serve as stress concentrators and evolve into fatigue cracks [14-16].

The main objective of this research is to determine the sequence of events, specifically whether the Shaft failure occurred first or if bearing damage initiated the failure, and to identify the root causes and contributing factors [8].

2. Experimental procedure

The chemical composition was determined by spectral testing using Thermo Scientific ARL 3460 Advantage. The ARL 3460 optical emission spectrometer has been specifically configured to address the analytical requirements for a wide range of alloys. It is driven by the OXSAS analytical software, which provides simple one-click routine analysis launch and full traceability. The test was performed in accordance with ASTM E415-21 for the analysis of carbon and low-alloy steels using spark atomic emission spectrometry. The method facilitates the simultaneous determination of 21 alloying and residual elements in carbon and low-alloy steels.

The hardness test was performed using the KB150 R - Digital Rockwell universal hardness testing machine. This machine is designed for automatic hardness testing and operates within a load

THE ANNALS OF "DUNAREA DE JOS" UNIVERSITY OF GALATI
FASCICLE IX. METALLURGY AND MATERIALS SCIENCE
Nº. 1 - 2026, ISSN 2668-4748; e-ISSN 2668-4756
Article DOI: https://doi.org/10.35219/mms.2026.1.02

range from 1 to 2500 (N), and is used for Rockwell, superficial Rockwell, and depth measurements for Vickers and Brinell tests.

Stereomicroscopy plays a crucial role in failure analysis. The Nikon SMZ745 stereoscopic microscope was employed for low-magnification observation of failure surface.

Optical microscopy was performed using the Olympus GX51 metallurgical microscope, widely used in automotive, aerospace, metallurgy, and research laboratories for precise material characterization and failure analysis. The cross-sectional sample was polished up to 1500 emery grade, followed by 1µm velvet cloth polishing, and then etched using a 2% Nital solution to reveal the microstructures.

Scanning electron microscopy (SEM) and energy dispersive X-ray spectroscopy (EDS) were carried out on the cross-sectional fractured surface of the sample using the JEOL IT-300LV Scanning Electron Microscope. To identify and quantify elemental composition of materials at microscopic scales, the Bruker Energy-Dispersive X-ray Spectroscopy (EDS) system integrated into JEOL SEM was employed.

3. Results and discussion

3.1. Visual inspection

The visual inspection was conducted on the failed compressor components to evaluate the condition of the shaft, bearings, and housing sleeve. The objective was to identify signs of damage, wear patterns, and fracture characteristics that could help determine the root cause of failure. Detailed observations were recorded and supported by photographs (Figure 1) to facilitate subsequent analysis.

Fig. 1. *The fracture surface*

The images show a catastrophic shaft fracture near the bearing region. The fracture surface exhibits fatigue leading to catastrophic failure. The bearing shows complete structural failure, with the rolling elements deformed and displaced from their original positions.

The visual inspection indicates that the compressor shaft experienced a catastrophic fatigue fracture near the bearing and coupling region. The bearing adjacent to the fracture shows complete structural failure, with severe deformation and displacement of the bearing elements, implying a loss of internal alignment and a potential seizure.

3.2. Chemical Composition - Spectral Test

The chemical composition (Table 1) indicates a steel grade similar to 42CrMo4 EN10083/3 (2006). Spectro analysis revealed high sulphur, since no calcium was added during processing, the inclusions remain unmodified and elongated, which may act as stress concentrators.

Typical applications of grade 42CrMo4 EN10083/3 (2006) are: compressor and turbine shafts, aircraft landing gear and engine components, crankshafts, connecting rods, transmission shafts, heavy-duty fasteners, and high-stress structural parts. The key features of this steel are: high strength and toughness over a wide temperature range, excellent fatigue and impact resistance, good hardenability with deep case formation, and moderate corrosion resistance.

THE ANNALS OF "DUNAREA DE JOS" UNIVERSITY OF GALATI
FASCICLE IX. METALLURGY AND MATERIALS SCIENCE
No. 1 - 2026, ISSN 2668-4748; e-ISSN 2668-4756
Article DOI: https://doi.org/10.35219/mms.2026.1.02

Table 1. *Shaft chemical composition*

Element	Compressor Shaft	42CrMo4 EN10083/3 2006	Remarks
Carbon (C)	0.415	0.38–0.45	Within range
Silicon (Si)	0.205	≤0.40	Within range
Manganese (Mn)	0.717	0.60–0.90	Within range
Phosphorus (P)	0.0073	≤0.025	Acceptable
Sulfur (S)	0.0256	≤0.035	**High - not favorable**
Nitrogen (N)	0.0081	—	Acceptable
Chromium (Cr)	0.865	0.90 – 1.20	Acceptable
Molybdenum (Mo)	0.181	0.15–0.30	Within range
Nickel (Ni)	0.747	-	Acceptable
Calcium (Ca)	0.0	—	**No Ca –** inclusions unmodified to globular
Aluminum (Al)	0.0012	≤0.05	Within limit
Vanadium (V)	0.0042	≤0.05	Trace
Titanium (Ti)	0.0027	≤0.05	Trace
Coper (Cu)	0.167	≤0.35	**High - not favorable**
Niobium (Nb)	0.0017	—	Trace
Borom (B)	0.00033	≤0.003	Within limit
CEV	0.80	—	

3.3. Hardness test

The test method used for the blade sample pieces was Vickers Hardness (30) in accordance with the ASTM E92 standard. The resulting value was converted to HB (Brinnel) and HRB (Rockwell). The Vickers 30 (HV 30) test is a highly precise method for measuring material hardness under a 300 N load. It is widely used in metallurgical testing, quality control, and failure analysis to assess the durability and wear resistance of components.

The hardness test was performed 10 mm away from the fracture surface to assess the material's baseline mechanical properties and minimize the influence of deformation or thermal effects near the fracture. This ensures the measured hardness reflects the true condition of the shaft material.

The shaft material exhibited a hardness of 257 HV, consistent with typical values for medium-carbon or heat-treated steels used in fatigue-loaded components. This value falls within the typical range of 250–300 HV, suggesting that the material maintained its expected strength and was not significantly softened.

3.4. Stereomicroscopy

The fracture surface indicates fatigue failure under bending stress. The crack initiated at the outer surface and propagated progressively, as evidenced by the concentric beach marks. The presence of a fibrous region signifies the rapid final fracture that occurred when the remaining cross-section could no longer sustain the applied load. The non-radial alignment of the fibrous region relative to the point of initiation further confirms asymmetric bending - rather than symmetric stress - as the dominant loading condition. Overall, the observed features - initiation site, beach marks, and final rupture are fully consistent with a fatigue-induced fracture mechanism under cyclic bending.

THE ANNALS OF "DUNAREA DE JOS" UNIVERSITY OF GALATI
FASCICLE IX. METALLURGY AND MATERIALS SCIENCE
Nº. 1 - 2026, ISSN 2668-4748; e-ISSN 2668-4756
Article DOI: https://doi.org/10.35219/mms.2026.1.02

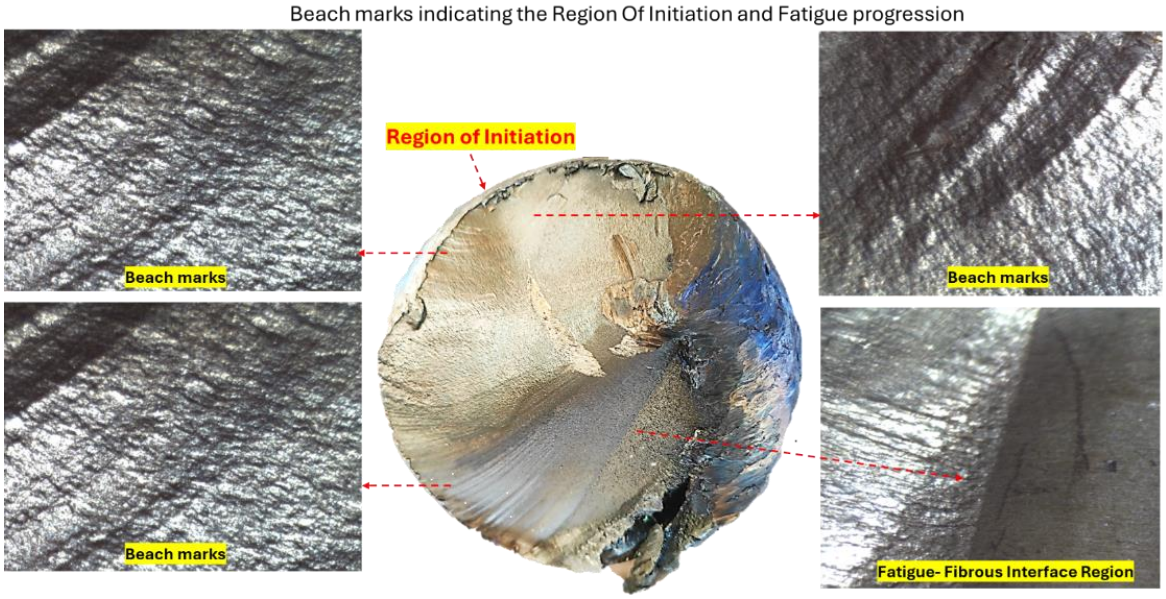

Fig. 2. *Stereomicroscopy images on different zones on failure surface*

3.5. Optical microscopy

The cross-sectional samples (Figure 3) were hot-mounted in phenolic resin. After grinding and polishing, the samples were etched (using 2% nital) and examined for microstructural inferences.

Figure 3b points out a homogenous, fine ferrite-pearlite structure.

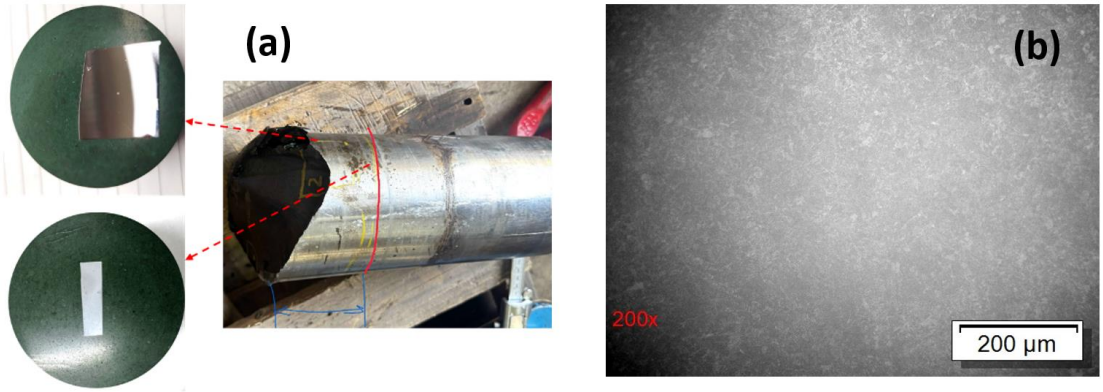

Fig. 3. *Cross-sectional samples (a), ferrite-pearlite structure*

3.6. SEM investigations

SEM was used for fractography analysis to reveal microscopic features such as dimples, cleavage facets, beach marks, and striations that indicated fracture modes and root causes of material failure. Additionally, it was used to detect inclusions, impurities, segregation, porosity, and other processing defects acting as stress concentrators.

EDS was used to measure the weight percentage of all elements present in the defect area. Furthermore, elemental distribution maps clearly visualized element segregation, diffusion, inclusions, and contaminants. Quantitative data reports with precise elemental percentages including spectra, maps, and line profiles were generated.

Ratchet marks were observed that indicate multiple crack planes merging with one another (Figure 4a and b). Moreover, Figure 4c and d show multiple striation indicating progressive fatigue crack growth under cyclic loading.

On further examination, we can observe a coarse exogenous inclusion (0.72 mm) at a depth of 0.80 mm from the surface, located precisely at the region of crack initiation. This inclusion likely acted as a stress concentrator, contributing to the onset of fatigue failure.

THE ANNALS OF "DUNAREA DE JOS" UNIVERSITY OF GALATI
FASCICLE IX. METALLURGY AND MATERIALS SCIENCE
No. 1 - 2026, ISSN 2668-4748; e-ISSN 2668-4756
Article DOI: https://doi.org/10.35219/mms.2026.1.02

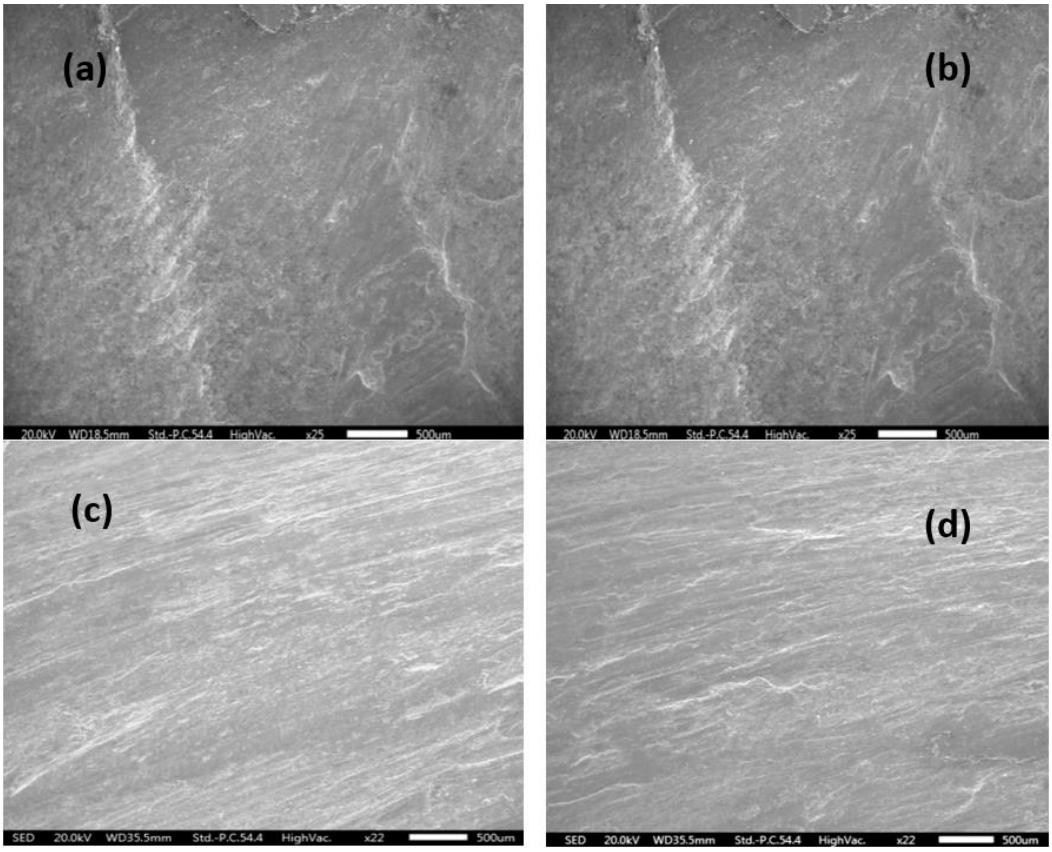

Fig. 4. *SEM micrographs*

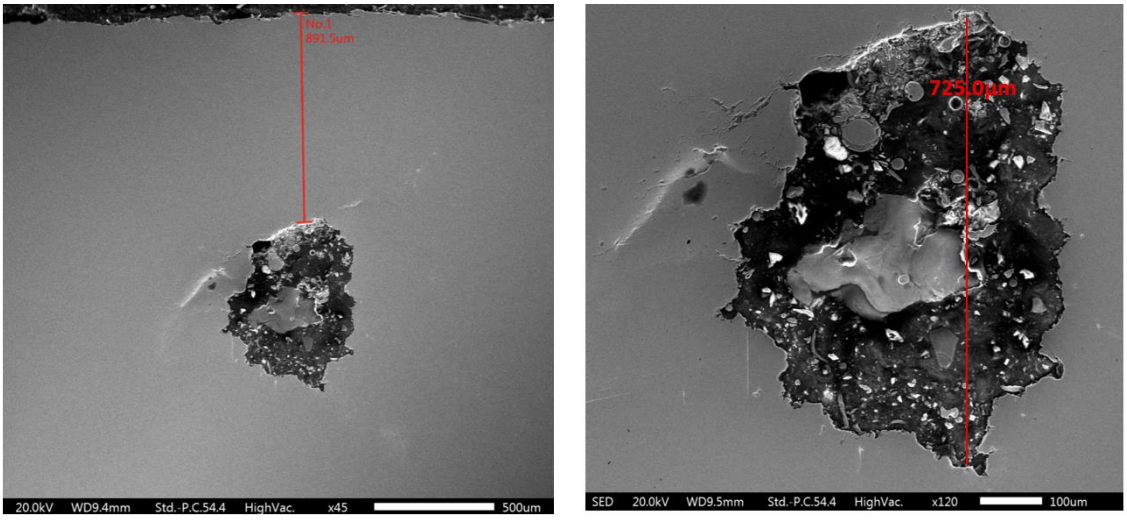

Fig. 5. *SEM micrographs - exogenous inclusion*

3.7. SEM-EDS analysis

EDS analysis reveals that the inclusion is primarily composed of O, Al, Si, and Fe, indicating an oxide-based inclusion, likely aluminosilicate in nature. Such inclusions can act as stress concentrators and contribute to crack initiation at the fracture surface.

Elemental mapping (Figure 7) confirmed that the complex oxide inclusion comprises predominantly of Al, Mg, and Si.

THE ANNALS OF "DUNAREA DE JOS" UNIVERSITY OF GALATI
FASCICLE IX. METALLURGY AND MATERIALS SCIENCE
Nº. 1 - 2026, ISSN 2668-4748; e-ISSN 2668-4756
Article DOI: https://doi.org/10.35219/mms.2026.1.02

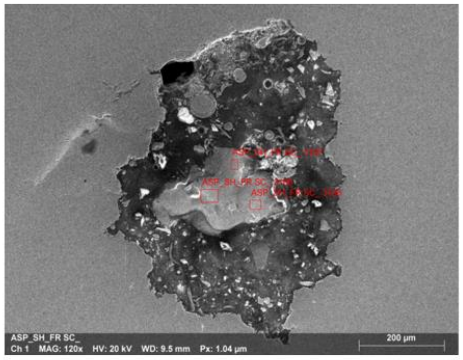

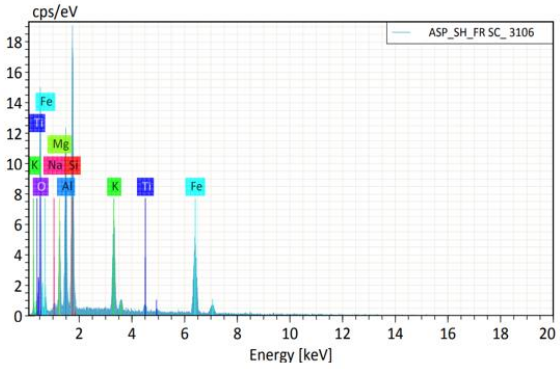

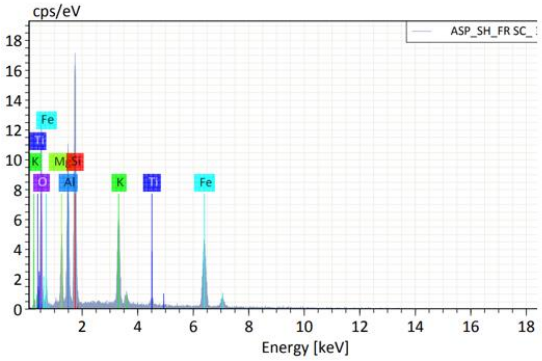

Spectrum	O	Na	Mg	Al	Si	K	Ti	Fe
ASP_SH_FR SC_ 3106	39.91	0.41	5.79	11.22	15.06	7.70	1.01	18.89
ASP_SH_FR SC_ 3107	39.28		4.53	9.93	15.21	8.74	0.91	21.40
ASP_SH_FR SC_ 3108	37.90		5.78	11.88	15.76	8.07	1.12	19.49
Mean	**39.03**	**0.41**	**5.37**	**11.01**	**15.34**	**8.17**	**1.02**	**19.93**
Sigma	**1.03**	**0.00**	**0.73**	**0.99**	**0.37**	**0.53**	**0.11**	**1.31**
SigmaMean	**0.59**	**0.00**	**0.42**	**0.57**	**0.21**	**0.31**	**0.06**	**0.75**

Fig. 6. *EDS spectra*

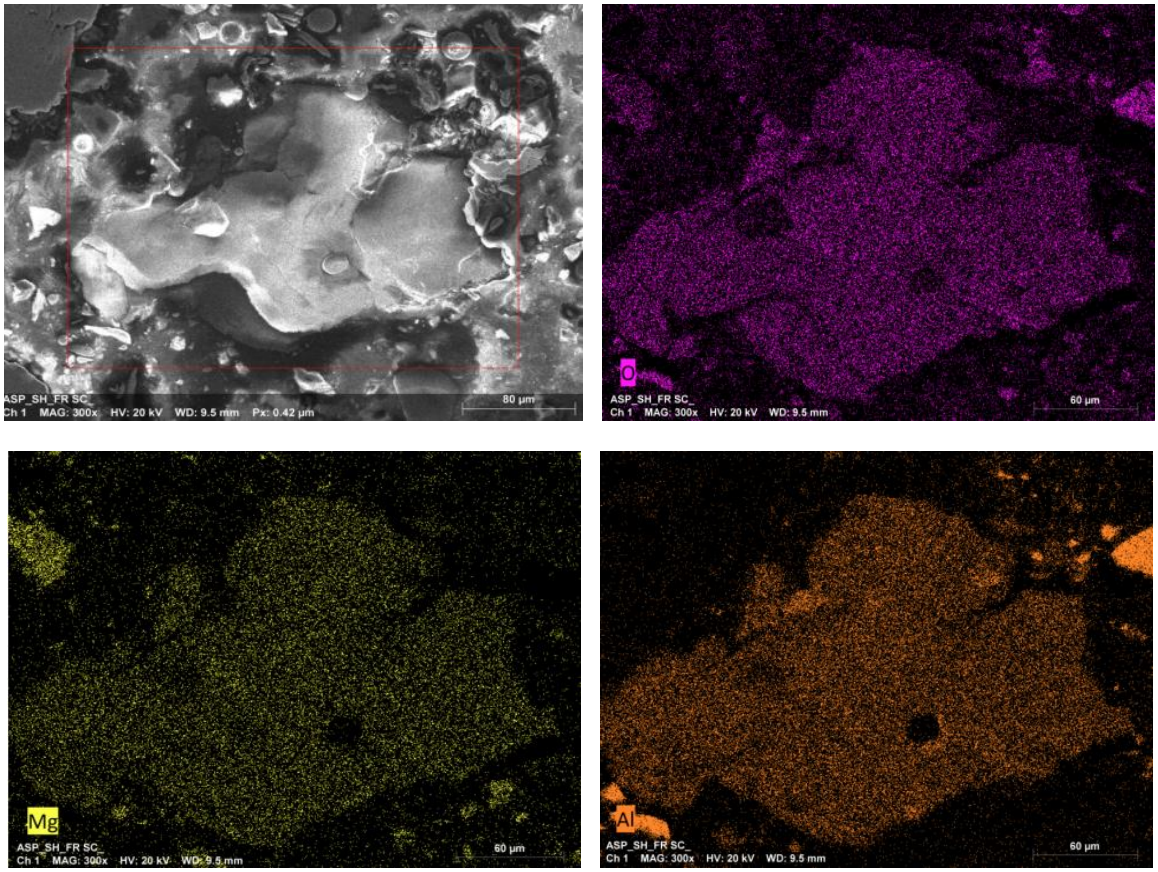

THE ANNALS OF "DUNAREA DE JOS" UNIVERSITY OF GALATI
FASCICLE IX. METALLURGY AND MATERIALS SCIENCE
No. 1 - 2026, ISSN 2668-4748; e-ISSN 2668-4756
Article DOI: https://doi.org/10.35219/mms.2026.1.02

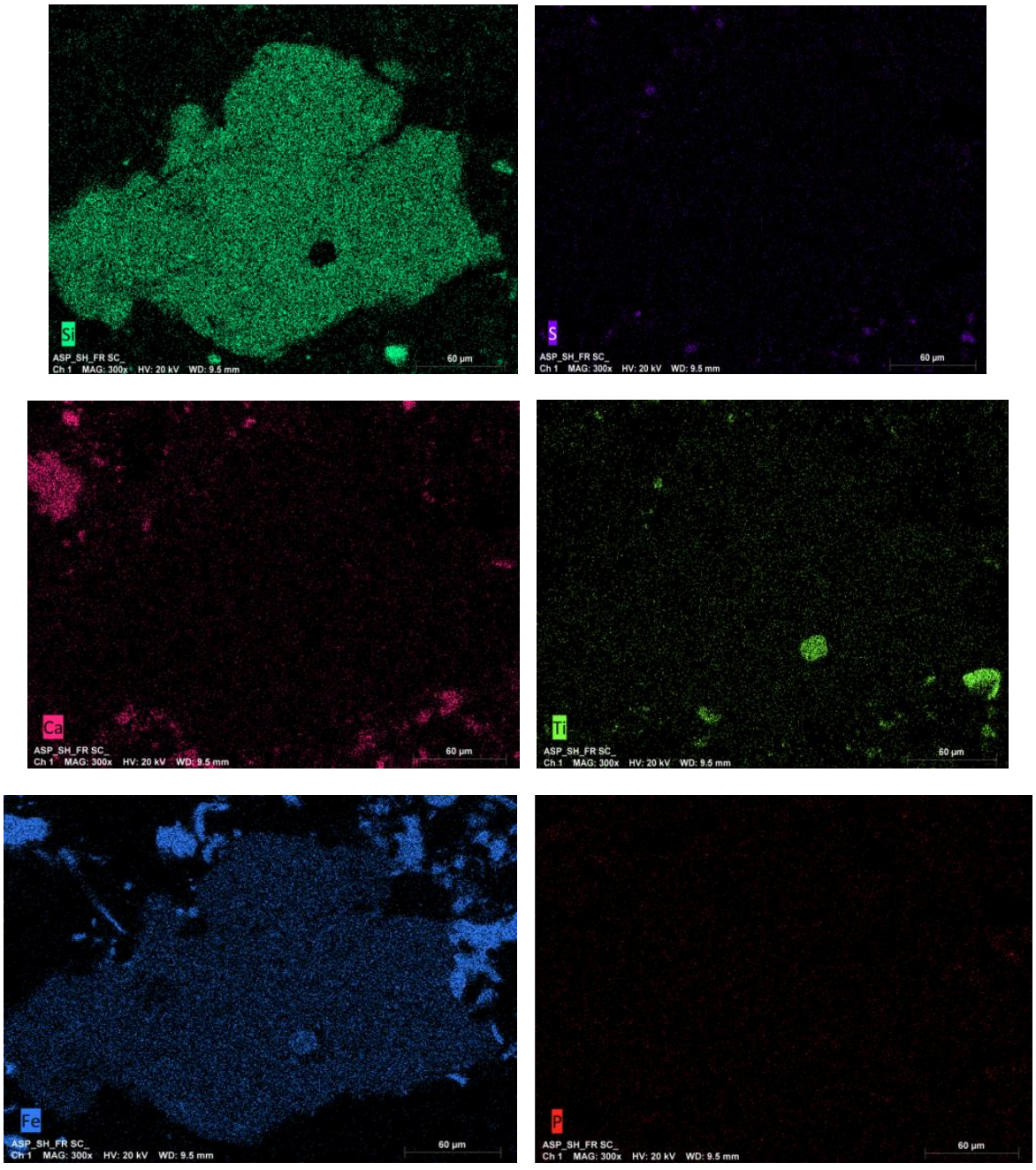

Fig. 7. *Elemental mapping (SEM)*

4. Conclusions

In summary, physical and microscopic examination revealed progressive fatigue features on the fracture surface, including beach marks and ratchet marks. The fracture initiated near the bearing region, and the crack propagated over time under cyclic bending stresses rather than resulting from a sudden overload.

Visual inspection of the housing sleeve showed severe scratches and abrasive wear on the side adjacent to the fractured shaft, confirming significant relative movement due to misalignment of the shaft-bearing assembly. On the opposite side, where no sleeves were installed, remained smooth and free of wear.

Chemical and microstructural analysis showed the shaft material is similar to 42CrMo4 EN10083/3 (2006) steel grade, with the following notable characteristics: a sulphur content of 0.026%, which is on the higher side and prone to harmful inclusions. The lack of calcium addition potentially leaves

inclusions unmodified and elongated, which act as stress concentrators.

SEM-EDS and elemental mapping revealed coarse, complex oxide inclusions (0.72 mm) at the region of initiation.

The defect mechanism and crack progression reveal that misalignment of the shaft-bearing assembly created rotational bending stresses and localized stress concentration zones. Fatigue cracks initiated at stress concentration points under cyclic operational loading were observed. Progressive crack growth is clearly evidenced by beach marks and ratchet marks. Finally, the shaft fracture occurred when the remaining cross-section could no longer sustain the bending loads, with bearing failure occurring subsequently as a secondary event.

Optical microscopy and hardness testing confirmed a homogeneous ferrite–pearlite microstructure, with hardness values consistent with the specified requirements. However, the presence of exogenous complex oxide inclusions and high sulphur levels without calcium treatment indicates a low level of quality focus by the manufacturer, which is concerning for such a critical end-use application.

References

[1]. Hou Nan, *et al.*, *Failure modes, mechanisms and causes of shafts in mechanical equipment*, Engineering Failure Analysis, vol. 136, 106216, 2022.
[2]. Wang M. S., *et al.*, *Failure analysis of screw shaft in screw compressor*, Engineering Failure Analysis, vol. 125, 105424, 2021.
[3]. Shahrivar A., Abdolmaleki A. R., *Failure of a screw compressor shaft*, Engineering Failure Analysis, vol. 13, issue 4, p. 698-704, 2006.
[4]. Florez Jorge Mario Tirado, *et al.*, *Analysis of the failure of an offshore compressor crankshaft*, Case Studies in Engineering Failure Analysis, p. 50-55, 2016.
[5]. Safaat Aat, Noviyanto Alfian, *Failure analysis of rotary screw compressor and its modifications*, International Journal of Innovation in Mechanical Engineering and Advanced Materials, 2021.
[6]. Fioravanti A., *et al.*, *Compressor Station Facility Failure Modes: Causes, Taxonomy and Effects*, Report EUR 30265 EN, by the European Commission Joint Research Centre (JRC), 2020.
[7]. Xu L., *et al.*, *Analysis of the causes of driving gear shaft fractures in gear pumps*, J. Fail. Anal. Prev., 20(1), p. 242-2482020.
[8]. Fuller R.W., *et al.*, *Horstemeyer, Failure analysis of aisi 304 stainless steel shaft*, Eng. Fail. Anal., 15(7), p. 835-846, 2008.
[9]. Callister W. D. Jr., Rethwisch D. G., *Callister's Materials Science and Engineering*, (10th ed.), John Wiley & Sons, 2020.
[10]. Martínez L., *et al.*, *Crack propagation by activated avalanches during creep and fatigue from elastic interface theory*, Physical Review Materials, 9(1), 013401, 2025.
[11]. Singh P., El-Awady J., *Low cycle fatigue behaviour of engineering metallic materials: Review on cyclic deformation micro-mechanism*, Materials Science and Engineering A, 876, 145322, 2024.
[12]. Chen X., *et al.*, *Fatigue life predictor: Predicting fatigue life of metallic materials using LSTM with a contextual attention model*, RSC Advances, 15(3), p. 1234-1247, 2025.
[13]. Rahman M., *et al.*, *Performance of composite metal foams under cyclic loading at elevated temperatures*, Journal of Materials Science, 60(5), p. 2150-2164, 2025.
[14]. Zhao H., *et al.*, *Fatigue crack growth of WC–Co cemented carbides: A comparative study using small indentation flaws and long through-thickness cracks*, International Journal of Fracture, 239(1), p. 1-20, 2024.
[15]. Santos A., *et al.*, *Numerical fatigue crack growth on compact tension specimens under Mode I and mixed-mode (I+II) loading*, Engineering Fracture Mechanics, 290, 110346, 2024.
[16]. Nguyen T., *et al.*, *Elucidating microstructural influences on fatigue behavior for additively manufactured Hastelloy X using a Bayesian-calibrated crystal plasticity model*, Acta Materialia, 266, 118232, 2024.

THE ANNALS OF "DUNAREA DE JOS" UNIVERSITY OF GALATI
FASCICLE IX. METALLURGY AND MATERIALS SCIENCE
N°. 1 - 2026, ISSN 2668-4748; e-ISSN 2668-4756
Article DOI: https://doi.org/10.35219/mms.2026.1.03

ANALYSIS AND PROGNOSIS OF SURFACE SUBSIDENCE IN THE JIU VALLEY

Dacian Paul MARIAN
University of Petroşani, Romania
e-mail: dacianmarian@upet.ro

ABSTRACT

Surface subsidence resulting from underground mining activities is a critical environmental and engineering concern that has garnered substantial attention in both academic and practical contexts. The phenomenon occurs when the removal of underground materials, such as coal, minerals, or ores, leads to the collapse or settling of the surface. This study examines mining operations conducted within the thick coal seams of the Jiu Valley Coal Basin in Romania, which utilize longwall mining techniques featuring roof control through caving or top coal caving methods. The analysis focuses on the complex deformations of the ground surface that have occurred over time as a direct result of coal extraction activities in specific mining sectors of the basin. Furthermore, the phenomenon of ground surface subsidence is investigated using the CESAR-LCPC finite element code. The modeling is conducted under the assumptions of elastic and elasto-plastic behavior. A temporal analysis of ground surface deformation is also conducted using a profile function. The results obtained from the modeling are subsequently compared with a comprehensive dataset of in situ measurements.

KEYWORDS: surface subsidence, finite element modeling, underground mining, profile function

1. Generalities

1.1. Mechanisms of Surface Subsidence

The mechanisms underlying surface subsidence are complex and multifaceted, often influenced by geological, hydrological, and mining factors. Subsidence can be categorized into two primary types: immediate and delayed [1]. Immediate subsidence occurs shortly after mining activities commence, while delayed subsidence manifests over a longer timeframe, often years after mining has ceased. The timing and extent of subsidence are influenced by the type of mining method employed, the geological characteristics of the overburden, and the depth and extent of the mined-out area [2].

Numerous studies have explored the mechanics of subsidence. For instance, the work of Zhang *et al.* [3] emphasizes the role of stress redistribution within the overburden strata as a primary driver of subsidence. When coal or minerals are extracted, the stress previously supported by the mined material is redistributed to the surrounding rock, leading to the potential failure of the overburden and resultant surface displacement.

Additionally, the interaction between surface and underground hydrology can exacerbate subsidence. As noted by Xu *et al.* [4], changes in groundwater levels due to mining can lead to increased pore water pressure in the overburden, further destabilizing the surface layers.

1.2. Impacts of Surface Subsidence

The impacts of surface subsidence are extensive and can affect both the environment and human infrastructure [5-7]. One of the most significant concerns is the potential for damage to buildings, roads, and other forms of infrastructure [8, 9]. Research by Li *et al.* [10, 11] highlights the fact that subsidence can lead to structural failures, creating safety hazards and economic burdens for communities. In addition to physical damage, subsidence can also disrupt local ecosystems, affecting soil stability, vegetation, and water drainage patterns [12-14].

The socio-economic implications of subsidence are also noteworthy. Many mining regions are home to vulnerable populations that may not have the

THE ANNALS OF "DUNAREA DE JOS" UNIVERSITY OF GALATI
FASCICLE IX. METALLURGY AND MATERIALS SCIENCE
Nº. 1 - 2026, ISSN 2668-4748; e-ISSN 2668-4756
Article DOI: https://doi.org/10.35219/mms.2026.1.03

resources to adapt to or mitigate the impacts of subsidence. As outlined by O'Neill *et al.* [15], the displacement of communities due to subsidence-related hazards poses significant social challenges, including the loss of livelihoods and cultural heritage. Furthermore, the psychological impacts of living in subsidence-prone areas can lead to increased stress and anxiety among residents [16].

1.3. Impacts of Surface Subsidence

Given the potential consequences of surface subsidence, numerous strategies have been proposed and implemented to mitigate its effects. One common approach is the use of subsidence monitoring systems, which utilize techniques such as InSAR (Interferometric Synthetic Aperture Radar) and ground-based surveys to detect and measure ground movement [17]. These monitoring systems allow for the early detection of subsidence, enabling timely intervention measures.

Another mitigation strategy involves the design of mining operations that minimize subsidence risk. For example, the implementation of stope design principles that maintain a stable roof can reduce the likelihood of immediate subsidence [18]. Additionally, backfilling techniques, in which mined-out areas are filled with waste material, have been shown to effectively reduce subsidence by providing additional support to the overburden [19].

Community engagement and education are also vital components of effective subsidence mitigation. As highlighted by Smith *et al.* [20], involving local communities in monitoring efforts and decision-making processes can enhance resilience and foster a collaborative approach to managing subsidence risks. This participatory approach not only empowers communities but also improves the effectiveness of mitigation strategies by incorporating local knowledge and perspectives.

1.4. General information regarding underground mining in the Jiu Valley

The Petroşani Hard Coal Basin constitutes the most significant hard coal deposit in Romania, with an estimated balance reserve of approximately one billion tons. This coal deposit has been recognized and exploited since 1788, during the era of the Austro-Hungarian Empire. However, substantial coal extraction commenced concurrently with Romania's industrialization following World War II, peaking at over 9 to 10 million tons annually after 1980.

Following the reorganization of the Romanian industrial sector post-1990, in response to the evolving demands of a market economy, coal production from this basin was curtailed to approximately 3.5 million tons per year. Initially, the coal deposit was divided into 16 mining fields; however, subsequent reorganizations and closures have resulted in the operational status of only 7 mining fields.

The complex tectonic structure of the deposit necessitates the delineation of geological blocks of limited extent, typically ranging from 200 to 300 meters, which presents significant technical challenges for mining operations. Furthermore, the deposit is characterized by methane gas emissions, with levels exceeding 10 to 15 cubic meters per ton of coal, and a notable propensity for self-ignition of coal.

The genesis of the deposit is sedimentary, with prevalent rock types in the basin including limestone, marl, argillaceous or marly sandstone, and conglomerate. The strength of these rocks varies between 15–16 MPa and 50–60 MPa, with instances of even higher strength, indicating a general trend of relatively low stability.

The primary factors influencing the stress and strain conditions surrounding excavations resulting from coal seam mining, particularly with respect to roof rock caving in the Jiu Valley Coal Basin, include excavation dimensions, seam inclination, the geomechanical properties of the coal and surrounding materials, mining depth, characteristics of face supports, face advancement rates, and distances from adjacent panels and nearby coal seams.

Through surface measurement analyses conducted under the influence of underground mining, optimal design parameters for the main safety pillars have been established, leading to the determination of subsidence limit angles for various coal mining fields within the Jiu Valley Coal Basin.

This study focuses on analysing the impact of underground mining on the ground surface above coal seam No. 3 in the Uricani, Vulcan, Lonea, and Petrila mines, utilizing a newly developed profile function. Additionally, numerical modeling of the subsidence phenomenon has been performed for the Uricani Mine employing the CESAR-LCPC finite element software.

Typically, the temporal evolution of the subsidence basin is dynamic. As longwall face mining progresses, the length of the panel increases, and the subsidence basin transitions through subcritical, critical, and supercritical stages. Following the cessation of mining activities, the subsidence phenomenon gradually diminishes, coinciding with the settlement of caving rocks, resulting in residual subsidence. A pertinent case study is provided by Panel 5 of coal seam No. 3 at the Livezeni Mine, characterized by a dip of 15-22

THE ANNALS OF "DUNAREA DE JOS" UNIVERSITY OF GALATI
FASCICLE IX. METALLURGY AND MATERIALS SCIENCE
Nº. 1 - 2026, ISSN 2668-4748; e-ISSN 2668-4756
Article DOI: https://doi.org/10.35219/mms.2026.1.03

degrees, a thickness of 12.5 meters, and a mining depth of 340 meters.

The findings from the 2D finite element modeling using the CESAR-LCPC code indicate that the development of the subsidence basin is dynamic and contingent upon various panel mining dimensions. It has been established that at the maximum panel size of approximately 440 meters (the actual length of Panel 5), critical subsidence had not been attained. Critical subsidence is projected to occur at a panel extension of 2000 meters; beyond this threshold, the subsidence is classified as supercritical.

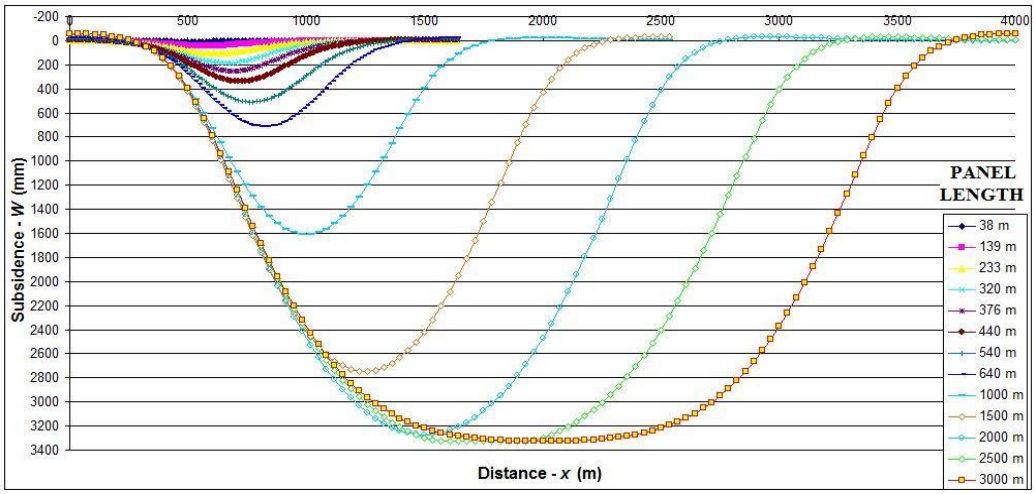

Fig. 1. *Dynamic Subsidence Trough*

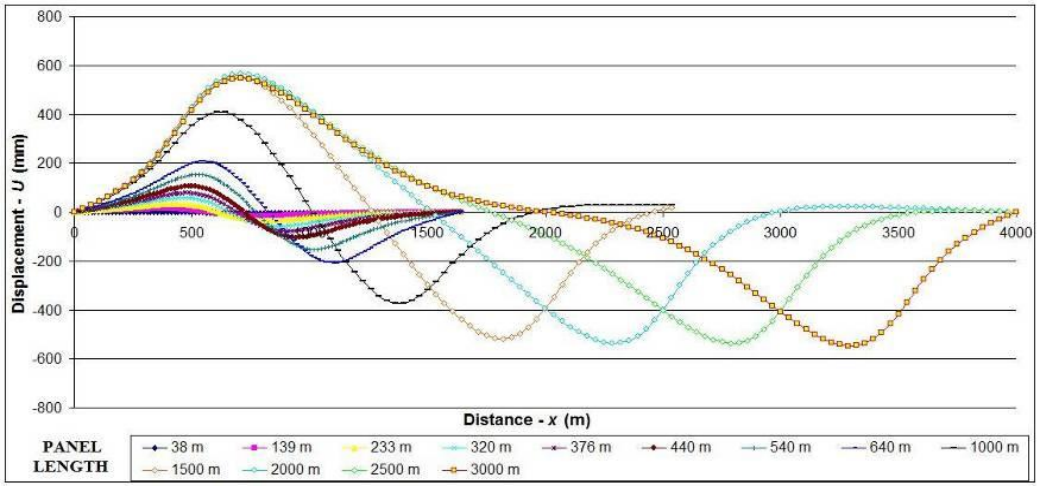

Fig. 2. *Dynamic Horizontal Displacements*

2. An Examination of Subsidence Phenomena Associated with underground mining at the Uricani Mine

The monitoring of ground surface displacement in response to underground mining activities at the Uricani Mine is conducted through a designated monitoring station comprising ten observation benchmarks, spanning a total length of 563.6 meters. Topographical measurements have been systematically performed on a quarterly basis, commencing in October 2007. This monitoring station is instrumental in providing empirical data regarding the displacements and deformations of the ground surface attributable to the exploitation of coal from Seam No. 3, Block V, Panel 1 (Figure 3).

The extraction process involved the mining of a thick, gently inclined coal seam, characterized by an inclination of less than 10 degrees, utilizing the top coal caving longwall mining method. This method was employed over the entire thickness of the seam and across a panel length of 354 meters. The mining operations for this panel commenced in 2003 and reached completion in the latter half of 2007.

THE ANNALS OF "DUNAREA DE JOS" UNIVERSITY OF GALATI
FASCICLE IX. METALLURGY AND MATERIALS SCIENCE
No. 1 - 2026, ISSN 2668-4748; e-ISSN 2668-4756
Article DOI: https://doi.org/10.35219/mms.2026.1.03

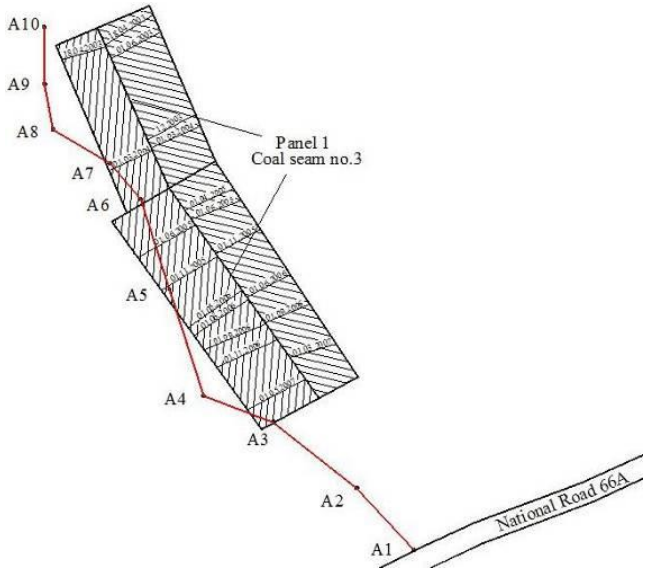

Fig. 3. *Surface displacement monitoring Station, Uricani Mine*

2.1. Statistical Interpretation of the Measurements

The subsidence basins that were measured were subjected to a statistical analysis utilizing a profile function represented by the following equation:

$$W(x) = a \cdot x^{b} \cdot e^{-c \cdot x} \quad (1)$$

To incorporate time into this function, a regression analysis was performed on all regression coefficients as a function of time t. This process yielded a novel generalized profile function that is dependent on time, expressed as follows:

$$W(x,t) = a_1 \cdot t^{a_2} \cdot x^{b_1 \cdot ln(t) + b_2} \cdot e^{-(c_1 \cdot ln(t) + c_2) \cdot x} \quad (2)$$

Where: x is the distance measured from the limit of the subsidence trough; t is time;
$a_1 = 2 \cdot 10^{-31}; b_1 = -2.593; c_1 = -0.0074;$
$a_2 = 12.936; b_2 = 15.365; c_2 = 0.0435$ (R^2=0.971) are the coefficients of regression for this profile function.

Figure 4 illustrates the actual subsidence graphs as a function of time alongside the outcomes generated by the time-dependent profile function.

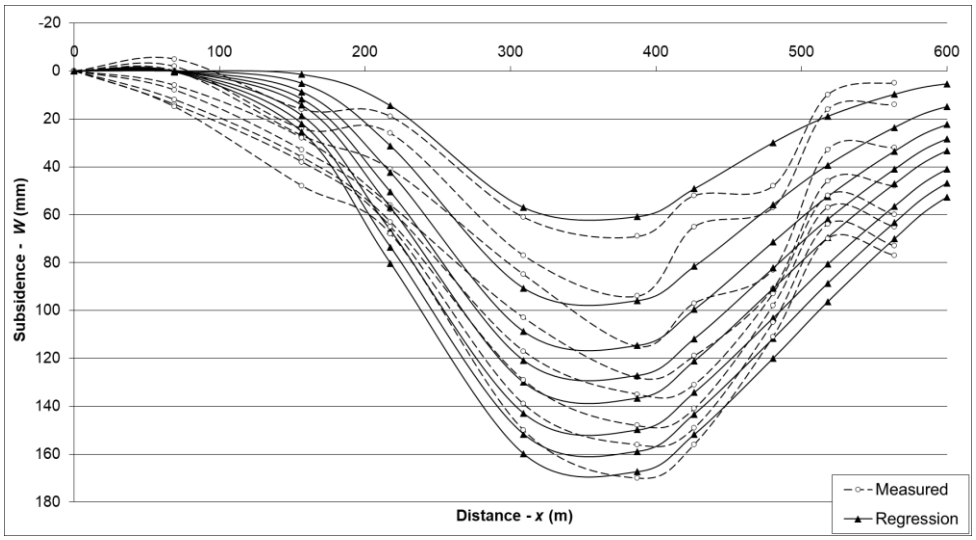

Fig. 4. *Measured subsidence curves and the Corresponding Profile Functions, Uricani Mine*

THE ANNALS OF "DUNAREA DE JOS" UNIVERSITY OF GALATI
FASCICLE IX. METALLURGY AND MATERIALS SCIENCE
No. 1 - 2026, ISSN 2668-4748; e-ISSN 2668-4756
Article DOI: https://doi.org/10.35219/mms.2026.1.03

2.2. 3D Finite Element Modeling

To develop the three-dimensional (3D) finite element computational models, the CESAR-LCPC software, version 4, was employed. In the context of the Uricani Mine, two distinct models were constructed to assess ground surface subsidence and displacement, adhering to the plane strain hypothesis. Model 1 was oriented along the seam dip, as a vertical cross-section at point A6, as shown in Figure 3. The second model was aligned with the seam strike, depicting a directional cross-section through the central portion of the goaf space.

The computations were conducted under the assumption of elasto-plastic behavior without hardening, positing that both the surrounding geological formations and the coal seam are continuous, homogeneous, and isotropic. The geomechanical parameters utilized in the calculations were average values (γ_a = 26.6 kN/m^2, E = 5 035 000 kN/m^2, ν =0.19 and ϕ =55°). Additionally, the caved roof rocks were modeled as a highly compressible medium, characterized by a Young's modulus of E = 15 000 kN/m^2 and a Poisson's ratio of ν =0.4.

To calibrate the models in accordance with the measured values of maximum vertical displacements and to adjust laboratory characteristics to reflect *in situ* rock properties, successive calculations were performed with the characteristic values reduced by 50%, 60%, and 70%, corresponding to structural weakness coefficients K of 0.5, 0.4, and 0.3, respectively, as depicted in Figure 6b.

The initial loading conditions were established as geostatic $[\sigma_o]$, corresponding to a depth of approximately 390 meters. This resulted in vertical geostatic stresses of σ_{oy} = 102.4 MPa; and horizontal geostatic stresses of $\sigma_{ox} = k_o \cdot \sigma_{oy} =$ 24.6 MPa (where:$k_o = \frac{\nu}{1-\nu} = 0.24$). The stresses induced by the excavations were also calculated $[\sigma_e] = [-102.4;\ -24.6]$ MPa. Ultimately, the models were subjected to total stress loading conditions:$[\sigma_T] = [\sigma_o] - [\sigma_e]$.

The analysis indicated that the model with a 60% reduction in characteristics closely approximated real-world conditions. Consequently, the "strike model" was analyzed under the Mohr-Coulomb elasto-plastic behavior hypothesis, incorporating a structural weakness coefficient K of 0.4. In this model, a coefficient was introduced to account for the third dimension (panel width), which reduced the mining void stresses $[\sigma_e]$ by approximately 60%.

For the construction of the 3D finite element models, the CESAR-LCPC finite element code was utilized. The model designated "with mining voids" was developed to evaluate displacements and ground surface deformations in three dimensions, employing an elastic behavior hypothesis that involved reducing the properties of the rocks and coal.

The model dimensions were specified as X = 1354 m, Y = 1100 and Z = 470 m. The meshing of the model, as well as each region, was accomplished with hexahedral elements employing linear interpolation. Thus, a number of 48000 nodes and 44800 volume elements resulted.

The subsidence basins derived from measurements, as well as from both 2D and 3D numerical modeling, were compared along the monitoring station's approximate route, as illustrated in Figures 5 and 6. Figure 6a depicts the displacement along the X-axis obtained from the 3D numerical modeling, following the monitoring station's approximate route shown in Figure 5. A comparison between the numerical model's subsidence basin and the measured subsidence (Figure 5) revealed that while the maximum subsidence values were equivalent, there were deviations in the overall subsidence profile.

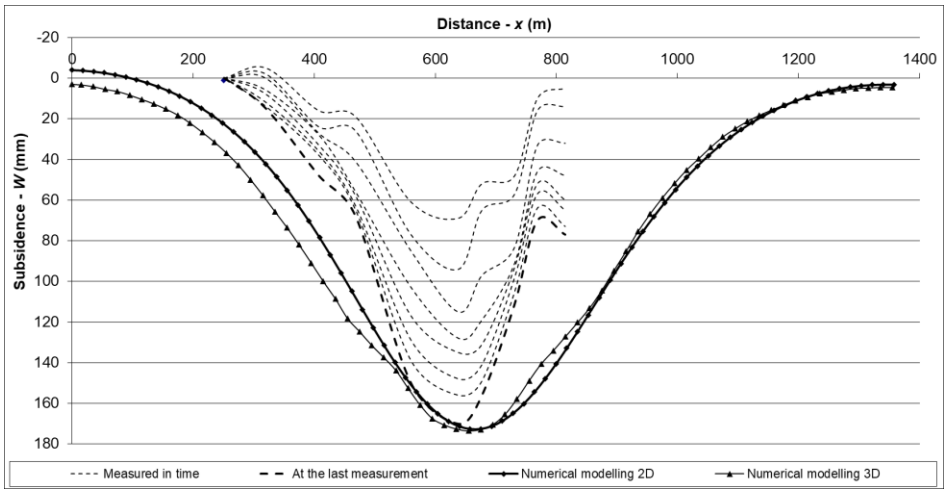

a)

THE ANNALS OF "DUNAREA DE JOS" UNIVERSITY OF GALATI
FASCICLE IX. METALLURGY AND MATERIALS SCIENCE
Nº. 1 - 2026, ISSN 2668-4748; e-ISSN 2668-4756
Article DOI: https://doi.org/10.35219/mms.2026.1.03

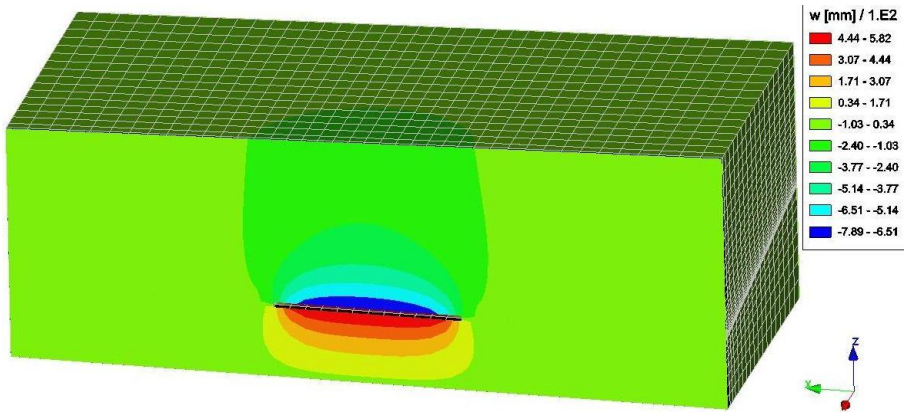

b)

Fig. 5. *Subsidence trough resulted from 3D Numerical Modelling and measured subsidence*

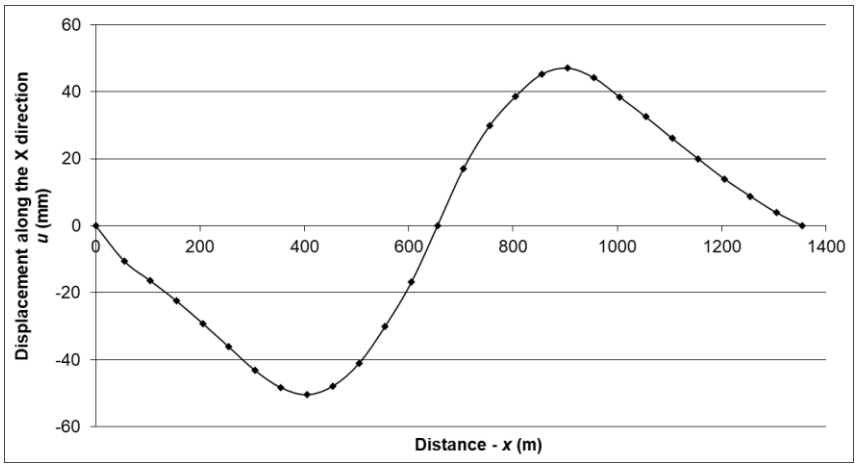

a)

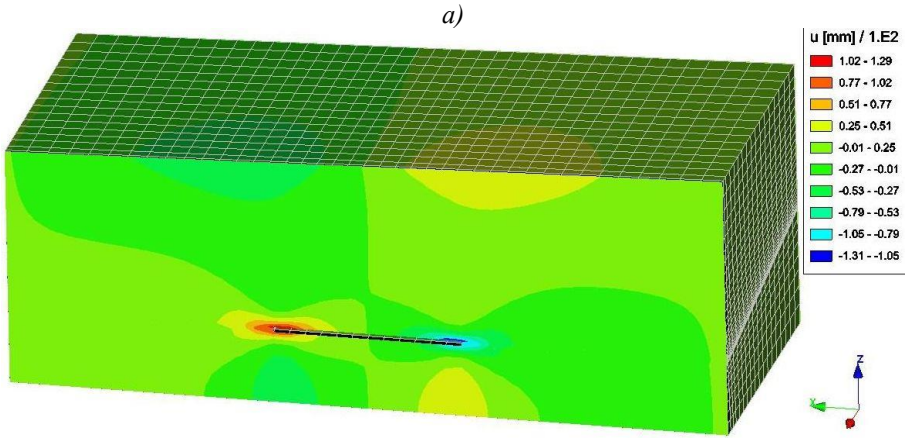

b)

Fig. 6. *Horizontal displacement from 3D Modelling (along the X Direction)*

3. Analysis of Subsidence Associated with Coal Seam No. 3 at the Vulcan Mine

The assessment of ground surface subsidence attributable to underground mining activities at the Vulcan Mine is conducted utilizing a monitoring station comprising 16 benchmarks, which collectively span a length of 620.8 meters. This monitoring station is instrumental in providing data regarding ground surface subsidence and deformation resulting from the extraction of coal seam No. 3, specifically within Block VII-VIII, at Faces No. 366 and 376 (Figure 7).

Coal seam No. 3, characterized by an average thickness of approximately 50 meters, is extracted

THE ANNALS OF "DUNAREA DE JOS" UNIVERSITY OF GALATI
FASCICLE IX. METALLURGY AND MATERIALS SCIENCE
No. 1 - 2026, ISSN 2668-4748; e-ISSN 2668-4756
Article DOI: https://doi.org/10.35219/mms.2026.1.03

using a top coal caving mining method, which is associated with the aforementioned coal faces. The commencement of mining operations dates back to 1964, at which time a roof control technique involving rock caving was implemented.

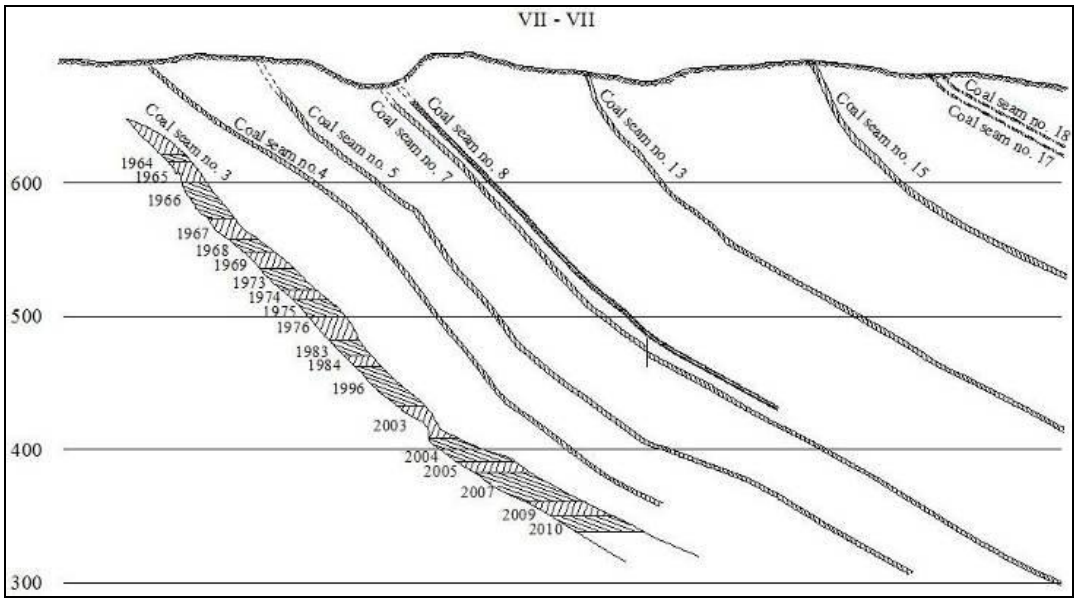

Fig. 7. *Cross - Section, Vulcan Mine*

Following the statistical interpretation of the measurements utilizing the profile function (1), a regression operation was conducted to determine the coefficients of regression for each measurement phase. Consequently, the generalized time-dependent profile function (2*)* was derived, yielding a coefficient of determination R^2 of 0.95 $a_1 = 7 \cdot 10^{-13}$; $b_1 = -4.186; c_1 = -0.0113;$ $a_2 = 21.23;\ b_2 = 60.35; c_2 = 0.1363$

The subsidence curves, which were measured periodically, along with the approximation curves of the time-dependent profile function, are graphically depicted in Figure 8. This figure illustrates a strong correlation between the *in-situ* measurements and the model, as evidenced by the high R^2 value of 0.95.

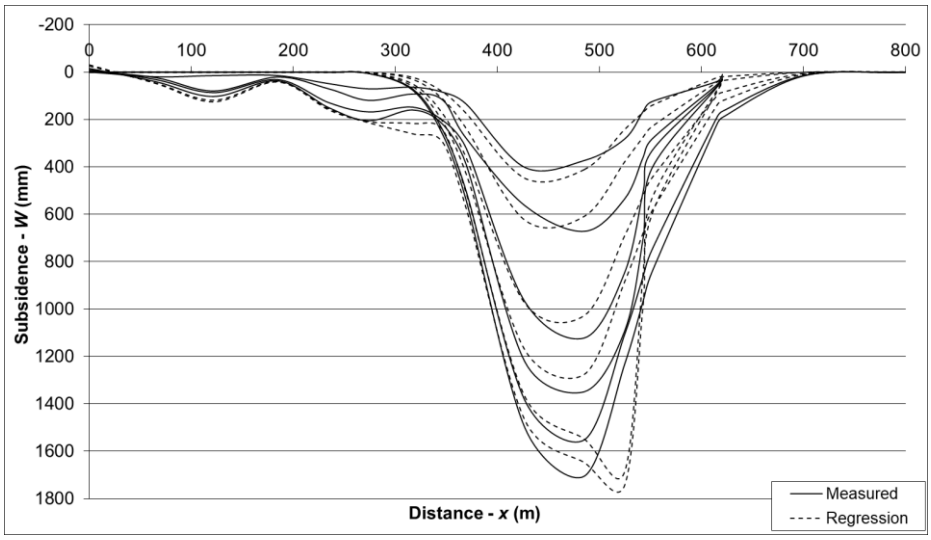

Fig. 8. *Measured subsidence and the temporal profile function curves at Vulcan Mine*

THE ANNALS OF "DUNAREA DE JOS" UNIVERSITY OF GALATI
FASCICLE IX. METALLURGY AND MATERIALS SCIENCE
No. 1 - 2026, ISSN 2668-4748; e-ISSN 2668-4756
Article DOI: https://doi.org/10.35219/mms.2026.1.03

4. Surface Subsidence Analysis in the case of Petrila Mine

The measurements conducted along the alignment designated as 200, which was established in 1981, comprise 16 monitoring benchmarks arranged at intervals of 250 meters. Since 1978, mining operations for coal seam No. 3, located beneath the elevation of +300 meters, have been executed using a slice method, employing roof control through caving in the areas corresponding to Faces No. 138 and 139. By 1991, complete extraction was attained at Face No. 139 at the elevation of +200 meters.

Consistent with prior analyses, the statistical evaluation of the measurements was performed utilizing the profile function (1) and the generalized time-dependent function (2), resulting in the following regression coefficient of R^2 = 0.981: $a_1 = 2{,}69 \cdot 10^{-4}; b_1 = -0{,}36; c_1 = -0{,}0025;$ $a_2 = 2{,}414; b_2 = 2{,}828; c_2 = 0{,}019876.$

The surface subsidence graphs derived from the data, alongside the results obtained from the profile function, are illustrated in Figure 11.

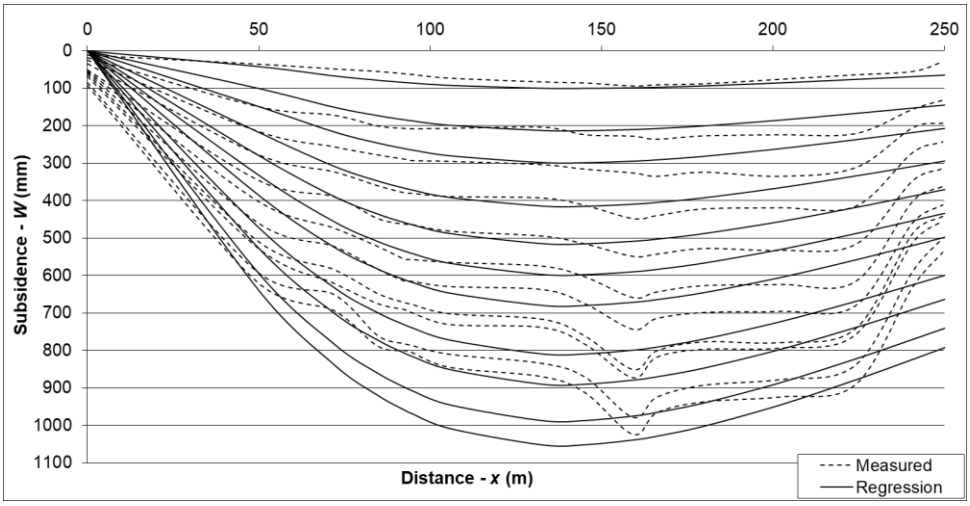

Fig. 11. *Measured subsidence and the temporal profile function curves at Petrila Mine*

5. Future research directions

Despite the progress made in understanding and addressing surface subsidence, several gaps in the literature remain. Future research should focus on the development of more sophisticated predictive models that account for the complex interactions between geological, hydrological, and anthropogenic factors influencing subsidence [21]. Additionally, there is a need for interdisciplinary studies that integrate geotechnical engineering, environmental science, and the social sciences to comprehensively address the multifaceted impacts of subsidence.

Moreover, the role of climate change in exacerbating subsidence risks warrants further investigation. Changes in precipitation patterns and increased frequency of extreme weather events can alter groundwater dynamics and influence subsidence behavior [22]. Understanding these interactions will be crucial for developing adaptive management strategies in mining regions.

Finally, the implementation of innovative technologies, such as machine learning and artificial intelligence, in subsidence monitoring and prediction presents an exciting avenue for future research. These technologies have the potential to enhance the accuracy and efficiency of subsidence assessments, ultimately leading to more effective mitigation strategies [23].

6. Conclusions

In summary, surface subsidence resulting from underground mining is a complex phenomenon with significant environmental, social, and economic implications. A comprehensive understanding of the mechanisms, impacts, and mitigation strategies associated with subsidence is essential for effective management and policy development in mining regions. The existing literature provides a solid foundation for future research, which should continue to explore innovative solutions and interdisciplinary approaches to address the challenges posed by subsidence. By doing so, we can better safeguard communities and ecosystems affected by underground mining activities.

Simultaneously with the reevaluation of the mining activities associated with the Jiu Valley hard coal deposit, necessitated by the closure of some

mining units and the initiation of new panel mining operations, there has emerged a pressing need to reassess the stability of surface lands and the integrity of existing structures. This context has highlighted the importance of evaluating ground surface stability in areas influenced by mining operations. Consequently, an intensive effort was made to assess historical measurements across various mining fields in the Jiu Valley, alongside an analysis of the associated data repository maintained by the Hard Coal Company of Petroșani. This paper presents several significant case studies derived from this analysis.

It is noteworthy that the data analysis encountered challenges because ground surface monitoring was conducted along monitoring stations which were not relevant from a scientific perspective. The main purpose of these monitoring stations was to monitor the behavior of features located in the exploitation's area of influence (roads, constructions, and land parcels.

As a result of this investigation, a time-dependent profile function was developed and validated, which can be used to predict the temporal evolution of subsidence trough resulting from underground mining (the function was validated using specific cases from the Jiu Valley). In addition to the profile function methodology, the subsidence phenomenon was also analyzed using the 3D finite element method. The calculations were executed under conditions of elasticity and elasto-plasticity, incorporating models that accounted for mining voids and caved zones. Following a sensitivity analysis and model calibration, significant results were achieved that are pertinent to the geological and mining conditions of the Jiu Valley.

References

[1]. Bel R., Donnelly L., *Mechanisms of surface subsidence in coal mining regions*, Journal of Mining Science, 42(3), p. 227-235, 2006.

[2]. Cheng Y., *et al.*, *A review of surface subsidence prediction models in mining areas*, Environmental Earth Sciences, 71(8), p. 3653-3665, 2014.

[3]. Zhang Y., *et al.*, *Stress redistribution and its role in surface subsidence due to mining*, Geotechnique, 68(4), p. 332-340, 2018.

[4]. Xu C., *et al.*, *The influence of groundwater on subsidence in mining areas: A case study*, Hydrogeology Journal, 25(5), p. 1351-1365, 2017.

[5]. Floarea D. A., *et al.*, *Necessity of Following up the Land Surface Deformation for Closed Mining Areas*, International Multidisciplinary Scientific GeoConference - SGEM 2015, Sofia, Bulgaria, vol. 5, issue 2, p. 733-738, 2015.

[6]. Onica I., Marian D. P., *Introduction to finite element modeling. Stability of mining excavations*, Universitas Publishing House, Petroșani, 2016.

[7]. Onica I., *et al.*, *Prognosis of the Maximum Subsidence and Displacement of the Ground Surface in the Jiu Valley Coal Basin Conditions*, International Multidisciplinary Scientific GeoConference - SGEM 2014, Sofia, Bulgaria, vol. 3, p. 465, 2014.

[8]. Floarea D. A., *et al.*, *Necessity of Subsidence Phenomenon Monitoring in the Case of Sustainable Development of Jiu Valley Coal Basin Conditions*, Annals of the University of Petrosani Mining Engineering, vol. 15, 2014.

[9]. Marian D. P., *et al.*, *Sensibility Analysis of the Subsidence Parameters at the Variation of the Main Geo-Mining Factors*, Mining Revue/Revista Minelor, vol. 17, issue 3, 2011.

[10]. Li J., *et al.*, *Structural impacts of surface subsidence on urban infrastructure*, Journal of Structural Engineering, 141(10), 04015039, 2015.

[11]. Marian R. R., *et al.*, *3D Finite Element Analysis of Deformation of Buildings Located in Areas Affected by Underground Mining*, International Multidisciplinary Scientific GeoConference: SGEM 2018, vol. 18, issue 1.3, p. 3-10, 2018.

[12]. Huang Y., *et al.*, *Ecological impacts of surface subsidence in mining areas: A review*, Environmental Management, 63(5), p. 663-674, 2019.

[13]. Marian D. P., *et al.*, *Surface Subsidence Prognosis Using the Influence Function Method in the Case of Livezeni Mine*, Mining Revue/Revista Minelor, vol. 23, issue 1, 2017.

[14]. Onica I., Marian D. P., *Applications of the finite element method in the analysis of surface stability and underground structures*, Universitas Publishing House, Petrosani, 2016.

[15]. O'Neill P., *et al.*, *Socio-economic impacts of subsidence on mining communities*, Resources Policy, 68, 101724, 2020.

[16]. Miller R., *et al.*, *Psychological impacts of living in subsidence-prone areas*. Journal of Environmental Psychology, 75, 101629, 2021.

[17]. Bock Y., *et al.*, *Monitoring ground deformation using InSAR: Applications to mining subsidence*, Geophysical Research Letters, 43(10), p. 4904-4911, 2016.

[18]. Bishop D., *et al.*, *Stope design principles for minimizing subsidence risk*, International Journal of Mining Science and Technology, 28(4), p. 617-625, 2018.

[19]. Chen H., *et al.*, *The effectiveness of backfilling techniques in reducing surface subsidence*, Mining Engineering, 71(6), p. 49-58, 2019.

[20]. Smith T., *et al.*, *Community engagement in subsidence monitoring: Lessons learned*, Journal of Community Engagement and Scholarship, 13(1), p. 45-56, 2020.

[21]. Kumar A., *et al.*, *Predictive modeling of subsidence in coal mining areas: A review*, International Journal of Coal Geology, 253, 103889, 2021.

[22]. Feng X., *et al.*, *Climate change impacts on groundwater dynamics and subsidence in mining regions*, Water Resources Research, 58(3), e2021WR030123, 2022.

[23]. Zhang L., *et al.*, *Application of machine learning in subsidence prediction and monitoring*, Computers and Geotechnics, 139, 104290, 2023.

THE ANNALS OF "DUNAREA DE JOS" UNIVERSITY OF GALATI
FASCICLE IX. METALLURGY AND MATERIALS SCIENCE
Nº. 1 - 2026, ISSN 2668-4748; e-ISSN 2668-4756
Article DOI: https://doi.org/10.35219/mms.2026.1.04

ADDITIVELY MANUFACTURED TPU ACOUSTIC METAMATERIALS FOR HIGH-FREQUENCY NOISE MITIGATION IN DENTAL ROTARY INSTRUMENTS

Emilian CHIFOR[1], Florin-Bogdan MARIN[1,2], Mihaela MARIN[1,2]
[1] "Dunarea de Jos" University of Galati, Romania
[2] Interdisciplinary Research Centre in the Field of Eco-Nano Technology and Advanced Materials CC-ITI, Faculty of Engineering, "Dunarea de Jos" University of Galati, Romania, 47 Domnească Street, RO-800008, Galaţi, Romania
e-mail: flmarin@ugal.ro

ABSTRACT

Noise generated by high-speed dental turbines represents a persistent challenge in dental clinics, affecting both patient comfort and the occupational well-being of medical staff. This study investigates the potential of additively manufactured thermoplastic polyurethane (TPU) acoustic metamaterials for high-frequency noise mitigation in dental applications. A layered metamaterial panel based on periodic hexagonal unit cells is proposed and numerically evaluated as a compact and frequency-selective acoustic treatment. A vibro-acoustic simulation framework is employed to assess the sound transmission loss (STL) performance of the proposed metamaterial in comparison with a solid TPU panel of equivalent thickness. Two configurations are analysed: a reference case without acoustic treatment and a modified case in which the TPU-based metamaterial is integrated onto the head of a dental rotary bur. Overall, the findings highlight the effectiveness of compact TPU-based acoustic metamaterials as a promising solution for targeted noise mitigation in dental environments. The proposed approach combines acoustic efficiency, design flexibility, and compatibility with additive manufacturing, thereby facilitating its potential integration into dental equipment and clinical noise control strategies.

KEYWORDS: panoramic dental radiography; metallic restoration detection; computer vision; image processing

1. Introduction

Noise pollution represents a significant challenge in medical environments, where excessive acoustic disturbances can negatively affect patient comfort, staff performance, and the accuracy of medical procedures. Hospitals and clinical facilities are characterized by complex acoustic conditions generated by medical equipment, ventilation systems, alarms, and human activity.

In recent years, acoustic metamaterials have emerged as a promising solution for advanced noise control due to their ability to manipulate sound propagation beyond the limitations of conventional materials [1-4]. By exploiting engineered subwavelength structures, metamaterials enable [5] the targeted attenuation of specific frequency bands, offering new opportunities for noise mitigation in sensitive medical settings.

This work investigates the potential of metamaterial-based solutions for noise reduction in the medical industry, focusing on their underlying principles, design considerations, and applicability in real-world clinical environments. Traditional noise mitigation strategies in medical facilities typically rely on passive absorbers, barriers, or architectural modifications. While effective to a certain extent, these approaches often require substantial space, provide broadband but limited attenuation, and lack adaptability to varying noise sources.

Medical environments impose strict constraints related to hygiene, safety, compactness, and compatibility with existing equipment. Consequently, there is a strong demand for compact, lightweight, and frequency-selective noise mitigation solutions

THE ANNALS OF "DUNAREA DE JOS" UNIVERSITY OF GALATI
FASCICLE IX. METALLURGY AND MATERIALS SCIENCE
Nº. 1 - 2026, ISSN 2668-4748; e-ISSN 2668-4756
Article DOI: https://doi.org/10.35219/mms.2026.1.04

that can be seamlessly integrated into medical devices and infrastructures.

Metamaterials address these requirements by enabling tailored acoustic responses, including negative effective mass density or bulk modulus, which allow for efficient attenuation of low-frequency noise that is otherwise difficult to suppress. This capability makes metamaterials particularly attractive for medical applications such as diagnostic rooms, intensive care units, and operating theatres [9-11].

Noise exposure in dental clinics represents a well-recognized occupational and patient-related issue, with potential implications for comfort, concentration, and long-term auditory health [6-8]. Modern dental procedures rely heavily on high-speed rotary instruments, among which the dental turbine is the predominant source of acoustic disturbance [9-14]. During clinical operation, dental turbines generate elevated sound pressure levels, typically ranging from 75 to 85 dB(A), with dominant spectral components located in the high-frequency range where human auditory sensitivity is maximal.

Prolonged exposure to such noise has been associated with increased stress levels in patients and cumulative auditory fatigue among dental professionals [14-18]. Moreover, the tonal and high-frequency nature of turbine-generated noise contributes to heightened discomfort, making effective noise mitigation strategies particularly relevant in clinical settings [17].

Conventional noise reduction approaches in dental clinics primarily involve passive acoustic treatments, equipment enclosures, or architectural modifications. While these solutions can provide partial attenuation, they are often bulky, broadband in nature, and difficult to integrate into compact clinical settings. In addition, standard acoustic materials typically exhibit limited performance in the high-frequency regime unless significant thickness is employed, which is impractical for many dental applications.

Recent advances in acoustic metamaterials offer new opportunities for targeted noise mitigation. By exploiting engineered microstructures and local resonance phenomena, metamaterials enable frequency-selective attenuation and enhanced damping within compact form factors. In this context, thermoplastic polyurethane (TPU) has emerged as a promising material due to its intrinsic viscoelastic damping properties, mechanical flexibility, and compatibility with additive manufacturing technologies.

This work investigates the potential of a TPU-based acoustic metamaterial, designed as a layered structure with stacked hexagonal unit cells, for reducing turbine-generated noise in dental clinics. A numerical vibro-acoustic simulation framework is employed to evaluate the sound transmission loss (STL) through the proposed structure, with a specific emphasis on the clinically relevant 3–6 kHz frequency band. The study aims to demonstrate that compact, additively manufactured TPU metamaterials can provide effective and application-oriented noise mitigation solutions for dental environments.

2. Experimental procedure

This study adopts a multidisciplinary methodology combining acoustic theory, numerical simulation, and metamaterial design to investigate noise mitigation solutions for medical environments. In particular, the proposed approach integrates computational fluid dynamics (CFD)–based acoustic simulations with the structural modeling of hexagonal layered metamaterial cells, enabling detailed analysis of sound–structure interaction in the case of a dental rotary bur.

The methodology consists of the following main steps:

The acoustic metamaterial is modeled as a stacked arrangement of hexagonal unit cells, selected for their structural symmetry, efficient space-filling properties, and mechanical stability. The primary noise source considered in this study is the high-speed dental turbine, which is known to generate elevated sound pressure levels with dominant spectral components in the high-frequency range. Based on reported clinical measurements, the turbine produces sound pressure levels of approximately 75 dB(A), with pronounced peaks in the 5 kHz frequency band.

Accordingly, the objective of the simulation is to evaluate the effectiveness of a TPU-based metamaterial structure in attenuating airborne noise within the 1–8 kHz frequency range, with a specific emphasis on the clinically relevant 3–6 kHz band. The metamaterial is positioned on the dental rotary bur head (Fig. 2).

The proposed noise mitigation solution consists of a TPU-based acoustic metamaterial panel, designed as a layered structure composed of stacked hexagonal unit cells. This geometry was selected due to its structural symmetry, high porosity control, and capability to induce local resonances and enhanced damping effects.

The geometry consists of elongated hexagonal unit cells arranged in a longitudinally periodic lattice within a rectangular domain (Fig. 1). Key geometric parameters, including unit cell dimensions, wall thickness, and repetition pitch, are explicitly defined to enable fine-tuning of the effective mechanical and vibro-acoustic properties. Such structures are suitable for finite element analysis, parametric optimization,

THE ANNALS OF "DUNAREA DE JOS" UNIVERSITY OF GALATI
FASCICLE IX. METALLURGY AND MATERIALS SCIENCE
Nº. 1 - 2026, ISSN 2668-4748; e-ISSN 2668-4756
Article DOI: https://doi.org/10.35219/mms.2026.1.04

and the additive manufacturing of lightweight functional components.

The TPU material is modeled as a viscoelastic polymer with frequency-independent elastic properties for the baseline simulations. Density, Young's modulus, and Poisson's ratio are defined based on manufacturer datasheets for medical-grade TPU 95A commonly used in additive manufacturing. Structural damping is introduced via a loss factor to capture the inherent energy dissipation characteristics of TPU.

To evaluate sound transmission through the metamaterial panel, a vibro-acoustic simulation framework is employed. The study investigates two scenarios: (i) a reference configuration without a metamaterial panel and (ii) a configuration in which the proposed metamaterial is integrated onto the head of the dental rotary bur.

This coupled formulation enables the assessment of both airborne sound transmission and structure-borne vibration effects, which are critical for accurate STL prediction.

The numerical simulations are implemented using Altair SimLab.

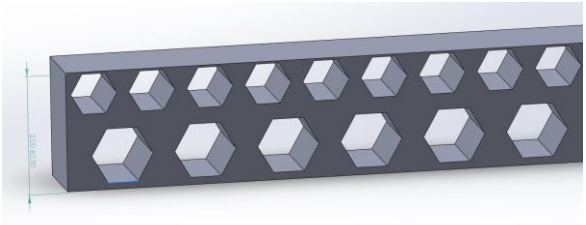

Fig. 1. *Metamaterial structure*

Comparing the two simulation results, a clear improvement in noise mitigation performance is observed in the second configuration. In the first image, the acoustic pressure field exhibits an extended region of elevated sound pressure levels, with high-intensity zones propagating farther from the dental turbine along the main emission direction. This indicates a more efficient transmission of acoustic energy into the surrounding air domain.

In contrast, the second image shows a noticeable reduction in both the magnitude and spatial distribution of the acoustic pressure field. High sound pressure level regions are more confined to the vicinity of the source, and the transition toward lower pressure levels occurs at a shorter distance from the turbine. Based on the colour scale and the contraction of the high-intensity regions, an estimated reduction of approximately 6–10 dB in peak sound pressure level is achieved in the second case.

This reduction is accompanied by a significant decrease in the directional propagation of the acoustic wave, suggesting enhanced dissipation and absorption of acoustic energy. The observed behavior is consistent with the presence of an acoustic treatment that introduces additional damping and scattering mechanisms, leading to faster attenuation of the sound field. Overall, the comparison demonstrates that the second configuration provides a more effective noise mitigation solution, resulting in a substantial reduction of turbine-generated noise under identical simulation conditions.

This parametric analysis enables the identification of optimal design configurations that maximize noise attenuation in the target frequency band while maintaining minimal panel thickness.

Acoustic propagation through and around the metamaterial structure was investigated using CFD-based simulations, employing the linearized Navier–Stokes equations coupled with acoustic wave formulations. The simulations model the interaction between incident acoustic waves and the hexagonal metamaterial layers, allowing for the evaluation of pressure fields, velocity distributions, and sound transmission loss. Appropriate boundary conditions were applied to represent reflective, absorptive, or open acoustic environments typical of medical facilities.

3. Results and discussions

The modal analysis performed on the TPU-based metamaterial panel revealed multiple vibration modes within the targeted frequency range. In contrast to the solid TPU reference panel, the hexagonal layered configuration exhibited a higher density of local resonance modes between 3 and 6 kHz. These modes are primarily associated with the deformation of the hexagonal cell walls and inter-layer coupling effects.

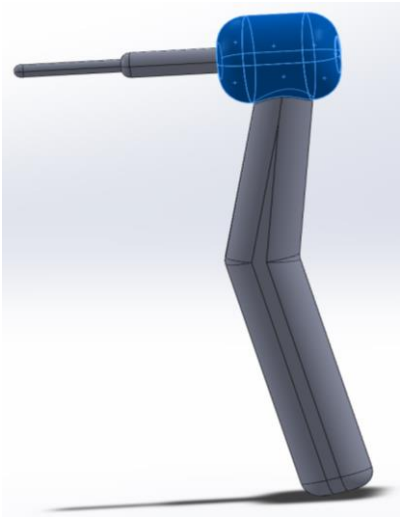

Fig. 2. *Placement of the metamaterial*

THE ANNALS OF "DUNAREA DE JOS" UNIVERSITY OF GALATI
FASCICLE IX. METALLURGY AND MATERIALS SCIENCE
Nº. 1 - 2026, ISSN 2668-4748; e-ISSN 2668-4756
Article DOI: https://doi.org/10.35219/mms.2026.1.04

The presence of these localized resonances indicates an increased potential for energy dissipation through viscoelastic damping, which is expected to enhance acoustic attenuation within the corresponding frequency bands.

Figure 3 illustrates the simulated sound transmission loss (STL) as a function of frequency for both the solid TPU panel and the TPU metamaterial panel with stacked hexagonal cells. The solid TPU panel exhibits a gradual increase in STL with frequency, consistent with mass-law behavior, but provides limited attenuation within the critical 3–6 kHz band.

In contrast, the TPU metamaterial panel demonstrates a pronounced improvement in STL performance. Distinct attenuation peaks are observed within the 3–6 kHz range, coinciding with the identified structural resonance frequencies. In this band, the metamaterial panel achieves an STL increase of approximately 8–15 dB compared to the solid TPU reference, varying on the specific unit cell dimensions and number of layers.

The results highlight the frequency-selective nature of the proposed metamaterial design. While both configurations provide comparable attenuation at lower frequencies, the hexagonal layered structure exhibits superior performance in the high-frequency range associated with dental turbine noise.

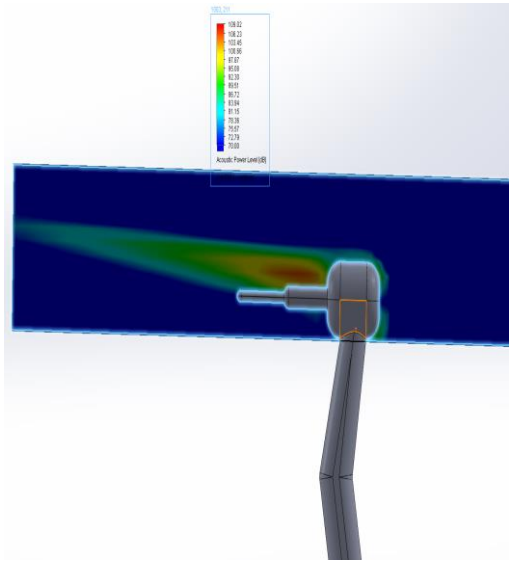

Fig. 3. *Sound level in case of no panel*

This behavior confirms that the attenuation mechanism is not solely governed by panel mass but is strongly influenced by the engineered geometry of the metamaterial. The stacked hexagonal cells act as locally resonant elements, inducing bandgap-like behavior and enhancing sound energy dissipation within targeted frequency intervals.

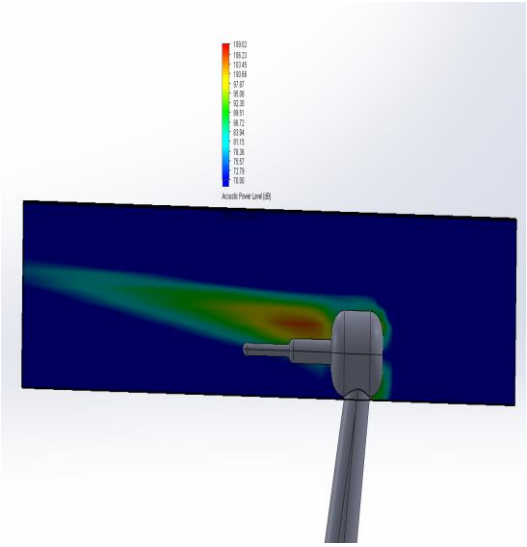

Fig. 4. *Sound level distribution in case panel is applied*

A parametric analysis indicates that the acoustic performance of the metamaterial panel is sensitive to the geometric characteristics of the hexagonal cells. Increasing the unit cell size or the total panel thickness shifts the STL peaks toward lower frequencies, whereas reducing these parameters shifts attenuation peaks to higher frequencies.

The results demonstrate that through appropriate tuning of the hexagonal cell dimensions and layering strategies, the metamaterial panel can be optimized to specifically target the dominant spectral components of dental turbine noise.

These findings suggest that compact TPU metamaterial panels can outperform conventional polymer-based acoustic treatments in dental environments, particularly for high-frequency noise mitigation. The results obtained from the vibro-acoustic simulations demonstrate that the proposed TPU-based metamaterial panel provides a significant improvement in sound transmission loss compared to a solid TPU panel of equivalent thickness. This improvement is particularly evident within the 3–6 kHz frequency band, which corresponds to the dominant spectral components of dental turbine noise and the region of maximum human auditory sensitivity.

The enhanced STL performance can be primarily attributed to the engineered hexagonal layered geometry, which introduces local resonance phenomena and increases structural compliance at targeted frequencies. Unlike conventional homogeneous panels, where sound attenuation is largely governed by the mass law, the metamaterial configuration enables frequency-selective attenuation through resonance-driven energy dissipation and the viscoelastic damping of the TPU material.

THE ANNALS OF "DUNAREA DE JOS" UNIVERSITY OF GALATI
FASCICLE IX. METALLURGY AND MATERIALS SCIENCE
Nº. 1 - 2026, ISSN 2668-4748; e-ISSN 2668-4756
Article DOI: https://doi.org/10.35219/mms.2026.1.04

The modal analysis supports this interpretation by revealing a higher density of structural modes in the metamaterial panel within the critical frequency range. These modes facilitate stronger vibro-acoustic coupling, resulting in increased sound energy absorption and reduced acoustic transmission. The observed attenuation peaks align well with the predicted resonance frequencies of the hexagonal unit cells, confirming the effectiveness of the design strategy.

From an application perspective, the ability to achieve an additional 8–15 dB STL improvement without increasing panel thickness or mass is particularly relevant to dental environments, where space constraints and ergonomic considerations are critical. The use of TPU further enhances applicability, as the material offers favourable damping properties, mechanical flexibility, and compatibility with additive manufacturing processes.

Nevertheless, the results should be interpreted within the context of the study's limitations. The simulations assume idealized boundary conditions and linear material behavior, which may differ from real clinical settings. Furthermore, the current analysis focuses on airborne noise transmission and does not explicitly address structure-borne vibration pathways through dental equipment. These aspects warrant further investigation through experimental validation and extended modeling.

Overall, the findings indicate that TPU-based acoustic metamaterials represent a promising and practical solution for mitigating high-frequency noise generated by dental turbines, offering significant advantages over conventional polymer-based acoustic treatments in terms of efficiency and design flexibility.

4. Conclusions

This study investigated the potential of a TPU-based acoustic metamaterial for mitigating noise generated by high-speed dental turbines, which represent one of the primary acoustic disturbances in dental clinics. A vibro-acoustic simulation framework was employed to evaluate the sound transmission loss of a layered hexagonal metamaterial panel and to compare its performance to a conventional solid TPU panel of equivalent thickness.

The numerical results demonstrate that the proposed metamaterial configuration provides a substantial improvement in acoustic attenuation, particularly within the 3–6 kHz frequency range most relevant to turbine-generated noise and human auditory sensitivity. Compared to the solid TPU reference, the metamaterial panels achieved an additional 8–15 dB increase in STL without increasing panel thickness or mass.

The enhanced performance is attributed to the combined effects of local resonance phenomena induced by the hexagonal cell geometry and the intrinsic viscoelastic damping properties of TPU. These mechanisms enable frequency-selective noise mitigation beyond the limitations of conventional mass-based acoustic treatments.

Overall, the findings confirm that compact, additively manufactured TPU metamaterials represent a promising solution for noise reduction in dental environments. The proposed approach offers a balance between acoustic efficiency, design flexibility, and practical applicability, making it suitable for integration into dental equipment housings, liners, or localized acoustic barriers. Future work will focus on experimental validation, optimization for manufacturing constraints, and extending the approach to multi-source noise mitigation scenarios within clinical settings.

Despite the promising results obtained in this study, several limitations must be acknowledged. First, the analysis is based exclusively on numerical vibro-acoustic simulations performed under idealized boundary conditions. While these simulations provide valuable insights into the noise mitigation potential of the proposed TPU metamaterial, real dental environments exhibit more complex acoustic characteristics, including reverberation, equipment-induced structural vibrations, and variable source–receiver configurations.

Future work will therefore concentrate on experimental validation using additively manufactured TPU prototypes and controlled acoustic measurements in laboratory or simulated clinical environments. Parametric optimization studies will be extended to include a wider range of geometric configurations, material properties, and manufacturing constraints. Furthermore, the integration of adaptive or multi-material designs may enable tuneable and broadband noise mitigation tailored to diverse dental equipment and operational conditions.

References

[1]. Yao K., *et al.*, *A comprehensive review of acoustic metamaterials: Mechanisms, design strategies, and applications*, Materials & Design, 274, 112832, 2025.
[2]. Lu Z., *et al.*, *Bio-inspired acoustic metamaterials for traffic noise control*, Communications Engineering, 4(1), 12, 2025.
[3]. Ciaburro G., *Optimizing Controlled-Resonance Acoustic Metamaterials for Advanced Engineering Applications*, Acoustics, 13(2), 11, 2025.
[4]. Comandini M., *Architected acoustic metamaterials: an integrated design approach for wave propagation control*, HAL Open Science, hal-05057221, 2025.
[5]. Tan J., *Active Acoustic Metamaterials for High Performance Noise Control (Doctoral dissertation)*, University of Southampton, School of Engineering, 2022.

[6]. Berger E. H., *Hearing protector performance: How they Work-And-What Goes Wrong in the Real World: EAR Division*, Cabor Corporation, 1983.
[7]. Da Cunha K. F., *et al.*, *Assessment of noise intensity in a dental teaching clinic*, BDJ Open, 3:17010. https://doi.org/10.1038/bdjopen.2017.10, 2017.
[8]. Lavanya S., *et al.*, *High speed handpiece- A Narrative Review*, J Orofacial Rehab., 4(2), p. 11-19, DOI: 10.5281/zenodo.13356703, 2024.
[9]. Bhandary N., *et al.*, *Short Communication High speed handpieces*, J Int Oral Health, 2014.
[10]. Shankar Narayan G., Sundaram Rajasekaran M., *Evolution and mechanism of dental handpieces*, J Curr Res Aca Rev., 2018.
[11]. Jo Y., *et al.*, *A study on the psychological noise reduction effect through sound masking for dental handpiece noise*, 2022.
[12]. Jiang P., *et al.*, *Dental drill noise reduction using commercially-available devices*, 2023.
[13]. Jiang P., *A Passive Noise Attenuation Earplug Designed to Minimise Unwanted Air Turbine Driven High-Speed Dental Drill Noise*, Applied Acoustics, 2023.
[14]. Jiang P., *Dental Drill Noise Reduction Using a Commercially Available Passive Resonator Device*, Journal of the Royal Society Interface, 2023.
[15]. ***, *Passive Noise Cancelling Device for Dental Drill Noise Reduction*, World Intellectual Property Organization, WO2015011449A1, 2015.
[16]. Lee W., Kwon H.-B., *Vibroacoustic Analysis and Noise Control of High-Speed Dental Air Turbine Handpieces*, Journal of Dental Research, 2022.
[17]. Zhang Z., *et al.*, *Acoustic Metamaterials with Subwavelength Resonators for High-Frequency Noise Attenuation*, Applied Physics Letters, 2021.
[18]. Ma G., Sheng P., *Acoustic Metamaterials: From Local Resonances to Broad Applications*, Science Advances, 2016.

THE ANNALS OF "DUNAREA DE JOS" UNIVERSITY OF GALATI
FASCICLE IX. METALLURGY AND MATERIALS SCIENCE
Nº. 1 - 2026, ISSN 2668-4748; e-ISSN 2668-4756
Article DOI: https://doi.org/10.35219/mms.2026.1.05

BUILDINGS OF THE FUTURE: CHALLENGES OR OPPORTUNITIES?

Simona STANCA
Technical University of Cluj-Napoca, Buildings and Management Department, Romania
e-mail: simona.stanca@ccm.utcluj.ro

ABSTRACT

The accelerated evolution of technology, the pressures generated by climate change, and global socio-economic transformations have led to a profound reassessment of the way residential buildings are designed and used. This paper analyses the concept of "buildings of the future" from the perspective of residential housing, highlighting both the challenges and opportunities associated with their implementation. Issues related to digitalization, sustainability, innovative materials, social impact, and urban integration are addressed, with the aim of assessing whether these transformations represent real progress or an obstacle to contemporary society.

KEYWORDS: residential buildings, sustainability, smart homes, energy efficiency, urban development

1. Introduction

The rapid transformations of the global environment, the growth of the urban population, digitalization, and climate change are driving a profound reassessment of the way we design and use the built infrastructure. Buildings are no longer just static structures, but dynamic systems integrated into a complex digital and ecological ecosystem.

The concept of the building of the future involves intuitive architecture, capable of meeting the needs of users through smart technologies, sustainable materials, and adaptive design.

The construction sector plays a key role in economic and social development, while also being one of the largest consumers of natural resources.

According to the United Nations Environment Program (UNEP, 2022), buildings are responsible for about 37% of global carbon dioxide emissions. In this context, residential buildings of the future become a topic of major interest, both for specialists and for the public (Fig. 1) [1].

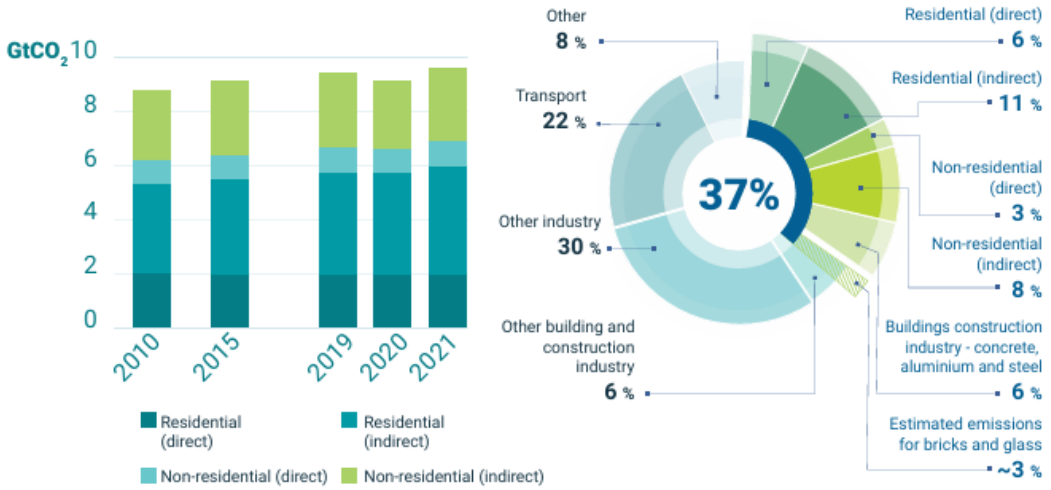

Fig. 1. *CO_2 emissions in buildings 2010-2021 (left) and share of buildings in global energy and process emissions in 2021 (right)* [1]

THE ANNALS OF "DUNAREA DE JOS" UNIVERSITY OF GALATI
FASCICLE IX. METALLURGY AND MATERIALS SCIENCE
Nº. 1 - 2026, ISSN 2668-4748; e-ISSN 2668-4756
Article DOI: https://doi.org/10.35219/mms.2026.1.05

The aim of the study is to analyse the current directions of development of residential housing and to assess the extent to which they constitute an opportunity or a challenge for society.

2. The need to transform residential buildings

The existing built stock is largely characterized by low energy efficiency and the use of outdated technologies that no longer meet current sustainability and performance requirements.

According to the European Commission (2020), more than 75% of buildings in Europe were built before the introduction of modern energy performance standards, and around 85% to 95% of them will still be in use in 2050 (Fig. 2) [2].

This situation highlights the need to intervene in the existing built stock to reduce energy consumption and environmental impact.

A determining factor in the transformation of residential buildings is the increase in energy consumption.

The buildings sector is responsible for around 40% of total energy consumption and around 36% of greenhouse gas emissions in the European Union (Fig. 3) [2, 3].

Fig. 2. *Solutions: less energy used, more green energy, less emissions* [2]

The lack of adequate thermal insulation, insufficient glazed areas, inefficient windows, and outdated heating systems contribute significantly to energy losses and increased operating costs for users [4].

Climate change is another major argument for transforming homes.

According to reports by the Intergovernmental Panel on Climate Change (IPCC, 2021), reducing carbon emissions from the buildings sector is essential to achieving the climate goals set by the Paris Agreement - Intergovernmental Panel on Climate Change. (2021) [5].

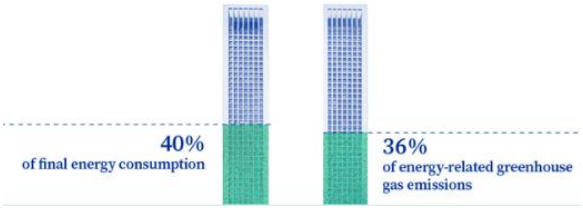

Fig. 3. *Buildings in the EU account for* [2]

Adapting residential buildings to new climatic conditions, by increasing energy performance and using renewable energy sources, contributes both to mitigating the effects of climate change and to increasing the resilience of the built environment [6].

Accelerated urbanization is also an important factor requiring the modernization of residential buildings.

According to Eurostat data (2022), more than 75% of the European Union's population lives in urban areas, and this proportion is constantly increasing [7].

The densification of cities and the pressure on existing infrastructure require sustainable solutions that optimize the use of resources and reduce the impact of urban development on the environment.

Studies by the World Health Organization (WHO, 2018) show that homes with low energy performance can have negative effects on health, favouring the development of respiratory problems and thermal discomfort [8].

Through thermal rehabilitation, modernization of installations, and increased structural safety, buildings can provide a healthier, safer, and more adapted living environment that meets current requirements.

The main factors that require the transformation of homes are (Fig. 4):

THE ANNALS OF "DUNAREA DE JOS" UNIVERSITY OF GALATI
FASCICLE IX. METALLURGY AND MATERIALS SCIENCE
Nº. 1 - 2026, ISSN 2668-4748; e-ISSN 2668-4756
Article DOI: https://doi.org/10.35219/mms.2026.1.05

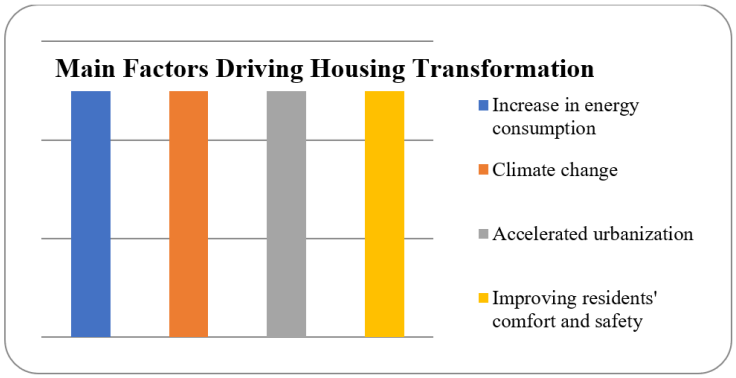

Fig. 4. *Main Factors Driving Housing Transformation*

The transformation of residential buildings is essential to improve the comfort and safety of beneficiaries.

3. Digitalization and the concept of smart housing

Digitalization is a broad process of transforming society by integrating digital technologies into all areas of daily life, both economic and social. In this context, the smart home appears as a direct result of technological progress, combining automation, connectivity, and artificial intelligence to improve the comfort, safety, and energy efficiency of the living space.

Digitalization is fundamentally changing the way people interact with the environment, and the home becomes an active space, capable of meeting the needs of users [9].

The concept of the smart home is based on the use of devices interconnected through the IoT, which allow the monitoring and control of different systems within the home, such as lighting, heating, security, or household appliances.

The IoT plays a critical role in the development of smart homes, as it enables continuous communication between devices and users, in real time. Thus, the dwelling is no longer a passive space, but an adaptive one, capable of anticipating the preferences of the tenants [10], (Fig. 5), [11].

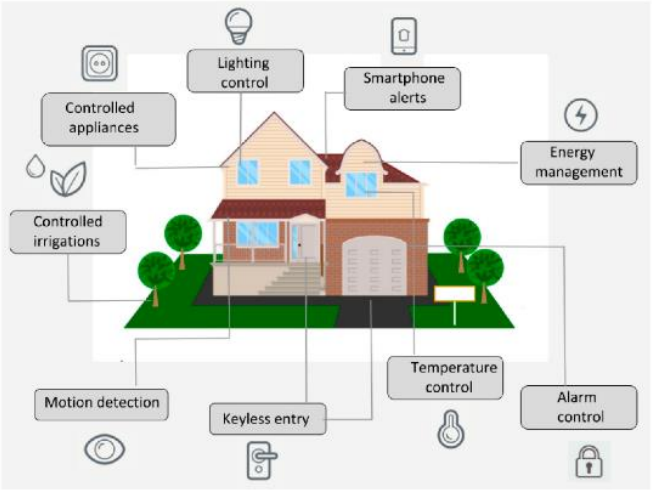

Fig. 5. *An IoT-based smart home depicting the use of smart sensing devices for different purposes* [11]

One of the main advantages of home digitalization is increased comfort. Through mobile apps or voice assistants, users can control home functions remotely, saving time and effort.

Automating household tasks helps reduce daily stress and improve quality of life. In addition, customized scenarios such as "night mode" or "departure mode" demonstrate how technology can simplify daily routine [12].

THE ANNALS OF "DUNAREA DE JOS" UNIVERSITY OF GALATI
FASCICLE IX. METALLURGY AND MATERIALS SCIENCE
Nº. 1 - 2026, ISSN 2668-4748; e-ISSN 2668-4756
Article DOI: https://doi.org/10.35219/mms.2026.1.05

In addition to comfort, the smart home makes a significant contribution to energy efficiency and environmental protection. Smart energy management systems can optimize electricity and gas consumption, reducing losses and costs.

According to the International Energy Agency (IEA, 2020), the digitalization of buildings can reduce energy consumption by up to 20%, which highlights the important role of technology in sustainable development [13]. Thus, smart housing becomes an essential tool in the fight against climate change.

The development of smart homes also poses certain challenges, in terms of data security and privacy [14].

Connected devices collect large amounts of information about users, which can create risks if this data is not properly protected.

Therefore, digitalization must be accompanied by appropriate policies and technical solutions to protect users.

4. Integration of residential buildings into the urban environment

The integration of residential buildings of the future into the urban environment is one of the fundamental directions of the sustainable development of contemporary cities.

Today, housing is no longer conceived as an isolated element, but as an integral part of a complex, energy-connected, functional, and social urban system. This principle underpins the smart city concept, which promotes resource efficiency, digitalization of infrastructure, and improved quality of urban life [15].

A first essential aspect of urban integration is the correlation of residential buildings with the city's energy infrastructure. The homes of the future are designed to be connected to smart grids, enabling a two-way exchange of energy.

Buildings equipped with photovoltaic panels and storage systems can function as prosumers, supplying surplus energy to the grid and helping to balance urban consumption [16].

This energy integration reduces dependence on conventional sources and increases the resilience of cities in the face of energy crises.

Another major element is the integration of buildings into sustainable urban mobility systems. Modern urban planning favours the location of housing in the vicinity of public transport, bicycle infrastructure, and pedestrian routes, with the aim of reducing the use of personal cars. Many residential complexes include charging stations for electric vehicles and spaces dedicated to alternative mobility, supporting the objectives of reducing carbon emissions at the urban level [17].

Integration into the urban environment also involves the relationship between residential buildings and green spaces.

According to recent studies, urban vegetation contributes significantly to reducing the heat island effect, improving air quality, and increasing the psychological comfort of the inhabitants [18].

Green roofs, green façades and communal gardens become central elements of modern residential design, integrating buildings into the urban ecosystem and enhancing local biodiversity [19], (Fig. 6), [20].

Fig. 6. *Studium Green – Seasons* [20]

The integration of residential buildings into the urban environment depends directly on public policies and urban planning regulations.

Strategies such as the European Union's Renovation Wave aim to modernize the existing built stock and integrate it into the vision of sustainable, energy-efficient, and inclusive cities [21].

The residential buildings of the future will be an active part of smart and green cities. Modern projects emphasize biophilic design such as: the inclusion of green spaces, abundant natural lighting, and the installation of effective ventilation for the health of residents.

In the future, urban plans should include mandatory energy efficiency and environmental criteria, and the smart city network will connect data on housing consumption with transport or energy infrastructure for global optimization.

Through coherent planning and strategic investments, residential buildings of the future can become active drivers of urban regeneration and sustainable development.

THE ANNALS OF "DUNAREA DE JOS" UNIVERSITY OF GALATI
FASCICLE IX. METALLURGY AND MATERIALS SCIENCE
Nº. 1 - 2026, ISSN 2668-4748; e-ISSN 2668-4756
Article DOI: https://doi.org/10.35219/mms.2026.1.05

5. Sustainable materials and sustainable construction

Innovation in the field of building materials is making a significant contribution to the development of the homes of the future.

Cross-laminated timber (CLT), self-healing concrete, and 3D printing technologies reduce costs and lead times, as well as reducing environmental impact.

Future residential buildings will use materials with a low environmental footprint. For example, there are new cements with 40–50% fewer carbon emissions than traditional cement [22].

Locally, advanced residential projects such as EvoHouse, the first certified passive dwelling in Romania, are built from cross-laminated timber (CLT), a renewable material that replaces concrete over large surfaces (Fig. 7), [23].

Fig. 7. *EvoHouse, the first certified passive home in Romania* [23]

Prefabricated modular construction uses eco-friendly panels and super-insulated windows to reduce waste and construction time.

The reuse of existing structures instead of massive demolition is encouraged to avoid the unnecessary generation of construction waste [24].

Resource savings are underpinned by the principles of the circular economy: the focus is on recyclable and reusable materials [25].

All of this is a first step toward creating buildings that can replenish their own resources, integrating solar panels on the roof and rainwater collection systems.

This type of approach reduces both environmental impact and long-term costs.

6. Socio-economic impact

Although buildings of the future offer significant benefits, they can accentuate social inequalities if access is limited by high costs.

Risks:
- increasing inequalities;
- social exclusion;
- urban gentrification.

Opportunities:
- reduction of maintenance costs;
- energy-efficient social housing;
- increased quality of life.

Public policies and support programs, such as the "Renovation Wave", are key to ensuring equitable access to energy-efficient housing.

The transition to the homes of the future also significantly influences socio-economic planning.

Initially, new Nearly Zero-Energy Building (NZEB) standards and smart technologies translate into higher construction costs due to advanced materials and complex installations [26]. Developers are feeling the pressure of these costs and the need for technical know-how.

However, the long-term economic benefits are obvious: energy-efficient buildings have much lower operating costs and command higher prices, making them more attractive to environmentally conscious buyers [27].

In Romania, the government and the EU offer generous subsidies to balance these costs: programs such as "Casa Verde Plus" grant incentives for the thermal efficiency of homes. Through this program, any citizen of the European Union residing in Romania can submit an application for financing in the form of an energy efficiency premium [28].

This makes renovation and sustainable construction more affordable from a financial point of view.

Socially, these changes create new jobs for designers, specialized builders, and IT technicians, but they can also generate inequalities if they are not well managed. There is a risk that only high-income families will immediately access new technologies, while others remain in traditional homes.

Buildings of the future will have a major socio-economic impact: they will stimulate the economy, improve the quality of life, and protect the environment, even if the transition brings some financial and technical challenges [29].

However, to maximize these benefits, strategic planning, coherent public policies, and technological education are essential.

7. Conclusions, Challenges or opportunities?

The analysis of residential buildings of the future highlights the fact that they cannot be

classified exclusively as challenges or opportunities; rather, they represent a complex reality at the intersection of technological innovation, ecological responsibility, and social transformation.

From the perspective of opportunities, homes of the future offer concrete solutions to reduce energy consumption and carbon emissions, contributing to the achievement of the climate goals established at the European and global level. The integration of renewable sources, the digitalization of consumption management, and the use of sustainable materials lead to increased energy efficiency and an improved quality of life for residents.

On the other hand, the process of transitioning to these housing models involves significant challenges. High upfront costs, the need to adapt the legislative framework, the shortage of specialists, and the risks associated with digitalization (such as data security) can slow large-scale deployment. At the social level, there is a risk of increasing inequality if access to energy-efficient and smart housing remains limited to certain socio-economic categories [30].

However, the balance tips, in the medium and long term, in favour of opportunities. Investments in sustainable buildings generate operational savings, increase property values, and stimulate the development of innovative industries. Moreover, in the context of the climate and energy crisis, the modernization of the residential stock is no longer an option, but a strategic necessity.

Therefore, buildings of the future should not be seen merely as a simple technological evolution, but as part of a structural transformation of the way society understands housing, environmental responsibility, and the relationship with urban space. To the extent that they are supported by coherent public policies, education, and fair investment, they predominantly represent major opportunities for the sustainable development of contemporary society.

In conclusion, if approached with proper planning and support, these homes of the future will serve as an opportunity to create resilient and comfortable communities rather than just a burden.

References

[1]. ***, https://globalabc.org/sites/default/files/202211/FULL%20REPORT_2022%20Buildings-GSR_1.pdf, accessed in 19.01.2026.
[2]. ***, https://www.consilium.europa.eu/en/infographics/fit-for-55-making-buildings-in-the-eu-greener/, accessed in 19.01.2026.
[3]. ***, https://energy.ec.europa.eu/topics/energy-efficiency/energy-performance-buildings/renovation-wave_en, accessed in 21.01.2026.
[4]. ***, https://www.iea.org, accessed in 21.01.2026.
[5]. ***, https://www.ipcc.ch, accessed in 21.01.2026.
[6]. Stanca Simona, *Improving energy efficiency in a building using passive energy-saving measures*, Journal of Applied Engineering Sciences (JAES), 13(26)2, DOI: 10.2478/jaes-2023-0034, 2023.
[7]. ***, https://ec.europa.eu/eurostat, accessed in 26.01.2026.
[8]. ***, https://www.who.int, accessed in 26.01.2026.
[9]. Negroponte N., *Being Digital. New York: Knopf*, Zeng, E., Mare, S., & Roesner, F., *End user security and privacy concerns with smart homes*, In Proceedings of the 13th Symposium on Usable Privacy and Security, SOUPS 2017, p. 65-80, Santa Clara, CA: USENIX Association.
[10]. Gubbi J., *et al.*, *Internet of Things (IoT): A vision, architectural elements, and future directions*, Future Generation Computer Systems, 29(7), p. 1645-1660, 2013.
[11]. Cristina Stolojescu-Crisan1, *et al.*, *An IoT-Based Smart Home Automation System*, Sensors, 21(11), 3784, 2021.
[12]. Harper R., *The Connected Home: The Future of Domestic Life*, London: Springer, 2011.
[13]. ***, https://www.iea.org/energy-system/decarbonisation-enablers/digitalisation, accessed in 3.02.2026.
[14]. Zeng E., *et al.*, *End user security and privacy concerns with smart homes*, In Proceedings of the 13th Symposium on Usable Privacy and Security, p. 65-80, Santa Clara, CA: USENIX Association, 2017.
[15]. ***, https://www.oecd.org/en/publications/cities-in-the-world_d0efcbda-en.html, accessed in 3.02.2026.
[16]. ***, https://www.unep.org/resources/annual-report-2022, accessed in 3.02.2026.
[17]. ***, https://www.mckinsey.com/featured-insights/world-economic-forum/overview, accessed in 3.02.2026.
[18]. ***, https://www.unep.org/resources/annual-report-2022, accessed in 4.02.2026.
[19]. ***, https://commission.europa.eu/strategy-and-policy/strategic-foresight/2020-strategic-foresight-report_en, accessed in 4.02.2026.
[20]. ***, https://www.studiumgreen.ro/seasons-ro/, accessed in 9.02.2026.
[21]. ***, https://european-union.europa.eu/index_en, accessed in 9.02.2026.
[22]. ***, https://hartareciclarii.ro/noutati/cladirile-viitorului-au-nevoie-de-tehnologii-inovatoare-pentru-a-face-fata-provocarilor/, accessed in 9.02.2026.
[23]. ***, https://www.planradar.com/ro/case-pasive-romania/, accessed in 9.02.2026.
[24]. Stanca Simona, *Reuse of construction waste*, INTER-ENG 2023, U.M.F.S.T. Târgu Mureș Romania, LNNS, vol. 926, p. 198-209, DOI: 10.1007/978-3-031-54664-8_19, 2023.
[25]. Stanca Simona, *The future of construction from a sustainable materials perspective*, The Annals of "Dunarea de Jos" University of Galati Fascicle IX Metallurgy and Materials Science, p. 37-42, DOI: 10.35219/mms.2024.1.05, 2024.
[26]. ***, https://www.romcim.ro/blog/constructiile-sustenabile-in-2026-de-la-tendinte-globale-la-provocari-locale-si-solutii-concrete.
[27]. ***, https://arhispec.ro/articol/romania-2030-cum-vor-arata-cladirile-viitorului, accessed in 16.02.2026.
[28]. ***, https://www.planradar.com/ro/case-pasive-romania/, accessed in 16.02.2026.
[29]. ***, https://www.romcim.ro/sustenabilitate/angajamentul-nostru, accessed in 16.02.2026.
[30]. ***, https://www.mckinsey.com/industries/engineering-construction-and-building-materials/how-we-help-clients, accessed in 17.02.2026.

THE ANNALS OF "DUNAREA DE JOS" UNIVERSITY OF GALATI
FASCICLE IX. METALLURGY AND MATERIALS SCIENCE
N°. 1 - 2026, ISSN 2668-4748; e-ISSN 2668-4756
Article DOI: https://doi.org/10.35219/mms.2026.1.06

STRUCTURE–MORPHOLOGY–DEFECT RELATIONSHIPS IN $CaTiO_3$-BASED PEROVSKITES FOR ENVIRONMENTAL APPLICATIONS

Adriana-Gabriela SCHIOPU[1,2], Florin CĂLIN-ISTRATE[3], Monica BÂLDEA[2], Daniela ISTRATE[1]

[1] Doctoral School Materials Science and Engineering, National University of Science and Technology POLITEHNICA Bucharest, Romania
[2] Pitești University Centre, Faculty of Mechanics and Technology, National University of Science and Technology POLITEHNICA Bucharest, Romania
[3] Uzina de Apă Budeasa, APA CANAL 2000 S.A. Pitești, Romania
e-mail: daniela.calin@stud.sefi.upb.ro, gabriela.schiopu@upb.ro, monica.baldea@upb.ro, florin_calin_istrate@yahoo.com

ABSTRACT

This review provides a comprehensive and critical analysis of the structure–morphology–defect relationships in $CaTiO_3$-based perovskites, with an emphasis on their environmental applications, particularly in water treatment and photocatalytic degradation processes. The paper systematically examines the influence of crystal structure, synthesis routes, microstructural evolution, and defect chemistry on the functional performance of $CaTiO_3$ materials. Special attention is given to the role of crystallographic phase stability, particle size distribution, surface area, porosity, and aggregation phenomena in controlling adsorption capacity and charge carrier dynamics. Different synthesis strategies—including solid-state reaction, sol–gel processing, hydrothermal and microwave-assisted routes, spray pyrolysis, and green mechanochemical methods—are comparatively evaluated with respect to their effects on morphology control and defect formation. Furthermore, the integration of $CaTiO_3$ with carbon-based materials and the development of doped or composite systems are analysed as strategies for enhancing photocatalytic activity and environmental stability.

By correlating structural features with the physicochemical performance indicators reported in the literature, this review identifies current limitations, unresolved challenges, and promising directions for future research. The analysis aims to provide a coherent framework for the rational design and optimization of $CaTiO_3$-based perovskites in environmental remediation technologies.

KEYWORDS: perovskite, $CaTiO_3$, SWOT analysis, environmental applications, ZnO reinforced composites

1. Introduction

Semiconductor oxides represent one of the most intensively investigated material classes for environmental remediation, particularly in photocatalytic water treatment. Among them, binary oxides with the general formula AO_2, such as TiO_2, have traditionally dominated the field due to their chemical stability, well-established synthesis routes, and relatively high photocatalytic efficiency under UV irradiation. However, despite these advantages, AO_2 systems exhibit intrinsic limitations, including restricted compositional flexibility, limited defect tunability, and challenges in band structure engineering without introducing significant recombination centres.

In contrast, ternary perovskite oxides with the general formula ABO_3 offer a structurally versatile alternative. The perovskite framework accommodates two distinct cationic sites (A and B), enabling independent control of lattice distortion, electronic configuration, and defect chemistry. This structural adaptability constitutes a major strength of ABO_3 systems, as it allows for the systematic tuning of

THE ANNALS OF "DUNAREA DE JOS" UNIVERSITY OF GALATI
FASCICLE IX. METALLURGY AND MATERIALS SCIENCE
Nº. 1 - 2026, ISSN 2668-4748; e-ISSN 2668-4756
Article DOI: https://doi.org/10.35219/mms.2026.1.06

electronic structure, oxygen vacancy concentration, and interfacial properties through aliovalent doping or compositional substitution. From a SWOT perspective (Figure 1), the principal strengths of ABO_3 materials compared to AO_2 oxides include enhanced chemical flexibility, greater tolerance to lattice distortion, and the ability to stabilize complex defect landscapes without structural collapse. These features are particularly advantageous for photocatalytic processes, where charge separation efficiency and surface reactivity depend critically on controlled defect engineering.

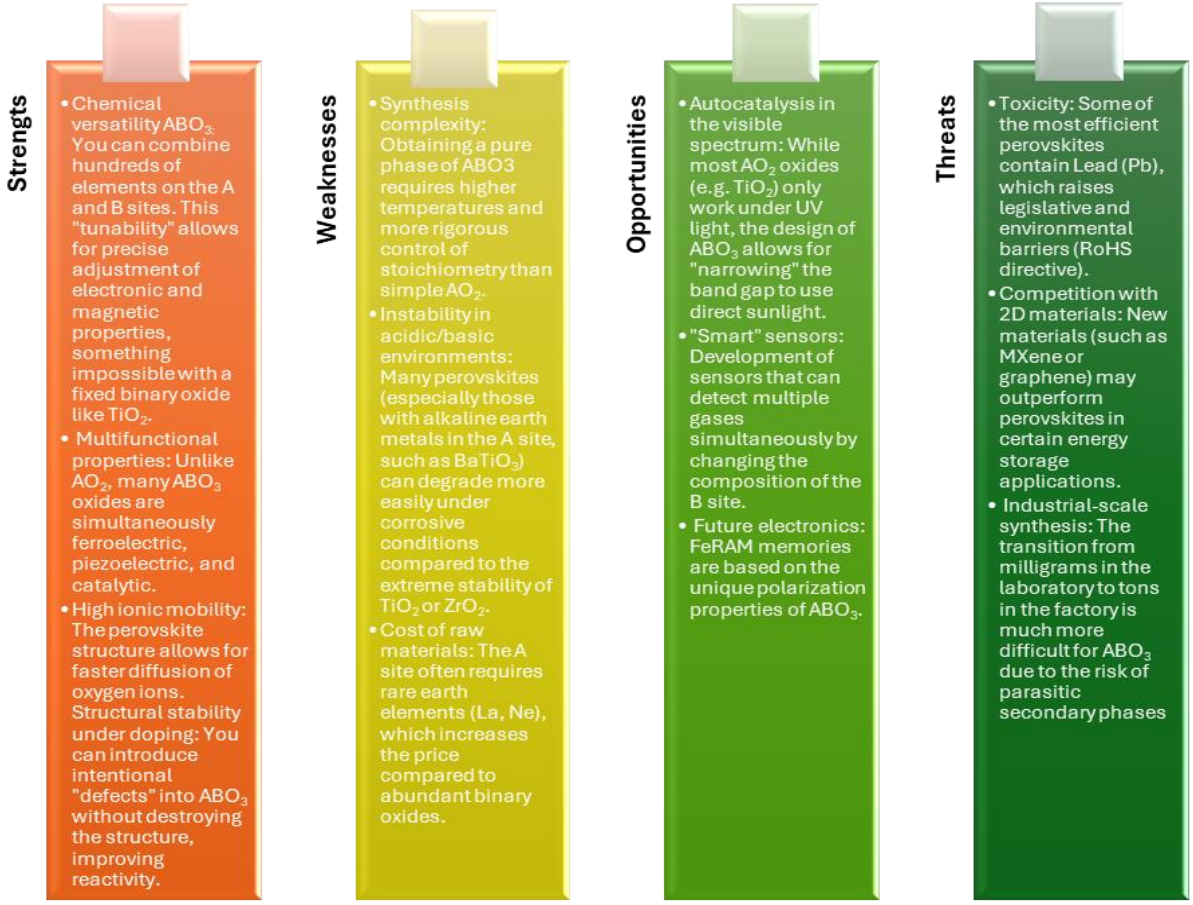

Fig. 1. *SWOT analysis of ABO_3 against AB*

Among oxide perovskites, calcium titanate ($CaTiO_3$) has attracted considerable attention owing to its chemical stability, non-toxicity, and structural robustness under environmental operating conditions [1, 4, 6]. At ambient temperature, $CaTiO_3$ crystallizes in an orthorhombic structure derived from the distorted cubic perovskite lattice, where TiO_6 octahedral tilting governs both band structure and defect accommodation. The electronic configuration of $CaTiO_3$ is characterized by a valence band primarily composed of O 2p states and a conduction band dominated by Ti 3d orbitals, resulting in a wide band gap typically reported in the range of 3.2–3.6 eV [3, 6]. Although this band gap restricts intrinsic activity to the ultraviolet region, the material remains highly attractive for environmental applications. In recent years, $CaTiO_3$-based materials have been extensively investigated for environmental remediation, particularly in photocatalytic water treatment and the degradation of organic pollutants [6, 11, 12, 20, 23]. The environmental relevance of $CaTiO_3$ stems from several key attributes: high chemical stability in aqueous media, resistance to photo corrosion, compatibility with green synthesis routes, and tuneable electronic properties through doping or composite formation. Various synthesis strategies—including solid-state reaction, sol–gel processing, hydrothermal and microwave-assisted methods, spray pyrolysis, and mechanochemical approaches—have been developed to tailor particle size, morphology, and defect concentration [1, 4, 7, 8, 13, 14]. These synthetic variations directly influence surface area, crystallinity, oxygen vacancy formation,

THE ANNALS OF "DUNAREA DE JOS" UNIVERSITY OF GALATI
FASCICLE IX. METALLURGY AND MATERIALS SCIENCE
N°. 1 - 2026, ISSN 2668-4748; e-ISSN 2668-4756
Article DOI: https://doi.org/10.35219/mms.2026.1.06

and charge carrier dynamics, all of which are critical parameters for photocatalytic efficiency.

The environmental performance of $CaTiO_3$-based systems is not determined solely by bulk crystal structure but rather by the interplay between structural distortion, morphological evolution, and defect chemistry. Morphological control through hydrothermal growth or microwave-assisted processing can yield nanocubes, nanorods, or hierarchical architectures that modify surface exposure and reactive facet distribution [14, 15]. Concurrently, intrinsic defects such as oxygen vacancies and extrinsic modifications introduced by rare-earth or transition-metal dopants can alter band structure, promote charge separation, and influence the generation of reactive oxygen species [17, 19-21]. Furthermore, integration with carbon-based materials such as graphene oxide enhances adsorption capacity and facilitates interfacial charge transfer, thereby improving photocatalytic degradation efficiency [12].

Despite the expanding body of literature on $CaTiO_3$-based photocatalysts, a unified framework correlating crystal structure, defect formation, morphological evolution, and environmental performance remain insufficiently consolidated. Many reported improvements are attributed either to increased surface area or to band gap modification, yet the interplay between crystallographic distortion, vacancy stabilization, and morphology-controlled surface reactivity is rarely addressed in an integrated manner. The objective of this review is, therefore, to provide a systematic and critical assessment of the structure–morphology–defect relationships in $CaTiO_3$-based perovskites with a specific focus on environmental remediation. By correlating crystallographic characteristics, synthesis routes, microstructural features, and defect engineering strategies with reported photocatalytic performance, this work aims to identify consistent trends, highlight methodological limitations, and propose future directions for the rational optimization of $CaTiO_3$ materials in water treatment technologies [1-27].

2. Crystallographic characteristics

The geometric stability of the structure is described by the Goldschmidt tolerance factor, which correlates the ionic radii of cations A and B with that of oxygen. For values close to unity, the cubic structure is stable; for significant deviations, structural distortions occur. If the tolerance factor is less than 1, the BO_6 octahedrons undergo rotations and inclinations, leading to orthorhombic or rhombohedral symmetries. If it is greater than 1, tetragonal distortions or structural instabilities may occur.

The stability of the structure is described by the Goldschmidt tolerance factor:

$$t = \frac{r_A + r_O}{\sqrt{2}(r_B + r_O)}$$

where r_A and represent the ionic radii of the A-site and B-site cations, respectively, and r_O is the ionic radius of oxygen. For an ideal cubic perovskite structure, $t \approx 1$, indicating optimal packing of the BO_6 octahedra within the lattice. Deviations from unity result in structural distortions driven by octahedral tilting and lattice strain. For values of $0.8 < t < 1$, the perovskite structure is generally stable, though deviations lead to orthorhombic or rhombohedral distortions.

In $CaTiO_3$, the Goldschmidt tolerance factor is approximately $t \approx 0.97$, indicating a slight geometric mismatch between the A-site Ca^{2+} cation and the TiO_6 octahedral framework. This deviation from the ideal cubic configuration induces cooperative rotations of the TiO_6 octahedra and stabilizes an orthorhombic structure (space group *Pbnm*) at room temperature, as seen in Fig. 2. The associated octahedral tilting, commonly described by the Glazer notation ($a^-a^-c^+$), modifies Ti–O–Ti bond angles and orbital overlap between O 2p and Ti 3d states, thereby influencing band structure, charge transport, and defect energetics.

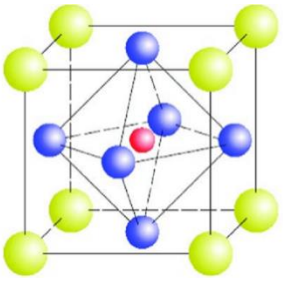

Fig. 2. *Perovskite structure*

A defining characteristic of the ABO_3 perovskite lattice is its chemical flexibility, which allows for partial or complete substitution at both the A and B sites without collapsing the crystal framework. This structural tolerance enables controlled doping and electronic tuning, facilitating the adjustment of optical, dielectric, and catalytic properties. In $CaTiO_3$, the orthorhombic lattice accommodates aliovalent dopants while maintaining structural coherence, making defect engineering and band structure modification viable strategies for performance optimization.

From an electronic perspective, the perovskite architecture promotes metal–oxygen–metal orbital overlap, and the B–O–B bond angle becomes a critical parameter governing conductivity and charge

THE ANNALS OF "DUNAREA DE JOS" UNIVERSITY OF GALATI
FASCICLE IX. METALLURGY AND MATERIALS SCIENCE
Nº. 1 - 2026, ISSN 2668-4748; e-ISSN 2668-4756
Article DOI: https://doi.org/10.35219/mms.2026.1.06

mobility. Octahedral distortions alter bandwidth and carrier dynamics, while also influencing the formation of energy and distribution of intrinsic defects such as oxygen vacancies. In $CaTiO_3$, the structural distortion associated with $t < 1$ introduces lattice strain that lowers the energetic barrier for vacancy formation in specific crystallographic environments. These vacancies, in turn, affect crystal growth kinetics during synthesis by modifying surface energy anisotropy and diffusion pathways, ultimately shaping particle morphology and aggregation behavior.

Consequently, morphology cannot be regarded solely as a processing outcome but rather as a manifestation of the underlying structural–defect equilibrium. Nanocubic architectures, hierarchical assemblies, or mesoporous aggregates reflect the interplay between lattice distortion, defect stabilization, and growth dynamics. The resulting surface configuration governs adsorption capacity, active site density, and interfacial charge transfer efficiency. Environmental performance, particularly photocatalytic degradation efficiency, therefore, arises from a coupled mechanism in which crystallographic distortion dictates defect stabilization, defects influence morphological evolution, and morphology controls surface reactivity and charge carrier separation.

$CaTiO_3$ thus represents a structurally adaptable perovskite system in which crystallographic symmetry, defect chemistry, and morphology are intrinsically interconnected. Its orthorhombic lattice undergoes temperature-driven transitions (Pbnm → tetragonal → cubic), further affecting dielectric behavior and defect stability. Various synthesis approaches—including solid-state, sol–gel, coprecipitation, hydrothermal, combustion, spray pyrolysis, and microwave-assisted routes—enable the modulation of phase purity, grain size, and defect concentration. Sol–gel processing offers molecular-level stoichiometric control and stabilization of the orthorhombic phase above 700–800 °C, while microwave-assisted treatments reduce processing time and enhance chemical homogeneity. Hydrothermal methods provide advanced morphological control, and coprecipitation yields monocrystalline nanoparticles with controlled dimensions.

Taken together, the perovskite framework of $CaTiO_3$ provides a robust and versatile platform in which structural parameters, defect formation, and morphological evolution are tightly coupled. This integrated structural–defect–morphology relationship constitutes the basis for the rational optimization of $CaTiO_3$-based materials in environmental remediation and related functional applications.

3. Morphology and specific surface area

Morphology and specific surface area are essential structural parameters in the control of the functional properties of $CaTiO_3$, directly influencing adsorption processes, surface reactivity, photocatalytic behavior, optical properties, and interaction with polymer or biological matrices. The integrated analysis of the studies [1-27] highlights that morphology is predominantly determined by the synthesis method, the ratio of precursors, the heat treatment temperature, and possible dopants.

Aerosol processing (spray-pyrolysis) tends to impose a spherical morphology, related to the formation of particles from atomized droplets. In the spray-pyrolysis study, monophasic $CaTiO_3$ powders with spherical particles and sizes in the nano-submicron range are obtained. In addition, it is explicitly emphasized that the concentration of the precursor solution controls the surface texture (smooth at low concentrations vs. rougher/heterogeneous appearance and stronger agglomeration at high concentrations), as well as the dimensional distribution (e.g., particles around ~0.4 μm at low concentrations, respectively often 0.6–0.8 μm at higher concentrations). From a mechanistic perspective, the explanation proposed in the article (rapid evaporation, internal stresses, formation of saline "crust") is consistent with the physics of droplet drying and the transition from dense/smooth particles to particles with a rough surface or even shell-like defects [4].

In the family of sol-gel "soft chemistry" routes, the primary particle sizes can descend to the fine nanometre regime, but agglomeration remains a recurrent phenomenon [1, 2, 7]. For $CaTiO_3$ sol–gel powders, primary particles with sizes of approximately ~13 nm size and agglomerations on the order of ~30 nm, observed by TEM, are reported, suggesting that drying and densification of the gel lead to particle association, even when nucleation produces nanometric units [7]. In the same logic of obtaining "green"/mechanochemical materials (intense grinding followed by calcination), nanocrystalline $CaTiO_3$ is obtained, with a crystallite size of approximately ~23.5 nm; here, mechanical activation accelerates the solid-solid reaction and lowers the temperature/energy necessary for phase formation, but does not necessarily imply fine morphological control at the level of individual particles. Hydrothermal syntheses (including microwave-assisted variants) most strongly promote anisotropy and particle "architectures", by controlling local supersaturation, ionic transport, and selectivity of crystallographic faces. A relevant example is hydrothermal synthesis at 180 °C for 16 h, where the change in the titanium precursor from solid (TiO_2) to

liquid (titanium isopropoxide) radically alters the $CaTiO_3$ morphology: from cubic morphology to a hollow rectangular morphology, suggesting a different nucleation/growth dynamic and possibly a dissolution–reprecipitation/Kirkendall mechanism under certain conditions [9]. Similarly, microwave-assisted hydrothermal synthesis at 140 °C for 16 min leads to the formation of microcubes (~3.0 μm) in the $CaTiO_3$:Sm system, and the variation of Sm^{3+} doping (within the investigated range) does not significantly change the morphology, indicating that the kinetic regime imposed by microwave irradiation dominates the shape selection (microcubes) more than the subtle effects of doping at low concentrations [14].

At the level of nanoparticles obtained by moderate heat treatments and analysed in detail, a structural hierarchy is often observed: nanometric crystallites, submicron aggregates, and agglomerates. In a study of the $CaTiO_3$ (perovskite) system, average crystallite sizes on the order of ~80 nm (determined by Rietveld refinement) [11] and secondary agglomerations around ~500 nm are reported, evidenced by SEM morphological analysis, confirming that the actual morphology observed in SEM can be governed by the aggregation of primary particles. This is critical for surface-dependent properties (adsorption/photocatalysis) and for sintering, because the specific surface area and effective porosity are controlled not only by the size of the crystallite, but also by the agglomeration mode.

In environmental remediation-oriented work with $CaTiO_3$–carbon composites (e.g. $CaTiO_3$/GO), the morphological rationale is explicitly connected to the specific surface area and the role of the surface in adsorption: it is emphasized that integration with graphene-based materials aims to increase the adsorption of pollutants through a large specific surface area and to facilitate charge transfer (limiting e^-/h^+ recombination). Even though this statement is functional, it anchors morphology (and, implicitly, texture/area) as a critical parameter in the design of $CaTiO_3$ materials for surface processes [12].

In the field of rare earth-doped and rapidly sintered $CaTiO_3$-based phosphors, anisotropic rod-type morphologies are distinguished. For $CaTiO_3:Eu^{3+}$ (combining coprecipitation and sintering), SEM highlights rod-shaped particles. In addition, microwave-assisted sintering produces slightly larger particles with more surface defects than conventional sintering, a difference attributed to the fast-heating regime and short treatment time [18].

Doping and associated phase transformations can change morphology at the level of ceramic particles, sometimes more dramatically than changing the synthesis pathway. For La-doped $CaTiO_3$ ceramics, SEM analysis indicates a morphological evolution directly correlated with the composition and the set of phases: for poorly doped samples, asymmetrical "feather-like/columnar" structures appear (tens to hundreds of nm), while at concentrations of 0.05–0.10 mol %A, small, spherical granules of about 10–20 nm are reported; at concentrations where the $La_{0.3}Ca_{0.7}TiO_3$ phase is formed and becomes dominant, the morphology evolves towards lamellar particles, "diamond-shaped", organized in dendritic structures [20]. In this case, morphology functions as a direct indicator of phase transformations and changes in crystalline growth mechanisms, probably associated with differences in cation diffusion and surface energy between coexisting phases, relevant to both photocatalytic performance and mechanical behavior through densification and particle connectivity.

For $CaTiO_3$ obtained by classical chemistry (coprecipitation), predominantly spherical, crystalline particles with diameters of the order of hundreds of nanometres and with a pronounced tendency to agglomeration are reported. In the coprecipitation-based study, SEM/TEM micrographs indicate agglomerates consisting of spherical particles with an average size of ~200 nm, and confirmation by HRTEM/SAED supports the crystalline character and the formation of the perovskite (orthorhombic) phase [17]. This type of morphology is typical of systems where nucleation is abundant, but growth control is limited by coalescence and capillary forces at drying/calcination, resulting in larger secondary particles than primary crystallites.

In the study on synthesis by the mechanochemical method [25], SEM micrographs highlight particles with predominantly irregular morphology, some crystals presenting pseudo-hexagonal appearance, with dimensions below 90 nm. BET analysis indicates a type IV isotherm with H1 hysteresis, corresponding to mesoporous materials, and the reported specific surface area is 301.1 m^2/g. This value is unusually high for a perovskite oxide obtained by treatment at 1000 °C, suggesting the existence of a highly fragmented and porous aggregate structure. The increase in crystallite size from 17.7 nm (1:1 ratio) to 40.27 nm (1:7 ratio) is highlighted, which confirms the role of the TiO_2 precursor in the nucleation and coalescence of the particles. In PEO/$CaTiO_3$ systems [27], XRD analysis shows a decrease in the intensity of the crystalline peaks of the PEO phase after the introduction of nanoparticles, indicating an increase in the amorphous fraction. Although $CaTiO_3$ is not morphologically analysed by SEM in this study, its effect on the polymer matrix microstructure demonstrates relatively homogeneous dispersion and efficient interfacial interaction.

THE ANNALS OF "DUNAREA DE JOS" UNIVERSITY OF GALATI
FASCICLE IX. METALLURGY AND MATERIALS SCIENCE
Nº. 1 - 2026, ISSN 2668-4748; e-ISSN 2668-4756
Article DOI: https://doi.org/10.35219/mms.2026.1.06

4. Photocatalysis and surface engineering

Heterogeneous photocatalysis based on semiconductor oxides is one of the most studied solutions for the degradation of organic pollutants and for advanced oxidation processes in water treatment. In this context, $CaTiO_3$, a perovskite material of the ABO_3 type, has established itself as a promising alternative to TiO_2 due to its high chemical stability, non-toxic character, and structural flexibility through doping and composite formation.

Although the $CaTiO_3$ bandgap (~3.4–3.6 eV) limits activity predominantly to the UV domain, recent literature demonstrates that, through defect engineering and integration into heterostructures, the activity can be extended to the visible domain. Studies dedicated to the synthesis of $CaTiO_3$ at low temperatures for the degradation of methylene blue confirm the photocatalytic potential of this material in the treatment of contaminated water [6].

Visible expansion strategies include boron doping (B–$CaTiO_3$) or integration with graphene oxide (GO). The B–$CaTiO_3$/GO composite exhibits improved methylene blue degradation under visible light with an optimal loading of 5 wt.% GO. The mechanism involves efficient separation of e^-/h^+ pairs and the generation of radicals $\cdot OH$ and $O_2^{\cdot -}$ [12].

Studies on $CaTiO_3$ synthesized at low temperatures for dye degradation [6] indicate the potential of the material in wastewater treatment, especially in combination with doping or carbon supports.

The valence band of $CaTiO_3$ is dominated by O 2p orbitals, and the conduction band by Ti 3d orbitals. The absorption of photons with energy ≥ Eg leads to the generation of electron–hole pairs:

$$CaTiO_3 + h\nu \rightarrow e_{CB}^- + h_{VB}^+$$

Electrons reduce dissolved oxygen to superoxide radicals, and holes oxidize water or hydroxyl groups, generating hydroxyl radicals, responsible for mineralizing organic pollutants [6], Electrons reduce dissolved oxygen:

$$O_2 + e^- \rightarrow O_2^{\bullet -}$$

Holes oxidize water or hydroxyl groups:

$$H_2O + h^+ \rightarrow \bullet OH + H^+$$

The radicals generated are responsible for the mineralization of organic pollutants.

Oxygen vacancies introduce intermediate levels in the band gap and favour the separation of charge carriers. Studies on $CaTiO_3$ synthesized by controlled chemical routes show that heat treatments influence the concentration of defects and, implicitly, the photocatalytic efficiency [1, 7].

Also, low-temperature synthesis for photocatalytic applications [6] confirms that reducing the crystallite size and increasing the number of structural defects lead to improved dye degradation efficiency.

In the study on the green chemistry synthesis of $CaTiO_3$ [23] the nanocrystalline material demonstrated a degradation of up to 93% of methylene blue under sunlight, with a high specific surface area (≈301 m^2/g), favourable to adsorption and surface reactions, being reported. The results indicate a direct correlation between the active surface area and the photodegradation efficiency.

Anionic or cationic doping alters the band structure. The controlled synthesis of $CaTiO_3$ by sol-gel or hydrothermal methods allows the uniform distribution of dopants [2, 11].

B–$CaTiO_3$/GO composites exhibit superior efficiency in dye degradation under visible light due to: GO's electronic conductivity, rapid electron transfer, and reduced e^-/h^+ recombination.

The study on graphene oxide perovskite composites highlights the significant increase in methylene blue degradation compared to pure $CaTiO_3$ [12].

Doping with lanthanide ions (Sm^{3+}, Pr^{3+}, Eu^{3+}, Er^{3+}) is a major vector of functionalization:

- $CaTiO_3:Sm^{3+}$ exhibits intense orange emissions due to $^4G_{5/2} \rightarrow {}^6H_j$ transitions, making it suitable for FED and LED applications [14].
- $CaTiO_3:Pr^{3+}$ demonstrates persistent luminescence properties (afterglow), where oxygen vacancies and local excess Ca act as trap levels [17].
- $CaTiO_3:Eu^{3+}$ exhibits dominant red emission at 617 nm ($^5D_0 \rightarrow {}^7F_2$), optimizable by microwave-assisted sintering [18].
- $CaTiO_3:Er^{3+}$ produces up-conversion emission under excitation 980 nm, with green and red emissions; hydrothermal films exhibit excellent hydrophilicity and demonstrated biocompatibility on BHK cells [19]. The control of the dopant concentration influences the luminescent intensity and quenching phenomena, with an optimal concentration below 3% molar for Er^{3+} being reported.

5. Influence of the synthesis method on performance in water treatment

The sol-gel and coprecipitation methods [1, 2, 7, 11, 13] allow the production of nanoparticles with increased specific surface area, which favours the adsorption of organic molecules and the accessibility

THE ANNALS OF "DUNAREA DE JOS" UNIVERSITY OF GALATI
FASCICLE IX. METALLURGY AND MATERIALS SCIENCE
Nº. 1 - 2026, ISSN 2668-4748; e-ISSN 2668-4756
Article DOI: https://doi.org/10.35219/mms.2026.1.06

of the active centres. In nanoparticles obtained by microwave-assisted sol-gel [13] the reduction of processing time and dimensional control contribute to the increase of photocatalytic efficiency.

The spray-pyrolysis method [4] produces submicron spherical particles, and the control of the concentration of precursors influences the surface texture and, implicitly, the kinetics of the degradation reactions. Mechanochemical synthesis [23] highlights the possibility of obtaining an eco-friendly material with high photocatalytic activity and no residual toxic effects on the environment (confirmed by phytotoxicity and antimicrobial activity tests).

The integration of $CaTiO_3$ with graphene oxide [12] is an effective strategy for increasing performance in water treatment. The B–$CaTiO_3$/GO composite exhibits: an increase in specific surface area, improved pollutant adsorption, reduced electron–hole recombination, and efficient charge transfer at the semiconductor–carbon interface.

These effects lead to faster and more efficient degradation of dyes compared to pure $CaTiO_3$.

Doping with lanthanides or transition metals alters the electronic structure and creates intermediate levels in the band gap, facilitating the expansion of absorption into the visible domain. In La-doped $CaTiO_3$ ceramics [20], improved photocatalytic activity correlated with structural and morphological changes in the material is reported.

In the case of $CaTiO_3$ doped with Sm or Eu [14, 18], although the primary objective is optoelectronic, defectological changes can indirectly contribute to photocatalytic activity by increasing trap centres for carriers.

Vanadium doping [21] leads to morphological changes (cuboidal structures) and influences charge transfer, which is relevant for advanced oxidation processes. In the article on $CaTiO_3$ asymmetric membranes [24], the use of the controlled porous structure for separation processes and potential for integrated catalytic systems in water treatment are explored. The control of porosity and microstructure allows the flow and access of reactants to the active surface to be optimized. A major advantage highlighted in the analysed literature is the non-toxic character of $CaTiO_3$. In the mechanochemical study [25], the degradation products of methylene blue showed no significant phytotoxic effects on seed germination, and antimicrobial tests indicated the absence of residual toxicity. This characteristic differentiates $CaTiO_3$ from other semiconductor oxides that can generate problematic byproducts.

6. Critical analysis of structure–morphology–defect relationships in $CaTiO_3$-based perovskites for environmental applications

The existing literature on $CaTiO_3$-based perovskites for environmental remediation demonstrates substantial progress in synthesis optimization, structural tailoring, and defect engineering [1-3]. Nevertheless, a closer examination of the published results reveals conceptual inconsistencies and methodological limitations that necessitate a critical reassessment. Although numerous investigations report enhanced photocatalytic performance through morphological refinement and dopant incorporation [6, 11, 20, 21], the correlations proposed between structural parameters and environmental efficiency are often qualitative rather than quantitatively validated.

A frequently invoked argument in the literature concerns the direct proportionality between specific surface area and photocatalytic efficiency. Nanometric $CaTiO_3$ powders synthesized via sol–gel, mechanochemical, microwave-assisted, or green routes typically exhibit improved degradation of model pollutants such as methylene blue [6, 8, 11, 25]. The enhancement is generally attributed to increased adsorption capacity and a higher density of reactive surface sites. However, comparative analyses indicate that surface area alone cannot fully explain catalytic performance. Materials obtained by spray pyrolysis [4] or combustion routes [5], despite moderate surface areas, may exhibit competitive stability and activity, while hydrothermal products with controlled morphology [14, 15] often demonstrate superior performance even without exceptionally high BET values. These discrepancies suggest that surface area must be interpreted in conjunction with crystallinity, defect concentration, and charge carrier dynamics.

The role of intrinsic defects, particularly oxygen vacancies, is widely emphasized in studies dealing with $CaTiO_3$ photocatalysts [6, 11, 20, 21]. Oxygen vacancies are commonly described as shallow donor states capable of facilitating charge separation and extending light absorption. Nevertheless, direct quantification of defect density remains limited across the literature. In many cases, defect presence is inferred indirectly from band gap shifts or XRD peak variations [3, 18], without systematic confirmation via spectroscopic techniques. Excessive vacancy concentration may increase recombination centres and compromise structural stability, yet such trade-offs are seldom discussed in depth. Therefore, defect–performance relationships often remain suggestive rather than demonstratively causal.

THE ANNALS OF "DUNAREA DE JOS" UNIVERSITY OF GALATI
FASCICLE IX. METALLURGY AND MATERIALS SCIENCE
Nº. 1 - 2026, ISSN 2668-4748; e-ISSN 2668-4756
Article DOI: https://doi.org/10.35219/mms.2026.1.06

Doping strategies involving rare-earth or transition-metal ions have been extensively explored as a means of electronic structure engineering [14, 17, 19, 20, 21]. For instance, lanthanum-doped $CaTiO_3$ ceramics exhibit morphological transformations correlated with enhanced photocatalytic response [20], while vanadium incorporation modifies charge transfer behavior and cuboid morphology [21]. Similarly, Sm^{3+} and Pr^{3+} substitutions influence microstructure and luminescent properties [14, 17], indirectly affecting charge carrier recombination pathways. However, the mechanistic interpretation of dopant effects frequently relies on band gap narrowing arguments without detailed verification of band edge positions relative to redox potentials. Moreover, the potential formation of secondary phases is not consistently evaluated [20], and the distinction between structural effects and genuine electronic modifications remains insufficiently clarified.

The synthesis route further complicates the structure–property relationship. Solid-state and conventional ceramic processing methods yield highly crystalline materials but often with limited surface area [1, 2]. In contrast, sol–gel and microwave-assisted techniques enable finer control over particle size and homogeneity [7, 13, 16], while hydrothermal processing promotes anisotropic growth, including nanocubes and hierarchical architectures [14, 15]. Green mechanochemical approaches emphasize sustainability and environmental compatibility [8, 25], aligning well with remediation applications. However, despite the diversity of synthetic methodologies, few studies evaluate scalability or long-term operational stability, particularly under realistic wastewater conditions. Membrane-based $CaTiO_3$ systems [24] and polymer-based nanocomposites [10, 27] illustrate alternative integration strategies, yet comprehensive assessments of durability and recyclability remain limited.

Another critical aspect concerns the experimental evaluation protocols used to assess environmental performance. Most investigations rely on model dye degradation under controlled laboratory illumination [6, 11, 12, 25]. Although such tests provide valuable comparative insight, they do not necessarily represent complex industrial effluents containing mixed organic and inorganic contaminants. Mineralization efficiency, toxicity of degradation intermediates, and catalyst leaching are rarely examined in detail. Composites incorporating graphene oxide [12] demonstrate improved charge separation and adsorption capacity, reinforcing the importance of interfacial engineering; however, systematic long-term cycling studies are often restricted to a few repetitions. The absence of standardized testing conditions—light intensity, catalyst dosage, pH, and pollutant concentration—further complicates direct comparison among studies [6, 11, 20].

From a theoretical standpoint, computational investigations into the structural and electronic properties of $CaTiO_3$ polymorphs provide valuable insight into band structure modifications and defect energetics [3]. Nonetheless, the integration between density functional theory predictions and experimental photocatalytic data remains sporadic. Few works attempt to correlate calculated defect formation energies with measured activity trends. A predictive framework linking crystal symmetry, morphology, defect density, and environmental degradation kinetics is largely absent, despite the growing number of experimental reports [1-27].

Collectively, the literature confirms the promising potential of $CaTiO_3$-based perovskites for environmental applications, including water treatment and photocatalytic degradation [6, 11, 12, 20, 25]. However, the field is still characterized by descriptive correlations rather than mechanistically validated models. Future research must adopt a more rigorous and standardized methodology that integrates defect quantification, band alignment analysis, morphology control, and real-environment performance evaluation. Only through such systematic integration of structural, morphological, and electronic parameters can $CaTiO_3$-based perovskites evolve from laboratory-scale demonstrations to scalable and reliable environmental remediation technologies [1-27].

7. Conclusions and future perspectives

This review has critically examined the structure–morphology–defect relationships in $CaTiO_3$-based perovskites with an emphasis on their environmental applications, particularly photocatalytic water treatment. The analysis of recent literature demonstrates that the environmental performance of $CaTiO_3$ cannot be attributed to a single structural parameter but rather emerges from the complex interplay between crystallographic distortion, microstructural evolution, defect chemistry, and surface engineering. Structural characteristics such as octahedral tilting and orthorhombic symmetry influence the band structure and defect accommodation, while synthesis-controlled morphology governs surface accessibility, porosity, and aggregation behavior. Intrinsic defects, especially oxygen vacancies, play a dual role by promoting charge separation at moderate concentrations while potentially acting as recombination centres when excessive. Extrinsic doping and composite formation further modify the electronic structure and interfacial charge transfer, yet

their effects remain highly dependent on dopant solubility, phase stability, and defect distribution.

Although $CaTiO_3$-based materials show promising photocatalytic degradation efficiency under laboratory conditions, particularly for model organic dyes, the field remains largely empirical. Reported performance improvements are often interpreted through qualitative correlations rather than mechanistically validated models. The absence of standardized testing protocols limits long-term stability studies, and scarce evaluation under realistic wastewater matrices restricts the translation of laboratory findings into practical environmental technologies. Furthermore, quantitative characterization of defect densities and band edge alignment remains insufficient, and the integration of computational predictions with experimental validation is still sporadic.

Future research should therefore move toward a more rigorous and predictive framework. Systematic defect quantification using advanced spectroscopic techniques, combined with density functional theory calculations of defect formation energies and band alignment, would clarify the true contribution of intrinsic and extrinsic modifications. Morphology control must be addressed not only from a surface-area perspective but also in terms of facet-dependent reactivity and charge transport pathways. In addition, scalable synthesis routes that maintain structural and defect integrity should be prioritized to bridge the gap between laboratory-scale preparation and industrial applicability.

Equally important is the evaluation of environmental performance under realistic operating conditions. Studies should extend beyond model dye degradation to include mineralization efficiency, toxicity of degradation intermediates, catalyst recyclability, and structural stability over extended cycling. The development of standardized photocatalytic testing methodologies would enable meaningful comparison across studies and facilitate the identification of truly optimized compositions.

In conclusion, $CaTiO_3$-based perovskites represent a structurally versatile and environmentally stable class of materials with significant potential for sustainable water treatment technologies. However, advancing from descriptive structure–property correlations toward quantitatively validated design principles is essential. A comprehensive integration of structural analysis, defect engineering, morphology control, and realistic environmental evaluation will be decisive for the rational optimization and practical implementation of $CaTiO_3$-based systems in environmental remediation.

References

[1]. Aung S., *et al.*, *Synthesis and Characterization of Calcium Titanate ($CaTiO_3$) Powder for Photovoltaic Application*, J. Myanmar Acad. Arts Sci., vol. 2, 2020.
[2]. Dornellas Athayde D., *Synthesis and Characterization of Perovskite Materials for Production of Mixed Ionic and Electronic Conduction Membranes*, Ph.D. Thesis, Graduate Program in Chemical Engineering, 2016.
[3]. Loletti M., *et al.*, *Structural and Electronic Properties of $CaTiO_3$ Polymorphs and 2D-Derived Systems: A Theoretical Investigation*, Eur. Phys. J. B, vol. 98, no. 4, DOI: 10.1140/epjb/s10051-025-XXXX-X, 2025.
[4]. Lanfredi S., *et al.*, *Synthesis and Structural Characterization of Calcium Titanate by Spray Pyrolysis Method*, Mater. Lett., vol. 201, p. 148-151, DOI: 10.1016/j.matlet.2017.05.049, 2017.
[5]. Lee S., *et al.*, *Synthesis of Lead-Free $CaTiO_3$ Oxide Perovskite Film through Solution Combustion Method and Its Thickness-Dependent Hysteresis Behaviors within 100 mV Operation*, Molecules, vol. 26, no. 18, DOI: 10.3390/molecules26185647, 2021.
[6]. García-Mendoza M. F., *et al.*, *$CaTiO_3$ Perovskite Synthesized by Chemical Route at Low Temperatures for Application as a Photocatalyst for the Degradation of Methylene Blue*, J. Mater. Sci.: Mater. Electron., vol. 34, no. 10, DOI: 10.1007/s10854-023-10152-3, 2023.
[7]. Mallik P. K., *et al.*, *Characterisation of Sol–Gel Synthesis of Phase Pure $CaTiO_3$ Nano Powders after Drying*, IOP Conf. Ser.: Mater. Sci. Eng., DOI: 10.1088/1757-899X/75/1/012012, 2015.
[8]. Kaur P., *et al.*, *Green Synthesis of Nano-Sized Calcium Titanate $CaTiO_3$ Using Solid State Mechano-Chemical Solventless Method and Its Characterization*, Int. J. Res. Eng. Appl. Manag., vol. 4, no. 1, 2018.
[9]. Pandey P. K., *et al.*, *Facile and Eco-Friendly One Step Low Temperature Synthesis of Very Large Scale $ATiO_3$ (A = Ca, Sr, Ba and Cd)*, J. Appl. Mater. Sci. Eng. Res., vol. 10, no. 1, 2026.
[10]. Naser R., *et al.*, *Fabrication of PGS/$CaTiO_3$ Nano-Composite for Biomedical Application*, Int. J. Nanoscience Nanotechnol., vol. 12, 2016.
[11]. Cerón-Urbano L., *et al.*, *Nanoparticles of the Perovskite-Structure $CaTiO_3$ System: The Synthesis, Characterization, and Evaluation of Its Photocatalytic Capacity to Degrade Emerging Pollutants*, Nanomaterials, vol. 13, no. 22, DOI: 10.3390/nano13222321, 2023.
[12]. Altin I., *Perovskite Type B-$CaTiO_3$ Coupled with Graphene Oxide as Efficient Bifunctional Composites for Environmental Remediation*, Processes, vol. 11, no. 11, DOI: 10.3390/pr11113358, 2023.
[13]. Kostryukov V. F., Igonina A. E., *Microwave Synthesis of $CaTiO_3$ Nanoparticles by the Sol–Gel Method*, Kondensirovannye Sredy Mezhfaznye Granitsy, vol. 22, no. 4, p. 504-506, 2020.
[14]. Pinatti I. M., *et al.*, *$CaTiO_3$ and $Ca_{1-3x}Sm_xTiO_3$: Photoluminescence and Morphology as a Result of Hydrothermal Microwave Methodology*, Ceram. Int., vol. 42, no. 1, p. 1352-1360, DOI: 10.1016/j.ceramint.2015.09.086, 2016.
[15]. Mimura K., *et al.*, *One-Step Synthesis of $BaTiO_3$/$CaTiO_3$ Core–Shell Nanocubes by Hydrothermal Reaction*, J. Asian Ceram. Soc., vol. 9, no. 1, p. 336-342, DOI: 10.1080/21870764.2021.1902713, 2021.
[16]. Anjelin S., *et al.*, *Preparation and Characterization of $CaTiO_3$ Nanopowder by Using Sol–Gel Method*, Int. J. Adv. Sci. Res. Manag., vol. 3, 2018.
[17]. Meroni D., *et al.*, *Sol–Gel Synthesis of $CaTiO_3$:Pr^{3+} Red Phosphors: Tailoring the Synthetic Parameters for Luminescent and Afterglow Applications*, ACS Omega, vol. 2, no. 8, p. 4972-4981, DOI: 10.1021/acsomega.7b00818, 2017.
[18]. Parajuli D., *et al.*, *Structural, Morphological, and Textural Properties of Coprecipitated $CaTiO_3$ for Anion Exchange in the Electrolyzer*, J. Nepal Phys. Soc., vol. 9, no. 1, p. 137-142, DOI: 10.3126/jnphyssoc.v9i1.60468, 2023.

[19]. Wang H., *et al.*, *Synthesis and Characterization of the $CaTiO_3:Eu^{3+}$ Red Phosphor by an Optimized Microwave-Assisted Sintering Process*, Materials, vol. 13, no. 4, DOI: 10.3390/ma13040879, 2020.
[20]. Zdorovets M. V., *et al.*, *Synthesis, Properties and Photocatalytic Activity of $CaTiO_3$-Based Ceramics Doped with Lanthanum*, Nanomaterials, vol. 12, no. 13, DOI: 10.3390/nano12132218, 2022.
[21]. Bantawal H., *et al.*, *Vanadium Doped $CaTiO_3$ Cuboids: Role of Vanadium in Improving the Photocatalytic Activity*, Nanoscale Adv., vol. 3, no. 18, p. 5301-5311, DOI: 10.1039/D1NA00341A, 2021.
[22]. Oproescu M., *et al.*, *Influence of Supplementary Oxide Layer on Solar Cell Performance*, Engineering, Technology & Applied Science Research, vol. 14, no. 2, p. 13274-13282, DOI: 10.48084/etasr.6879, Apr. 2024.
[23]. Schiopu A.-G., *et al.*, *Barium Carbonate Synthesized via Hydrolysis: Morphostructural Analysis and Photocatalytic Performance in Polymer and Geopolymer Matrices*, Crystals, vol. 15, no. 10, DOI: 10.3390/cryst15100890, 2025.
[24]. Setyaningsih E. P., *et al.*, *Preparation of $CaTiO_3$ Asymmetric Membranes Using Polyetherimide as Binder Polymer*, Indones. J. Chem., vol. 16, DOI: 10.22146/ijc.21169, 2016.
[25]. Gaikwad S. S., *et al.*, *A Green Chemistry Approach for Synthesis of $CaTiO_3$ Photocatalyst: Its Effects on Degradation of Methylene Blue, Phytotoxicity and Microbial Study*, Der Pharma Chem., vol. 4, p. 184-193, 2012.
[26]. Torimtubun A. A. A., *et al.*, *Affordable and Sustainable New Generation of Solar Cells: Calcium Titanate ($CaTiO_3$)-Based Perovskite Solar Cells*, E3S Web Conf., DOI: 10.1051/e3sconf/20183102006, 2018.
[27]. Aziz S. B., *et al.*, *Characteristics of PEO Incorporated with $CaTiO_3$ Nanoparticles: Structural and Optical Properties*, Polymers, vol. 13, no. 20, DOI: 10.3390/polym13203478, 2021.

THE ANNALS OF "DUNAREA DE JOS" UNIVERSITY OF GALATI
FASCICLE IX. METALLURGY AND MATERIALS SCIENCE
No. 1 - 2026, ISSN 2668-4748; e-ISSN 2668-4756
Article DOI: https://doi.org/10.35219/mms.2026.1.07

EXPERIMENTAL EVALUATION OF PATTERNED REFLECTIVE SURFACES FOR SOLAR GLARE REDUCTION IN SMALL UAV PLATFORMS

Florin-Bogdan MARIN[1,2], Silvia Patricia PĂMÂNT[1], Mihaela MARIN[1,2]

[1] "Dunarea de Jos" University of Galati, Romania
[2] Interdisciplinary Research Centre in the Field of Eco-Nano Technology and Advanced Materials CC-ITI, Faculty of Engineering, "Dunarea de Jos" University of Galati, Romania, 47 Domnească Street, RO-800008, Galaţi, Romania
e-mail: flmarin@ugal.ro

ABSTRACT

Small unmanned aerial vehicles (UAVs) increasingly require optical signature control in order to reduce visual detectability during daylight operations. This study investigates the influence of mirror-type polymer surface treatments on solar glare behavior and proposes a patterned reflective configuration as a passive mitigation strategy. A small multirotor UAV platform was partially covered (35–40%) with a PET-based reflective film exhibiting high specular reflectance (approximately 80–85%), and its visual response was evaluated under direct solar illumination.

Experimental observations indicated that continuous mirror-like surfaces generate intense specular glints for surface–sun incidence angles between approximately 20° and 45°, with glare visibility durations of 1.5–2.0 seconds. To reduce glare intensity, a segmented surface pattern was introduced, decreasing the estimated effective specular area from 30–35% to 15–20%. The patterned configuration demonstrated a shorter glare duration (0.5–0.8 seconds) and a proportional reduction in glare alignment probability. The results indicate that while reflective polymer coatings may contribute to background blending under diffuse lighting conditions, continuous mirror-like surfaces increase detection risk under direct sunlight. Patterned segmentation represents a low-cost, geometry-based approach for solar glint mitigation and optical camouflage enhancement in small UAV platforms.

KEYWORDS: UAV, drone, visual signature, reflective film, glare, patterning

1. Introduction

Unmanned aerial vehicles (UAVs) have experienced rapid technological development and widespread adoption in civilian, industrial, and security-related applications over the last decade [1-3]. Beyond endurance, payload capacity, and autonomy, operational effectiveness increasingly depends on signature management, particularly visual detectability under varying environmental and illumination conditions [4-5].

The visual detection of small aerial targets is strongly influenced by object size, motion, contrast against the background, illumination geometry, and surface reflectance properties [6-7]. Under daylight conditions, smooth or glossy surfaces may generate intense specular reflections ("glints"), significantly increasing detection probability at medium and long distances [8-9]. These optical effects are well documented in remote sensing and surface scattering theory [10], as well as in multispectral camouflage research [11].

Recent research in UAV survivability has focused on stealth materials, adaptive coatings, programmable polymer surfaces, and low-observable surface treatments [12-14]. Although effective, these approaches often require advanced materials, complex integration procedures, or increased manufacturing costs. For small UAV platforms, low-cost and geometry-based mitigation strategies remain particularly attractive [15].

THE ANNALS OF "DUNAREA DE JOS" UNIVERSITY OF GALATI
FASCICLE IX. METALLURGY AND MATERIALS SCIENCE
N°. 1 - 2026, ISSN 2668-4748; e-ISSN 2668-4756
Article DOI: https://doi.org/10.35219/mms.2026.1.07

From an optical standpoint, reflectance behavior and bidirectional reflectance distribution characteristics play a crucial role in detection probability [16]. In addition, object detection studies confirm that dynamic background interaction and directional reflections may significantly influence visibility when observed by electro-optical systems [17]. Beyond purely optical modeling approaches, recent advancements in computer vision and deep learning have demonstrated improved UAV detection capabilities using image-processing-based frameworks trained to recognize small aerial targets under complex background conditions [18].

Mirror-type polymer films represent a simple and accessible surface modification method. The theoretical assumption is that reflective surfaces may partially mimic environmental background colours by reflecting the surrounding scene. However, while such an approach may reduce contrast under diffuse lighting conditions, the same specular mechanism can lead to concentrated reflections under direct solar illumination that enhance visual detectability.

The balance between background blending and glare-induced detection therefore represents a relevant design challenge.

This paper presents a preliminary experimental evaluation of partial mirror-film coverage applied to a small UAV platform and investigates a patterned reflective surface as a passive mitigation strategy. The proposed approach combines material modification with CAD-supported surface segmentation to reduce the effective specular area and improve optical camouflage performance under direct sunlight.

2. Experimental procedure

The experimental study was conducted on a small multirotor UAV platform equipped with a polymer-based external shell. The UAV had an approximate diagonal span of 450 mm and a total mass of 1.2 kg. A commercially available mirror-type polymer film was selected due to its high specular reflectance and low implementation cost. The material was a PET-based reflective film with an estimated visible-spectrum reflectance of approximately 80–85% and a thickness between 50 and 80 μm. Prior to application, the UAV surface was cleaned and degreased to ensure proper adhesion. The reflective film was applied partially to selected fuselage regions, covering approximately 35–40% of the external surface. Partial coverage was intentionally adopted to avoid complete specular dominance and to allow comparative observation between reflective and non-reflective zones. The evaluation was performed under natural outdoor illumination, focusing on clear-sky conditions with direct solar exposure. The UAV was positioned at varying tilt angles to simulate realistic flight attitudes. The observer distance was maintained between 25 and 35 m to allow consistent visual comparison. Particular attention was given to surface–sun incidence angles between approximately 20° and 45°, representing the most critical interval for specular glare formation. The assessment was qualitative and based on repeated visual observations (five repetitions per configuration). The following parameters were evaluated: presence of high-intensity specular glints, duration of glare visibility, contrast difference between reflective and matte regions, and detectability against the sky background.

Glare duration was defined as the time interval during which the reflected highlight remained clearly distinguishable from background luminance. To mitigate sustained glare formation, a segmented reflective pattern was introduced. The pattern divided large continuous reflective regions into smaller geometrical segments, modifying local surface orientation and reducing coherent specular reflection alignment. This segmentation approach aimed to decrease the effective specular area without completely removing the reflective material, preserving potential background blending effects under diffuse lighting.

According to the law of reflection, the angle of incidence (θ_i) is equal to the angle of reflection (θ_r), both measured relative to the surface normal. This principle explains the concentration of reflected solar energy in a specific direction for smooth mirror-like surfaces:

$$\theta_i = \theta_r \quad (1)$$

where: θ_i - angle of incidence, θ_r - angle of reflection

It was observed that under direct sunlight the mirror-type surface generated concentrated reflections, increasing the probability of visual detection. This effect confirmed that while reflective materials may reduce contrast in some diffuse lighting conditions, they introduce a significant disadvantage under high solar irradiance.

To mitigate the identified drawback, an intermediate solution was proposed: introducing a patterned geometry on the reflective film. The pattern was designed to: break large continuous reflective surfaces into smaller segments, modify local reflection angles, reduce sustained specular highlight formation. The pattern concept aims to disrupt coherent specular reflection by introducing geometric discontinuities that scatter reflected light over a wider angular range.

THE ANNALS OF "DUNAREA DE JOS" UNIVERSITY OF GALATI
FASCICLE IX. METALLURGY AND MATERIALS SCIENCE
Nº. 1 - 2026, ISSN 2668-4748; e-ISSN 2668-4756
Article DOI: https://doi.org/10.35219/mms.2026.1.07

3. Results and Discussion

The experimental research revealed a clear trade-off between potential background blending and increased detectability due to specular glare. While reflective surfaces may reduce visual contrast in diffuse illumination conditions, their behavior under direct solar radiation represents a critical limitation. Figure 1 illustrates the initial experimental configuration with partial mirror-film coverage. Based on the observed glare effects, a patterned mitigation concept was developed (Figure 2). The proposed solution was further integrated into CAD-based UAV geometries designed (Figure 3) to enable controlled surface optimization.

Fig. 1. *The partial coverage of a drone surface with mirror-type plastic film*

As shown in Figure 1, the reflective film creates localized high-specular areas on the fuselage. During direct sunlight exposure, these zones generated intense glints visible from significant distance. The concentrated reflection is consistent with specular reflection physics, where smooth surfaces redirect incident light into narrow angular cones. This effect increases instantaneous contrast against the sky background and therefore enhances visual detectability.

Based on the glare effects observed in the configuration presented in Figure 1, a mitigation concept was developed to reduce sustained specular highlights without completely eliminating the reflective material. To demonstrate this intermediate solution. Figure 2 presents the patterned reflective surface applied to the mirror-type film.

Fig. 2. *The pattern created on the proposed material surface to reduce visual identification risk due to solar reflection*

The patterned geometry divides large continuous reflective areas into smaller segments. This segmentation modifies local surface orientation and disrupts coherent specular reflection. As a result,

THE ANNALS OF "DUNAREA DE JOS" UNIVERSITY OF GALATI
FASCICLE IX. METALLURGY AND MATERIALS SCIENCE
Nº. 1 - 2026, ISSN 2668-4748; e-ISSN 2668-4756
Article DOI: https://doi.org/10.35219/mms.2026.1.07

reflected solar radiation is redistributed over a wider angular range, reducing the probability of a strong, sustained glint being observed from a single viewing direction. The pattern therefore functions as a geometric camouflage strategy, combining reflective properties with controlled optical scattering. Following the conceptual validation of the patterned surface approach, the solution was integrated into a digital design workflow in order to enable systematic surface optimization. To support this engineering integration, Figure 3 presents the custom UAV geometry developed in the CAD environment.

The CAD model allows controlled partitioning of reflective and non-reflective zones, parametric adjustment of pattern dimensions, and visualization of surface orientation relative to the incident solar vector. This digital representation enables repeatable configuration studies and facilitates future quantitative optical simulations.

A comparative summary of glare behavior for the tested configurations is presented in Table 1. Glare duration was estimated through repeated visual observation during controlled angular displacement of the UAV, averaged over five test repetitions. Specular glare was observed for surface–sun incidence angles approximately between 20° and 45°.

Fig. 3. *The custom drone model designed*

The Glint Risk Index (GRI) provides a simplified estimation of glare intensity, indicating that detection risk increases proportionally with the effective specular area and when the observation angle approaches the specular reflection direction. It is defined as:

$$GRI = A_{specular} \cdot \cos(\theta) \quad (2)$$

The patterned configuration reduced the estimated effective specular area from approximately 30–35% to 15–20%, leading to a proportional decrease in the Glint Risk Index (GRI). Glare duration was defined as the time interval during which the reflected highlight remained clearly distinguishable from background luminance. Assuming a 45% reduction in effective specular area for the patterned configuration, the estimated GRI value decreases proportionally, indicating reduced glare alignment probability. For an identical observation angle, the proportional decrease in

THE ANNALS OF "DUNAREA DE JOS" UNIVERSITY OF GALATI
FASCICLE IX. METALLURGY AND MATERIALS SCIENCE
Nº. 1 - 2026, ISSN 2668-4748; e-ISSN 2668-4756
Article DOI: https://doi.org/10.35219/mms.2026.1.07

Aspecular leads to an equivalent reduction in the GRI value.

The present study is limited to qualitative outdoor observation without calibrated photometric instrumentation. No BRDF measurements or radiometric sensors were employed. Future work should include controlled illumination measurements, reflectance characterization, and BRDF-based modeling to quantitatively assess glare intensity and detection probability.

In addition to the proportional reduction in the Glint Risk Index, the patterned configuration demonstrated improved temporal instability of specular highlights. Unlike the continuous mirror surface, where glare remained sustained due to coherent reflection alignment, the segmented geometry introduced micro-variations in local surface normals. These variations resulted in rapid angular redistribution of reflected solar energy during UAV motion, thereby decreasing glare persistence.

Table 1. *Glare performance comparison for tested UAV surface configurations*

Configuration	Estimated Specular Area (%)	Glare Duration (s)	Estimated Risk
Continuous mirror	30–35%	1.5–2.0	High
Patterned mirror	15–20%	0.5–0.8	Medium
Matte surface	<5%	<0.3	Low

From an operational perspective, the reduction of glare duration from 1.5–2.0 s to 0.5–0.8 s represents a significant decrease in the visual detection window. In dynamic flight scenarios, even sub-second reductions in high-contrast glint exposure can meaningfully reduce target acquisition probability by human observers or electro-optical tracking systems.

Furthermore, the matte surface configuration confirms that minimal specular contribution (<5%) effectively suppresses glare formation. However, fully matte treatments eliminate potential background blending benefits under diffuse illumination. The patterned reflective approach therefore represents an intermediate optical solution, balancing contrast reduction under cloudy conditions with glare mitigation under direct solar irradiance.

4. Conclusions

This paper evaluated the optical behavior of mirror-type polymer coatings applied to small UAV platforms, focusing on solar glare formation and visual detectability under direct sunlight. Continuous reflective surfaces generated intense specular glints for incidence angles between 20° and 45°, with glare durations of 1.5–2.0 s, increasing the detection risk.

The introduction of a segmented reflective pattern reduced the effective specular area from 30–35% to 15–20%, decreasing glare duration to 0.5–0.8 s and proportionally lowering the Glint Risk Index (GRI). The patterned configuration disrupted coherent reflection alignment and redistributed reflected solar radiation over a wider angular range.

While matte surfaces minimized glare formation, they eliminate potential background blending benefits under diffuse illumination. The patterned reflective approach therefore represents a balanced, low-cost, geometry-based solution for mitigating solar glint while preserving partial camouflage functionality. Future work should include quantitative radiometric measurements, and BRDF-based modeling to further validate and optimize the proposed design strategy.

References

[1]. Colomina I., Molina P., *Unmanned aerial systems for photogrammetry and remote sensing: A review*, ISPRS Journal of Photogrammetry and Remote Sensing, 92, p. 79-97, 2014.
[2]. Doherty P., Rudol P., *A UAV search and rescue scenario with human body detection and geolocalization*, Advances in Artificial Intelligence, 4830, p. 1-13, 2007.
[3]. Zhang L., *et al.*, *Comparing human performance on target localization in near infrared and long wave infrared for cluttered environments*, Sensors, 24(20), 6662, 2024.
[4]. Schowengerdt R. T., *Remote Sensing: Models and Methods for Image Processing*, 3rd ed., Academic Press, 2007.
[5]. Hecht E., *Optics*, 5th ed., Pearson Education, 2016.
[6]. Bennett J. M., Mattsson L., *Introduction to Surface Roughness and Scattering*, 2nd ed., Optical Society of America, 2014.
[7]. Chipman R. A., *et al.*, *Polarized Light and Optical Systems*, CRC Press, 2018.
[8]. Nero G., *et al.*, *Reflective signatures of unresolved objects*, Optics Express, 32(15), p. 26167-26183, 2024.
[9]. Richards J. A., *Remote Sensing Digital Image Analysis: An Introduction*, 5th ed., Springer, 2013.
[10]. Lillesand T., *et al.*, *Remote Sensing and Image Interpretation*, 7th ed., Wiley, 2015.
[11]. Zhu H., *et al.*, *Multispectral camouflage for infrared, visible, lasers and microwave with radiative cooling*, Nature Communications, 12, 1805, 2021.

[12]. Shirke N., *et al.*, *Recent advances in stealth coating*, Polymer Bulletin, 81, p. 1-30, 2024.
[13]. Liu Y., *et al.*, *2D or not 2D: Shape-programming polymer sheets*, Progress in Polymer Science, 52, p. 79-106, 2016.
[14]. Goodrich M. A., *et al.*, *Supporting wilderness search and rescue using a camera-equipped mini UAV*, Journal of Field Robotics, 25(1-2), p. 89-110, 2008.
[15]. Kwan C., Budavari B., *Enhancing small moving target detection performance in low-quality and long-range infrared videos using optical flow techniques*, Remote Sensing, 12, 4024, 2020.
[16]. Schaepman-Strub C., *et al.*, *Reflectance quantities in optical remote sensing—Definitions and case studies*, Remote Sensing of Environment, 103(1), p. 27-42, 2006.
[17]. Rozantsev A., *et al.*, *Detecting flying objects using a single moving camera*, IEEE Transactions on Pattern Analysis and Machine Intelligence, 39(5), p. 879-892, 2017.
[18]. Marin F.-B., Marin M., *Drone detection using image processing based on deep learning*, Annals of "Dunarea de Jos" University of Galati, Fascicle IX: Metallurgy and Materials Science, 44(4), p. 36-39, 2021.

MANUSCRISELE, CĂRŢILE ŞI REVISTELE PENTRU SCHIMB, PRECUM ŞI ORICE CORESPONDENŢE SE VOR TRIMITE PE ADRESA:

MANUSCRIPTS, REVIEWS AND BOOKS FOR EXCHANGE COOPERATION, AS WELL AS ANY CORRESPONDANCE WILL BE MAILED TO:

LES MANUSCRIPTS, LES REVUES ET LES LIVRES POUR L'ECHANGE, TOUT AUSSI QUE LA CORRESPONDANCE SERONT ENVOYES A L'ADRESSE:

MANUSCKRIPTEN, ZIETSCHRITFTEN UND BUCHER FUR AUSTAUCH SOWIE DIE KORRESPONDENZ SID AN FOLGENDE ANSCHRIFT ZU SEDEN:

After the latest evaluation of the journals by the National Center for Science Policy and Scientometrics (**CENAPOSS**), in recognition of its quality and impact at national level, the journal will be included in the B^+ category, 215 code (http://cncsis.gov.ro/userfiles/file/CENAPOSS/Bplus_2011.pdf).

The journal is already indexed in:
DOAJ: https://doaj.org/
SCIPIO-RO: http://www.scipio.ro/web/182206
EBSCO: http://www.ebscohost.com/titleLists/a9h-journals.pdf
Google Academic: https://scholar.google.ro
Index Copernicus: https://journals.indexcopernicus.com
Crossref: https://search.crossref.org/

The papers published in this journal can be viewed on the website: http://www.gup.ugal.ro/ugaljournals/index.php/mms

Name and Address of Publisher:
Contact person: Prof. Dr. Eng. Elena MEREUŢĂ
Galati University Press - GUP
47 Domneasca St., 800008 - Galati, Romania
Phone: +40 336 130139
Fax: +40 236 461353
Email: gup@ugal.ro

Name and Address of Editor:
Ş. L. Dr. Eng. Marius BODOR
"Dunarea de Jos" University of Galati, Faculty of Engineering
111 Domneasca St., 800201 - Galati, Romania
Phone: +40 336 130208
Phone/Fax: +40 336 130283
Email: marius.bodor@ugal.ro

AFFILIATED WITH:

- THE ROMANIAN SOCIETY FOR METALLURGY
- THE ROMANIAN SOCIETY FOR CHEMISTRY
- THE ROMANIAN SOCIETY FOR BIOMATERIALS
- THE ROMANIAN TECHNICAL FOUNDRY SOCIETY
- THE MATERIALS INFORMATION SOCIETY (ASM INTERNATIONAL)

Edited under the care of the FACULTY OF ENGINEERING

Annual subscription (4 issues per year)

Fascicle DOI: https://doi.org/10.35219/mms

Volume DOI: https://doi.org/10.35219/mms.2026.1

Editing date: 15.03.2026
Number of issues: 200
Printed by Galati University Press (accredited by CNCSIS)
47 Domneasca Street, 800008, Galati, Romania